

Wrocław University of Technology-
Centre of Advanced Materials and Nanotechnology

Materials Science

**International Conference on Sol-Gel Materials
SGM2001, Rokosowo, Poland**

Vol. 20

•

No. 1

•

2002



Oficyna Wydawnicza Politechniki Wrocławskiej

Materials Science is an interdisciplinary journal devoted to experimental and theoretical research into the synthesis, structure, properties and applications of materials.

Among the materials of interest are:

- glasses and ceramics
- sol-gel materials
- photoactive materials (including materials for nonlinear optics)
- laser materials
- photonic crystals
- semiconductor micro- and nanostructures
- piezo-, pyro- and ferroelectric materials
- high- T_c superconductors
- magnetic materials
- molecular materials (including polymers) for use in electronics and photonics
- novel solid phases
- other novel and unconventional materials

The broad spectrum of the areas of interest reflects the interdisciplinary nature of materials research. Papers covering the modelling of materials, their synthesis and characterisation, physicochemical aspects of their fabrication, properties and applications are welcome. In addition to regular papers, the journal features issues containing conference papers, as well as special issues on key topics in materials science.

Materials Science is published under the auspices of the Centre of Advanced Materials and Nanotechnology of the Wrocław University of Technology, in collaboration with the Institute of Low Temperatures and Structural Research of the Polish Academy of Sciences and the Wrocław University of Economics.

All accepted papers are placed on the Web page of the journal and are available at the address:
<http://MaterialsScience.pwr.wroc.pl>

Editor-in-Chief

Juliusz Sworakowski

Institute of Physical and Theoretical Chemistry
Wrocław University of Technology
Wybrzeże Wyspiańskiego 27
50-370 Wrocław, Poland
sworakowski@pwr.wroc.pl

Associate Editors

Wiesław Stręk

Institute of Low Temperature
and Structure Research
Polish Academy of Sciences
P.O. Box 1410
50-950 Wrocław 2, Poland
strek@int.pan.wroc.pl

Jerzy Hanuza

Department of Bioorganic Chemistry
Faculty of Industry and Economics
Wrocław University of Economics
Komandorska 118/120
53-345 Wrocław, Poland
hanuza@credit.ae.wroc.pl

Scientific Secretary

Krzysztof Maruszewski

Institute of Materials Science and Applied Mechanics
Wrocław University of Technology
Wybrzeże Wyspiańskiego 27
50-370 Wrocław, Poland
maruszewski@pwr.wroc.pl

Advisory Editorial Board

Michel A. Aegerter, Saarbrücken, Germany
Ludwig J. Balk, Wuppertal, Germany
Victor E. Borisenko, Minsk, Belarus
Mikheylo S. Brodyn, Kyiv, Ukraine
Maciej Bugajski, Warszawa, Poland
Alexander Bulinski, Ottawa, Canada
Roberto M. Faria, São Carlos, Brazil
Reimund Gerhard-Multhaupt, Potsdam, Germany
Paweł Hawrylak, Ottawa, Canada
Jorma Hölsä, Turku, Finland
Alexander A. Kaminskii, Moscow, Russia
Wacław Kasprzak, Wrocław, Poland
Andrzej Kłonkowski, Gdańsk, Poland
Seiji Kojima, Tsukuba, Japan
Shin-ya Koshihara, Tokyo, Japan
Marian Kryszewski, Łódź, Poland
Krzysztof J. Kurzydłowski, Warsaw, Poland
Jerzy M. Langer, Warsaw, Poland
Janina Legendziewicz, Wrocław, Poland
Benedykt Licznarski, Wrocław, Poland

Tadeusz Luty, Wrocław, Poland
Joop H. van der Maas, Utrecht, The Netherlands
Bolesław Mazurek, Wrocław, Poland
Gerd Meyer, Cologne, Germany
Jan Misiewicz, Wrocław, Poland
Jerzy Mroziński, Wrocław, Poland
Robert W. Munn, Manchester, U.K.
Krzysztof Nauka, Palo Alto, CA, U.S.A.
Stanislav Nešpůrek, Prague, Czech Republic
Romek Nowak, Santa Clara, CA, U.S.A.
Tetsuo Ogawa, Osaka, Japan
Renata Reisfeld, Jerusalem, Israel
Marek Samoć, Canberra, Australia
Jan Stankowski, Poznań, Poland
Leszek Stoch, Cracow, Poland
Jan van Turnhout, Delft, The Netherlands
Jacek Ulański, Łódź, Poland
Walter Wojciechowski, Wrocław, Poland
Vladislav Zolin, Moscow, Russia

The Journal is supported by the State Committee for Scientific Research

Editorial Office

Anna Sofińska
Łukasz Maciejewski

Editorial layout

Hanna Basarowa

Cover design

Dariusz Godlewski

Printed in Poland

© Copyright by Oficyna Wydawnicza Politechniki Wrocławskiej, Wrocław 2002

Contents

Papers presented at the International Conference on Sol-Gel Materials, SGM 2001, Rokosowo, Poland

From the Editors.....	5
M. Opallo, Electrochemical redox reactions in solvated silica sol-gel glass.....	7
T. Aitasalo, J. Hölsä, H. Jungner, M. Lastusaari, J. Niittykoski, Comparison of sol-gel and solid-state prepared Eu^{2+} doped calcium aluminates.....	15
A. O. Ribeiro, C.R. Neri, Y. Iamamoto, O.A. Serra, Spectroscopic studies on the inclusion complexes of tetrakis(2-hydroxy-5-nitrophenyl)porphyrin with α -cyclodextrin in solution and in sol-gel matrix.....	21
J. Phalippou, T. Woignier, R. Sempéré, P. Dieudonné, Highly porous aerogels of very low permeability.....	29
D. Hreniak, E. Łukowiak, K. Maruszewski, R. Pażik, W. Stręk, Structure, spectroscopy and dielectric properties of $\text{BaTiO}_3:\text{Eu}^{3+}$ nanocrystallites prepared by the sol-gel method.....	43
M. Jasiorski, K. Maruszewski, W. Stręk, Optical behaviour of sol-gel derived photonic structures formed by submicron silica spheres.....	51
A. M. Kłonkowski, Luminescent materials, recognition phases of the chemical sensors and heterogeneous catalysts prepared by sol-gel method.....	57
N. Al-Dahoudi, M.A. Aegerter, Redispersable nanopowders for wet chemical coating processes. Application to transparent conducting coatings.....	71
L. C. Klein, Opportunities for sol-gel materials in fuel cells.....	81
A. Klukowska, U. Posset, G. Schottner, M. L. Wis, C. Salemi-Delvaux, V. Malatesta, Photochromic hybrid sol-gel coatings: preparation, properties, and applications.....	95

Regular papers

M. Maćzka, J. Hanuza, N. Sidorov, S. Kojima, Study of thermal disordering of the $\text{KSc}(\text{WO}_4)_2$ crystal structure by Raman spectroscopy.....	105
E. Zych, D. Hreniak, W. Stręk, $\text{Lu}_2\text{O}_3:\text{Eu}$, a new X-ray phosphor.....	111
M. Pawłowska, W. Wojciechowski, Review of luminescence and magnetic properties of antiferromagnetic KMnCl_3 , RbMnCl_3 , TlMnCl_3 and $(\text{C}_n\text{H}_{2n+1}\text{NH}_3)_2\text{MnCl}_4$ ($n = 1, 2$).....	123
V. E. Fainzilberg, Effects of polarization of radiofrequency radiation in polycrystalline ESR.....	137

From the Editors

With this issue of *Materials Science*, we are re-launching the journal after a few -year interruption. Its profile has been modified, the attention being now focused on the reporting results of experimental and theoretical research into synthesis, structure, properties and applications of materials.

The journal will appear quarterly; in addition to regular papers on various aspects of the materials, we plan to publish issues containing conference papers, as well as special issues on key topics in materials science. We are pleased to announce that readers will have access to the electronic version of current and recent issues of the journal, as well as to the texts of all manuscripts: they will be made available on the Web pages of the journal.

Several distinguished scientists from Poland and from all over the world agreed to serve on the Advisory Editorial Board. We hope that, with their active participation and support, *Materials Science* will succeed in making its name among other materials science and engineering journals.

*Juliusz Sworakowski,
Wiesław Stręk,
Jerzy Hanuza,
Krzysztof Maruszewski*

Electrochemical redox reactions in solvated silica sol–gel glass*

MARCIN OPALLO

Institute of Physical Chemistry, Polish Academy of Sciences, ul. Kasprzaka 44/52,
01-224 Warszawa, Poland. E-mail: mopallo@ichf.edu.pl

The studies of the electrochemical redox reactions in solvated silica sol–gel glass were reviewed. The methodology of the experiments with emphasis on the direct preparation of the solid electrolyte and the application ultramicroelectrodes was described. Generally, the level of the electrochemical signal is not much below that observed in liquid electrolyte. The current depends on time elapsed after gelation, namely the longer time, the smaller current. The differences between electrochemical behaviour of the redox couples in monoliths and thin layers were described.

Key words: sol–gel, solid electrolyte, electrode reaction, redox reaction, diffusion coefficient, ultramicroelectrode

1. Introduction

Inorganic materials obtained in a mild reaction conditions, i.e. by sol–gel method [1], emerged recently as versatile matrices for preparation of solid electrolytes suitable for use at ambient temperatures [2]. These materials offer several advantages over organic polymers including physical rigidity, chemical inertness, negligible swelling in aqueous or organic solutions, photochemical and thermal stability and optical transparency [3]. The presence of some amount of mobile ions within the matrix is required for the future application of these materials in electrochemical devices. Therefore they cannot be used in the form of xerogels – thoroughly dried gels, where mobility of species is heavily restricted, because of the small volume of solvent (typically water) left after aging and drying. The use of wet or – in another words – solvated gels seems to be a better strategy.

Application of these materials as electrolytes in amperometric sensors, electrochemiluminescent or electrochromic devices often requires the presence of redox-active ions or molecules within the matrix. These species are able to exchange elec-

*The paper presented at the International Conference on Sol–Gel Materials, SGM 2001, Rokosowo, Poland.

trons with the electrode without the mass transfer across the electrode/electrolyte interface. Before practical application the knowledge about electrochemical redox reactions at the electrode/silica matrix interface seems to be indispensable. On the other hand, the electrochemical methodology using redox probes provides a promising approach for characterisation of inorganic materials.

The sol–gel chemistry received attention of electrochemists quite recently (see [2] and refs. therein). Here, the first attempts to study electrochemical redox reactions in solvated silica sol–gel glass will be presented and summarized. This review will be restricted to the systems without macroscopically liquid phase. Therefore, the electrochemical processes at silica-matrix modified electrodes immersed into the liquid electrolyte will not be taken into account.

2. Methodology

Most of the electrochemical studies were carried out during tens of days starting from the sol preparation for aging process. In this way all changes in gel structure during formation and aging can be followed. The sol was usually placed into a small covered vial made of organic polymer (polyethylene, polypropylene or polystyrene) (Fig. 1). The working, reference and (sometimes) counter electrodes in a form of glass embedded discs or metal wires were immersed into the sol and fixed in the cap [4–19]. Fortunately, due to poor affinity of silicate matrix towards the organic polymer walls the shrinking gel pulls away only from the walls and the bottom of the cell. After few days it is held only by the electrodes, especially when they consist of glass body.

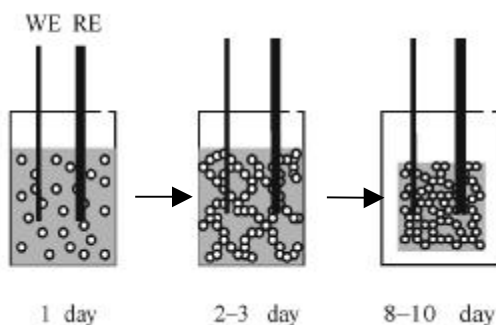


Fig. 1. Scheme of the electrochemical cell used in experiments with solvated sol–gel glass blocks;
 WE – working microdisc electrode, RE – reference electrode

This methodology seems to be superior, because the electrical contact between the electrodes and solid electrolyte is not affected by the gelation and aging. However, it makes the working electrode vulnerable on the fouling processes. The latter include adsorption of impurities or uncontrolled potential step far beyond the potential win-

dow. This in turn affects the reproducibility of electrochemical experiments, because the working electrode cannot be removed from the electrolyte for polishing without destroying the gel. This problem can be eventually avoided by gentle pressing the electrode towards the wall of the gel. Until now such methodology was used only for impedance spectroscopy studies, where the sample was held between two spring loaded electrodes [20–26]. The electrode assembly embedded on the flat support covered by sol-gel film [10, 15, 27–31] (Fig. 2) also may suffer from uncontrolled fouling. Additionally, the properties of the thin layer of the sol-gel electrolyte usually differ from those of gel monolith [10, 18]. However, from the point of view of application in electrochemical device, this configuration seems to be superior.

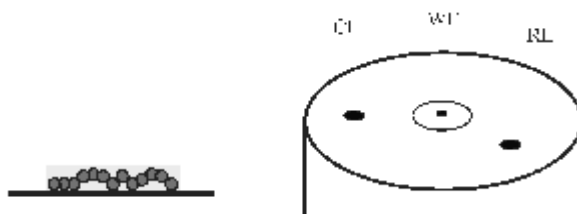


Fig. 2. Scheme of the electrochemical cell used in experiments with solvated sol-gel glass blocks; WE – working microdisc electrode, CE – counter electrode and RE – reference electrode

Almost all studies of the electrochemical redox reactions in silica sol-gel glass have been done with ultramicroelectrodes – electrodes of dimensions in the range of micrometers [32]. This is because of the relatively large resistance of the sol-gel electrolyte and large signal to noise ratio. The current obtained with a standard disc ultramicroelectrode, of diameter of about 10 μm , is in the nanoamperes range. Therefore, the effect of the electrolyte resistance, proportional to the product of current and resistance (so-called ohmic or IR drop [33]), is minor. It has to be emphasized that the measurement of such low current no longer remains a problem. Eventually its magnitude can be increased by application of interdigitated microelectrodes (IMES) without losing most of the features of the single ultramicroelectrode [27]. Also the application of the ultramicroelectrodes enables one independent estimation of the diffusion coefficient and concentration of the redox probe. This is because of two different transport regimes, namely, hemispherical and semiinfinite diffusion, which can be observed in a single experiment at long- and short-time scales [34].

3. Sol-gel electrolyte composition

Until now most of the studies were done in acid catalysed gel obtained from tetramethoxysilicate (TMOS) or tetraethoxysilicate (TEOS) precursor. The redox probe was dissolved in the sol. The mobility of the substrate is essential to obtain measurable current. Therefore, the drying rate was carefully controlled by making small hole(s) in the cap of the electrochemical cell. Although there are reports about elec-

trochemical studies in liquid without so-called supporting electrolyte, only the presence of the excess of ions allows to obtain results which can be analysed in a straightforward manner [33]. Therefore, in almost all studies the salt was added to the sol before the gel formation. Its presence does not affect the stability of the gel. The addition of ionomer like Nafion® which results in formation of polymer–silica composite material represents an alternative approach (see [12] and refs. therein).

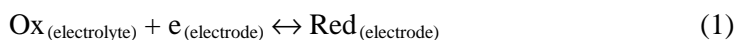
In order to introduce reactant insoluble in water, we added it as its solution in organic solvents like PC [10, 16], sulfolane (TMS) [16–18] or dimethylsulphoxide (DMSO) [19] directly to the sol. Such a way of preparation of sol–gel organic solid electrolyte was originally proposed by Wu et al. [20] for the prospective application in batteries. A concentrated lithium salt solution in ethylene carbonate and propylene carbonate mixture was directly added to an aqueous TMOS sol. The gel formation rate and material stability depend on the sol to organic solvent ratio. The gel obtained with a small amount of organic electrolyte was not transparent and susceptible to fracturing, whereas a large excess of the organic electrolyte resulted in a very soft, wet material [20]. We observed that addition of organic solvent increased gelation time in comparison to hydrated gel and it depended on the properties of the solvent and salt. After addition of PC or TMS solution it increases from few hours to 1–3 days [16–18], whereas DMSO extends gelation time to more than 20 days [19]. For lithium perchlorate solution in PC it occurs within 12 hours, however, it takes 2 days to obtain gel containing tetraalkylammonium salts. The replacement of PC with TMS also similarly extends the time of gelation.

The exchange of an organic electrolyte with liquid already present within silicate matrix as an effect of hydrolysis and gelation represents another possibility of silica sol–gel glass modification [21–26]. Like as in the case described previously [20] the solid electrolyte with conductivity not much below of the liquid one was obtained. It has to be emphasized that during both procedures few percent of strongly solvating water is left within matrix [26].

The value of isoelectric point of silica sol–gel glass equal to 2 [35] indicates quite large concentration of protons in the matrix. This may be enough to provide ionic budget for electrochemical experiments. Indeed, it is possible to obtain a cyclic voltammogram with the features similar to that obtained in a liquid in the absence of salt added [19]. This was done in sol–gel glass with ferrocene (Fc) solution in organic aprotic solvent: propylene carbonate (PC) without any salt present and it indicates the important role of protonic conduction of the wet sol–gel silica matrix.

4. Electrode reactions and transport rate

The electrochemical behaviour of the redox-active ions and molecules in a gel monolith is not much different from that in an electrolyte solution [4–19]. The shape of the cyclic voltammograms corresponding to simple redox reaction:



obtained at slow and fast scan rate is similar for all systems studied within tens of days after aging. This indicates the stability of the electrode/sol–gel electrolyte interface under slow and fast polarisation conditions and it looks promising from the point of view of the prospective applications. Contrary to the gel solvated with organic solvent some deterioration of fast scan cyclic voltammetry curve was reported for hydrated gels [8]. This may be caused by gel shrinking and pore collapse. It has been observed that during 20–50 days the hydrated gel shrinks by about 30%, whereas that containing organic solvent shrinks only by about 10%. For all cases studied the rate of electrode reaction is controlled by the reactant transport. The magnitude of the plateau or peak current decreases with time, however for a given time the magnitude of decrease depends on the system. We have found that even after one year after gelation of the gel modified with organic solvent, it is possible to obtain relatively well developed voltammetric curve.

Some shift of the redox potential (E°), which can be considered the measure of the difference in interactions of Ox and Red with surrounding environment, was observed during gel aging [7, 10, 13, 16]. However, there exists the problem of the stability of the reference electrode potential. It has to be emphasized that the effect on silica matrix on the surface of metals, their oxides or salts is unknown. Therefore it is better to use reference electrode separated from the gel. With this methodology small shift of E° by no more than 0.04 V [13] was observed in hydrated gel 30 days after gelation. This indicates small change in interactions between redox probe and surrounding media after gelation. Its degree and direction depends on the redox couple.

The fact that the presence of the silica matrix does not substantially affect the heterogeneous electron transfer rate enables us to determine the rate of the redox probe motion in terms of apparent diffusion coefficient (D_{app}). This parameter should be called “apparent” because it is not always clear whether the concentration of redox species is equal to that in the sol and also it may depend on time passed after gelation [9].

It is quite general that the value of D_{app} is smaller than that for an analogous liquid electrolyte. However, for some systems shortly after gel point it is larger than in the sol [16, 18]. The degree of D_{app} decrease depends on the redox probe, salt and organic solvent additives [4, 5, 7, 10, 16–19]. For the systems where this effect is substantial (2–4 times), it is most pronounced during the first few days elapsed after gelation. At longer time it is not significant. The D_{app} decrease correlates with the mass decrease during aging and drying [13]. For positively charged and neutral probes in hydrated gels or in gels solvated by organic solvents the decrease is substantial [4, 5, 7, 10, 16–19]. On contrary, D_{app} of the negatively charged reactants in hydrated gels is almost time-independent [7, 13].

The decrease of D_{app} seems to be caused by the fact that within a silicate matrix at some positions redox probes ions cannot move in every direction. Their motion is restricted by the size and geometry of the pores. This of course depends on the degree of polycondensation which still occurs, especially just after gel point and on aging of

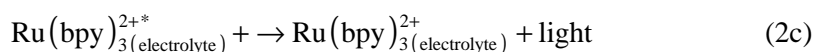
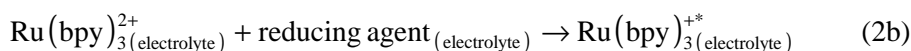
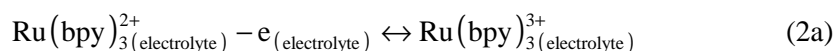
the gel. Unfortunately, there is no efficient direct method of the pore size of a wet gel estimation. The diameter of pores in TMOS acid-catalysed xerogel obtained in the presence of surfactant is in the range of 10 nm [1]. The minor shrinking of the wet gel indicates that they are much larger than pores in an analogous xerogel. Therefore, they are expected to be one or two orders of magnitude larger than the typical diameter of the redox probe equal about 1 nm. The correlation between D_{app} and sample mass decrease may indicate the evaporation of the liquid volume within the matrix [13]. This should eventually affect the concentration of the redox probes. The concentration increase in aging hydrated gel was claimed [7]. For gels solvated with organic solvents this effect is not important [16, 18].

There are many observations indicating that the interactions between the silicate matrix and the redox probes are minor, such as the correlation between the value of D_{app} , the size of the reactant and viscosity of the solvent predominately present in the matrix [16–18], as results from the Nernst–Einstein equation valid for liquids. Also a similar activation energy (E_a) of the reactant transport in the matrix and analogous liquid electrolyte supports this view [18]. However, more pronounced temporal dependence of the rate transport of the positively charged or neutral probes [4, 5, 7, 10, 16–19] indicates that situation is not so simple. The surface of the pore walls of silica sol–gel glass is covered by a number of functional groups: siloxane (SiOSi), silanol (SiOH), siloxide (SiO⁻) and unreacted alkoxide groups. The interactions between matrix charged substituents bearing electric charge or oxygen atoms having free electron pair (oxygen) with molecules and ions present in the pores may occur. This may be the reason of the different temporal dependences of the apparent diffusion coefficient. Organic additives may also affect the process of the gel formation. It is already known that addition of organic substances, usually surfactants, causes the increase of the xerogel pores (see [36] and refs. therein). The minor shrinking of the gel modified with organic solvents and D_{app} increase in the presence of large tetraalkylammonium cations in the gel [16–19] indicates that this is the case. One may also conclude that the addition of organic solvent or surfactant eventually allows one to increase the reactant transport by manipulation with the pore size.

The electrochemical behaviour of insoluble redox probes encapsulated into silica sol–gel glass and their action as electron mediators was also reported [9, 15]. The precursors of the redox active solids were incorporated directly into the sol. The formation of mixed valence ruthenium oxide with cyano cross links [9] or colloidal Prussian Blue occurs during sol–gel transition. Their electrochemical behaviour was not very far from that observed in contact with liquid electrolyte. This is because the hydrated gel provided mobile ions and their motion limits the electron hopping rate [9, 15].

The generation of light using electrochemical redox reaction represents another interesting aspect of sol–gel electrochemistry with prospective application in chemical analysis or electrochemiluminescent displays. It is possible to generate light within hydrated sol–gel glass monolith of ruthenium(II) tris(bipyridine) (Ru(bpy)₃)²⁺ at the

presence of oxalate or tertiary amines as reducing agents [8, 11]. The electrogenerated chemiluminescence (ecl) process can be described as follows:



However, the intensity of electrogenerated light was smaller than that in the absence of the sol-gel matrix. Ecl was found to be stable for 10 days [11].

5. Thin films

There is no electrochemical study comparing the electrochemical behaviour of the same system in hydrated gel. This, however, has been done for sol-gel glass with gel solvated by organic solvent [10, 16]. For gel made from TEOS, the magnitude of the current connected with electrooxidation of ferrocene is similar for thin film and monolith [16], whereas in the case of TMOS precursor the former is few times smaller [10]. Unfortunately, the signal disappears few days after gel formation.

The sol-gel approach has also been used by Cox group for generation of thin films of electrolytes containing catalyst for prospective use in amperometric sensors [27–29, 31]. The conductivity of the sol-gel matrix filled with concentrated acid, concentrated salt solution or redox catalyst is large enough that device can work in the absence of liquid electrolyte. They can be used for determination of gaseous substrates: NH_3 [27], CO [28], H_2O_2 [29] or monomethyl hydrazine [31]. These compounds are extracted into sol-gel film and electrochemically oxidised. Their electrode reaction involves nonmediated or mediated electrooxidation with mechanism more complicated than Eq. (1). It has to be emphasized that in one case the signal was claimed to be independent on humidity of the air [28] what is exciting in terms of application to gas sensors.

6. Conclusions

The electrochemical studies in silica sol-gel glass represent an example of the electrochemistry without the liquid electrolyte while preserving characteristic features known from the experiments in liquid media. Although quite consistent view emerges from the papers reviewed, there are many things to be done. At first sight the course of the electrochemical redox reactions in solvated silica sol-gel glass seems to be not very far from that observed in liquid electrolytes. However, the knowledge about interactions between matrix and solvent or solute except the restrain of redox probe

motion is very modest. Obviously more systems have to be studied. Also the careful studies of the gelation effect on the redox potential are highly desirable.

References

- [1] BRINKER C.J., SCHERER G.W., *Sol-gel Science: The Physics and Chemistry of Sol-gel Processing*, 1990, San Diego, Academic Press.
- [2] LEV O., WU Z., BHARATHI S., GLEZER V., MODESTOV A., GUN J., RABINOVICH L., SAMPATH S., *Chem. Mater.*, 1997, 9, 2354.
- [3] LEV O., TSIONSKY M., RABINOVICH L., GLEZER V., SAMPATH S., PANKRATOV I., *J. Gun, Anal. Chem.*, 1995, 67, 22A.
- [4] AUDEBERT P., GRIESMAR P., SANCHEZ C., *J. Mater. Chem.*, 1991, 2, 699.
- [5] AUDEBERT P., GRIESMAR P., HAPIOT P., SANCHEZ C., *J. Mater. Chem.*, 1992, 2, 1293.
- [6] HOLSTROM S.D., KARWOWSKA B., COX J.A., KULESZA P.J., *J. Electroanal. Chem.*, 1998, 456, 239.
- [7] COLLINSON M.M., ZAMBRANO P., WANG H., TAUSSIG J., *Langmuir*, 1999, 15, 662.
- [8] COLLINSON M.M., MARTIN S.A., *Chem. Commun.*, 1999, 899.
- [9] LAUGHLIN J.B., MIECZNIKOWSKI K., KULESZA P.J., COX J.A., *Electrochem. Solid State Lett.*, 1999, 2, 574.
- [10] OPALLO M., KUKULKA J., *Electrochem. Commun.*, 2000, 2, 394.
- [11] COLLINSON M.M., NOVAK B., MARTIN S.A., TAUSSIG J.C., *Anal. Chem.*, 2000, 72, 2914.
- [12] KHRAMOV A., COLLINSON M.M., *Anal. Chem.*, 2000, 72, 2943.
- [13] HOWELL A.R., ZAMBRANO P., COLLINSON M.M., *Anal. Chem.*, 2000, 72, 5625.
- [14] COLLINSON M.M., HOWELLS A.R., *Anal. Chem.*, 2000, 72, 702A.
- [15] MIECZNIKOWSKI K., COX J.A., LEWERA A., KULESZA P.J., *J. Solid State Electrochem.*, 2000, 4, 199.
- [16] OPALLO M., KUKULKA-WALKIEWICZ J., *Electrochim. Acta*, 2001, 46, 4235.
- [17] OPALLO M., KUKULKA-WALKIEWICZ J., *J. New Mater. Electrochem.Sys.*, 2001, 4, 155.
- [18] OPALLO M., KUKULKA-WALKIEWICZ J., *Solid State Ionics*, in press.
- [19] OPALLO M., KUKULKA-WALKIEWICZ J., *J. Sol-gel Sci. Technol.*, submitted to press.
- [20] WU P-W., HOLM S.R., DUONG A.T., DUNN B., KANER R.B., *Chem. Mater.*, 1997, 9, 1004.
- [21] DURAKPASA H., BREITER M.W., DUNN B., *Electrochim. Acta*, 1993, 38, 371.
- [22] DURAKPASA H., BREITER M.W., DUNN B., *J. Sol-gel Sci. Technol.*, 1994, 2, 251.
- [23] DURAKPASA H., BREITER M.W., DUNN B., *J. Electroanal. Chem.*, 1997, 428, 141.
- [24] WASIUCIONEK M., BREITER M.W., *J. Applied Electrochem.*, 1997, 27, 1106.
- [25] WASIUCIONEK M., BREITER M.W., *J. Electroanal. Chem.*, 1998, 443, 117.
- [26] WASIUCIONEK M., BREITER M.W., *J. Sol-gel Sci. Technol.*, 1998, 11, 17.
- [27] ALBER K.S., COX J.A., *J. Electrochem. Soc.*, 1996, 143, L126.
- [28] TESS M.E., COX J.A., *Anal. Chem.*, 1998, 70, 187.
- [29] HOLMSTROM S.D., COX J.A., *Electroanalysis*, 1998, 10, 597.
- [30] COX J.A., WOLKIEWICZ A.M., KULESZA P.J., *J. Solid State Electrochem.*, 1998, 2, 247.
- [31] HOLMSTROM S.D., SANDLIN Z.D., STEINECKER W.H., COX J.A., *Electroanalysis*, 2000, 12, 262.
- [32] WIGHTMAN R.M., WIPF D.O., [in:] A.J. Bard (Ed.), *Electroanalytical Chemistry*, 1989, New York, Marcel Dekker Inc., Vol. 15, p. 89 and references cited therein.
- [33] BARD A.J., FAULKNER L., *Electrochemical Methods. Fundamentals and Applications*, 2001, New York, Wiley.
- [34] DENAULT G., MIRKIN M.V., BARD A.J., *J. Electroanal. Chem.*, 1991, 308, 27.
- [35] ILER R.K., *The Chemistry of Silica*, 1979, New York, Wiley.
- [36] ROTTMAN C., GRADER G., HAZAN Y. DE, MELCHIOR S., AVNIR D., *J. Am. Chem. Soc.*, 1999, 121 8533.

Comparison of sol–gel and solid-state prepared Eu²⁺ doped calcium aluminates*

TUOMAS AITASALO^{1,2}, JORMA HÖLSÄ^{1,3}, HÖGNE JUNGNER⁴,
MIKA LASTUSAARI^{1,2}, JANNE NIITTYKOSKI^{1,2**}

¹University of Turku, Department of Chemistry, FIN-20014 Turku, Finland

²Graduate School of Materials Research, Turku, Finland

³ENSCP, CNRS, Laboratoire de Chimie Appliquée de l'Etat Solide, 11,
rue Pierre et Marie Curie, F-75231 Paris Cédex 05, France

⁴University of Helsinki, Dating Laboratory, P.O. Box 11, FIN-00014, Helsinki

The Eu²⁺ doped calcium aluminate (CaAl₂O₄:Eu²⁺) was prepared by the sol–gel method. The structure and luminescence properties of the title compound were studied and compared to the corresponding properties of the materials prepared by a conventional solid state reaction. The use of the sol–gel method in preparation lowered the reaction threshold temperature by c.a. 200 °C. An unusual hexagonal form of CaAl₂O₄:Eu²⁺, which cannot be prepared by the solid state reaction, was obtained by the sol–gel method. The UV excited luminescence and afterglow bands of the hexagonal CaAl₂O₄:Eu²⁺ were observed at a slightly longer wavelength than that of the normal monoclinic phase due to small differences in the crystal field effect on the splitting of the excited 4f⁶5d¹ configuration of the Eu²⁺ ion. The afterglow lifetime of the hexagonal phase was slightly longer than that of the monoclinic one due to deeper traps.

Key words: Eu²⁺ doped calcium aluminate, sol–gel method, persistent luminescence

1. Introduction

The Eu²⁺ doped alkaline earth aluminates, MAl₂O₄:Eu²⁺ (M = Ca, Sr) are potential persistent luminescence materials to replace the traditional ZnS:Cu used, e.g. in luminous paints [1]. The aluminates yield strong luminescence at the blue/green region [2, 3] that is characterized by a rapid initial decay from the Eu²⁺ ion followed by extremely long afterglow. The afterglow can be enhanced even more by co-doping the

*The paper presented at the International Conference on Sol–Gel Materials, SGM 2001, Rokosowo, Poland.

**Corresponding author, fax: +358-2-3336700, e-mail: japeni@utu.fi.

aluminates with some RE³⁺ ions (e.g. Dy³⁺ and Nd³⁺) [4–7]. Although the overall mechanism of the persistent luminescence of MAI₂O₄:Eu²⁺ is now quite well agreed on [4–7], the details involved are largely unknown. The search for new persistent luminescence materials would be facilitated greatly if the underlying mechanisms were known.

The solid state reaction of monoclinic CaAl₂O₄ must be carried out at high temperatures (around 1300 °C) since impurities as Ca₃Al₂O₆ are formed at lower temperatures [8]. On the other hand, the successful preparation of the CaAl₂O₄ powders at low temperatures (900 °C) by the sol–gel synthesis has been reported [9]. With the sol–gel method a metastable phase of CaAl₂O₄, which can not be prepared by the solid state reaction, has been obtained [10, 11]. In this work, studies on the sol–gel preparation, structure and luminescence of CaAl₂O₄:Eu²⁺ are reported and compared to those of the material prepared by the solid state route.

2. Experimental

The polycrystalline CaAl₂O₄:Eu²⁺ was prepared with the sol–gel method [8] using stoichiometric mixtures of aluminum isopropoxide (Al(OC₃H₇)₃), calcium nitrate (Ca(NO₃)₂·4H₂O) and europium oxide (Eu₂O₃, 0.5 mole-%) as starting materials. The gel was heated at 180 °C for 10 h to remove water and then at 850 °C for 20 h under a N₂ + 12% H₂ gas mixture. The solid state reaction between calcium carbonate (CaCO₃), aluminum oxide (Al₂O₃) and europium oxide was carried out at 1250 °C for 6 h.

The thermogravimetric (TG) curves were measured with a TA Instruments SDT 2960 Simultaneous DTA-TGA thermoanalyzer. The sol–gel and solid state reactions were studied in the temperature range between 25 and 1400 °C. The heating rate was 10 °Cmin⁻¹ and the gas (N₂ + 12% H₂) flowing rate was 100 cm³min⁻¹. Sample weights were ca. 10 mg.

The X-ray powder diffraction patterns were measured with an Enraf-Nonius PDS120 diffractometer (CuK_{α1} radiation; λ = 1,5406 Å) equipped with an INEL CPS120 position sensitive detector. The measurements were carried out at room temperature between 5 and 125 degrees using a flat rotating sample holder. The angular resolution of the apparatus was better than 0,018 degrees in *q*. A mixture of silicon (NIST standard #640b) and fluorophlogopite (NIST #675) powders was used as an external standard.

The luminescence and afterglow spectra were measured at room temperature using a Perkin Elmer LS-5 spectrometer. The UV-excitation from a xenon lamp was centered sharply at 350 nm. Prior to the afterglow measurements materials were exposed to radiation from a conventional tricolor fluorescent lamp for 10 s. The delay between the initial irradiation and afterglow measurements was 3 min. The thermoluminescence glow curves were measured with a Risø TL/OSL-DA-12 system between 25 and 400 °C monitoring globally emission up to 600 nm using a heating rate of 5 °C·s⁻¹.

3. Results and discussion

A 52% loss of weight was observed in the TG curve of $\text{CaO-Al}_2\text{O}_3$ gel at the temperature range between 200 and 600 °C (Fig. 1). This was due to the loss of organic solvent and the decomposition of nitrate. No loss of water below 200 °C was observed because the gel was heated at 180 °C before measurements. The sol-gel method lowered the reaction threshold temperature for CaAl_2O_4 by ca. 200 °C compared to the solid state reaction. With the sol-gel method, the pure monoclinic CaAl_2O_4 phase was not formed below 1200 °C because the byproducts as CaAl_4O_7 , $\text{Ca}_3\text{Al}_2\text{O}_6$ and $\text{Ca}_{12}\text{Al}_{14}\text{O}_{33}$ were also formed.

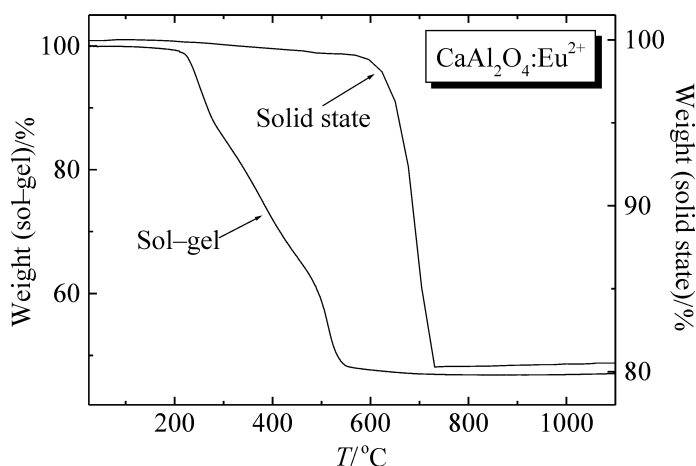


Fig. 1. Thermogravimetric curves of the sol-gel and solid-state prepared $\text{CaAl}_2\text{O}_4:\text{Eu}^{2+}$ materials; heating rate – $10\text{ }^\circ\text{C}\cdot\text{min}^{-1}$, gas ($\text{N}_2 + 12\% \text{H}_2$) flow rate: – $100\text{ cm}^3\cdot\text{min}^{-1}$, sample weight – ca. 10 mg

The metastable $\text{CaAl}_2\text{O}_4:\text{Eu}^{2+}$ phase, probably stabilized by impurities, was obtained with the sol-gel method by heating at 850 °C. Other products or starting materials were not observed. The X-ray diffraction patterns of the sol-gel hexagonal and the solid state prepared monoclinic phases were very similar (Fig. 2). The higher structural symmetry of the hexagonal phase can be seen in the less complicated pattern, however. The structure of the metastable $\text{CaAl}_2\text{O}_4:\text{Eu}^{2+}$ was determined as hexagonal with the space group P6_3 ($Z = 6$), in contrast to earlier data [10] reporting an orthorhombic structure. The calculated lattice parameters were as follows: $a = 8.74$ and $c = 8.08$ Å.

The UV excited luminescence and afterglow spectra of the monoclinic $\text{CaAl}_2\text{O}_4:\text{Eu}^{2+}$ phase consist of a single wide band peaking in the blue region ($I_{\text{max}} = 440$ nm) as reported earlier [1]. The band in the luminescence and afterglow spectra of the hexagonal $\text{CaAl}_2\text{O}_4:\text{Eu}^{2+}$ occurred at a slightly longer wavelength compared to that of the mono-

clinic phase (Fig. 3). The luminescence of the Eu^{2+} ion originates from the transitions between the $4f^65d^1$ and $4f^7$ configurations and can easily vary, in general, from UV to red depending on the host lattice [12]. A shift in the luminescence band position for the different CaAl_2O_4 phases can be explained by a small change in the crystal field effect on the Eu^{2+} ion because the splitting of the excited $4f^65d^1$ configuration is very strongly affected by the environment.

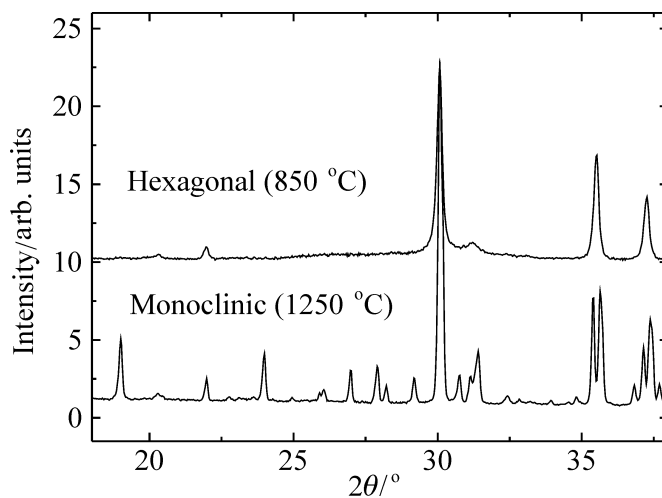


Fig. 2. X-ray diffraction patterns of the hexagonal and monoclinic $\text{CaAl}_2\text{O}_4:\text{Eu}^{2+}$ materials at room temperature ($\text{CuK}\alpha_1$ radiation)

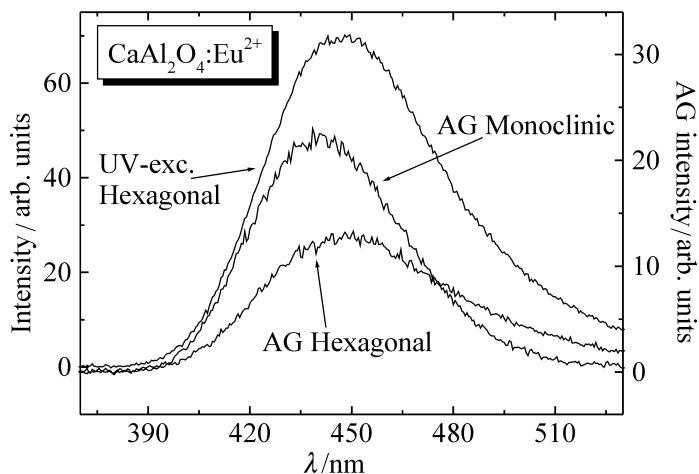


Fig. 3. UV-excited luminescence and afterglow spectra of the hexagonal and monoclinic $\text{CaAl}_2\text{O}_4:\text{Eu}^{2+}$ materials at room temperature

The afterglow spectra of the both polymorphs have the same band position, shape and width than those of the UV excited spectra indicating the same Eu^{2+} luminescent center. The initial afterglow from the hexagonal phase was weaker than that from the monoclinic one, but the difference was not as clear than as the case of the UV-excited spectra. The Eu^{2+} ion seems to favour only one site of the three Ca sites available in the structure of the monoclinic CaAl_2O_4 [13]. There are two six co-ordinated sites where the Ca–O distances (average 2.4 Å) are rather short for the Eu^{2+} ion whereas the third nine co-ordinated site, which has longer Ca–O distances (average 2.8 Å) [14] has thus enough space for the Eu^{2+} ion. The sum of the ionic radii $r(\text{Eu}^{2+}) + r(\text{O}^{2-})$ is 2.57 and 2.7 Å for the Eu^{2+} co-ordination numbers six and nine, respectively [15]. That supports also the preferred occupation of the nine co-ordinated Ca^{2+} site.

The afterglow lifetime of the hexagonal phase was slightly longer than that of the monoclinic one. After the initial nanosecond normal emission of the Eu^{2+} ion, the afterglow decay curves consisted of at least two additional processes, a rapid one prior to 20 min and further on a very slow one. The thermoluminescence glow curves of both the hexagonal and monoclinic $\text{CaAl}_2\text{O}_4:\text{Eu}^{2+}$ phases have a main maximum at about 80 °C followed by a tail extending up to 250 °C. The intensity of the main peak of the hexagonal phase was lower but the high-temperature tail was more intense than that of the monoclinic one. The existence of the high-temperature tail corresponding to deeper traps could explain the longer afterglow decay of the hexagonal phase.

4. Conclusions

The sol-gel method lowered the reaction threshold temperature by ca. 200 °C compared to the conventional solid state reaction. The pure monoclinic $\text{CaAl}_2\text{O}_4:\text{Eu}^{2+}$ phase was not, however, formed below 1200 °C. The metastable $\text{CaAl}_2\text{O}_4:\text{Eu}^{2+}$ phase was successfully prepared by the sol-gel method at 850 °C. The structure of this unconventional CaAl_2O_4 phase was determined as hexagonal.

The luminescence of both $\text{CaAl}_2\text{O}_4:\text{Eu}^{2+}$ phases was blue. The luminescence band of the hexagonal phase had the maximum at a slightly longer wavelength than that of the monoclinic one. The initial afterglow of the hexagonal phase was weaker but the lifetime was longer than that of the monoclinic one. The nature, number and depth of the traps as well as the overall persistent luminescence mechanisms are studied at the moment.

Acknowledgements

Financial support from the University of Turku, the Academy of Finland (project # 50466/2000) as well as from the Graduate School of Materials Research (Turku, Finland) is gratefully acknowledged. Prof. Jussi Valkonen and Dr. Manu Lahtinen (University of Jyväskylä, Department of Chemistry) are acknowledged for the use of X-ray powder diffractometer.

References

- [1] MURAYAMA Y., TAKEUCHI N., AOKI Y., MATSUZAWA T., *Phosphorescent Phosphor*, U.S. Patent 5, 1995, 424, 006.
- [2] PALILLA F.C., LEVINE A.K., TOMKUS M.R., *J. Electrochem. Soc.*, 1968, 115, 642.
- [3] BLASSE G., BRIL A., *Philips Res. Repts*, 1968, 23, 201.
- [4] MATSUZAWA T., AOKI Y., TAKEUCHI N., MURAYAMA Y., *J. Electrochem. Soc.*, 1996, 143, 2670.
- [5] YAMAMOTO H., MATSUZAWA T., *J. Lumin.*, 1997, 72–74, 287.
- [6] JIA W., YUAN H., LU L., LIU H., YEN W.M., *J. Lumin.*, 1998, 76, 77, 424.
- [7] NAKAZAWA E., MOCHIDA T., *J. Lumin.*, 1997, 72–74, 236.
- [8] MOHAMED B.M., SHARP J.H., *J. Mater. Chem.*, 1997, 7, 1595.
- [9] KURIHARA L.K., SUIB S.L., *Chem. Mater.*, 1993, 5, 609.
- [10] ITO S., IKAI K., SUZUKI K., INAGAKI M., *J. Am. Ceram. Soc.*, 1975, 58, 79.
- [11] MOORE R.E., HONG-SANG R., *Bol. Soc. Esp. Ceram. Vidr.*, 1993, 32, 369.
- [12] BLASSE B., GRABMAIER B.C., *Luminescent Materials*, 1994, Berlin, Springer.
- [13] NAKAMURA T., MATSUZAWA T., ROWLANDS C.C., BELTRÁN-LÓPEZ V., SMITH G.M., RIEDI P.C., *J. Chem. Soc., Faraday Trans.*, 1998, 94, 3009.
- [14] HÖRKNER W., MÜLLER-BUSCHBAUM H.K., *J. Inorg. Nucl. Chem.*, 1976, 38, 983.
- [15] SHANNON R.D., *Acta Cryst.*, 1976, A32, 751.

Spectroscopic studies on the inclusion complexes of tetrakis(2-hydroxy-5-nitrophenyl)porphyrin with α -cyclodextrin in solution and in sol-gel matrix*

A.O. RIBEIRO, C.R. NERI, Y. IAMAMOTO, O.A. SERRA**

Rare Earth/Bioinorganic Laboratory, Chemistry Department, FFCLRP, University of São Paulo, Av. Bandeirantes 3900, CEP 14040-901, Ribeirão Preto, Brazil

Tetrakis(2-hydroxy-5-nitrophenyl)porphyrin included in α -cyclodextrin (α -CD) photophysics was studied in aqueous media, in solid state and entrapped in a sol-gel matrix. The equilibrium constant of the pair porphyrin/ α -CD was evaluated as $1.22 \cdot 10^5 \text{ mol}^{-1} \cdot \text{dm}^{-3}$. The nitroporphyrin was reduced to aminoporphyrin, included into the α -CD and then entrapped in the Si-O matrix network. The tetrakisporphyrin maintained its luminescent properties (with emission bands at 658 and 713 nm, excited at 422 nm) in all environments, indicating a structural stability under the experimental conditions.

Key words: tetrakis(2-hydroxy-5-nitrophenyl)porphyrin, aminoporphyrin, α -cyclodextrin, sol-gel, luminescence, inclusion compound, hybrid matrix

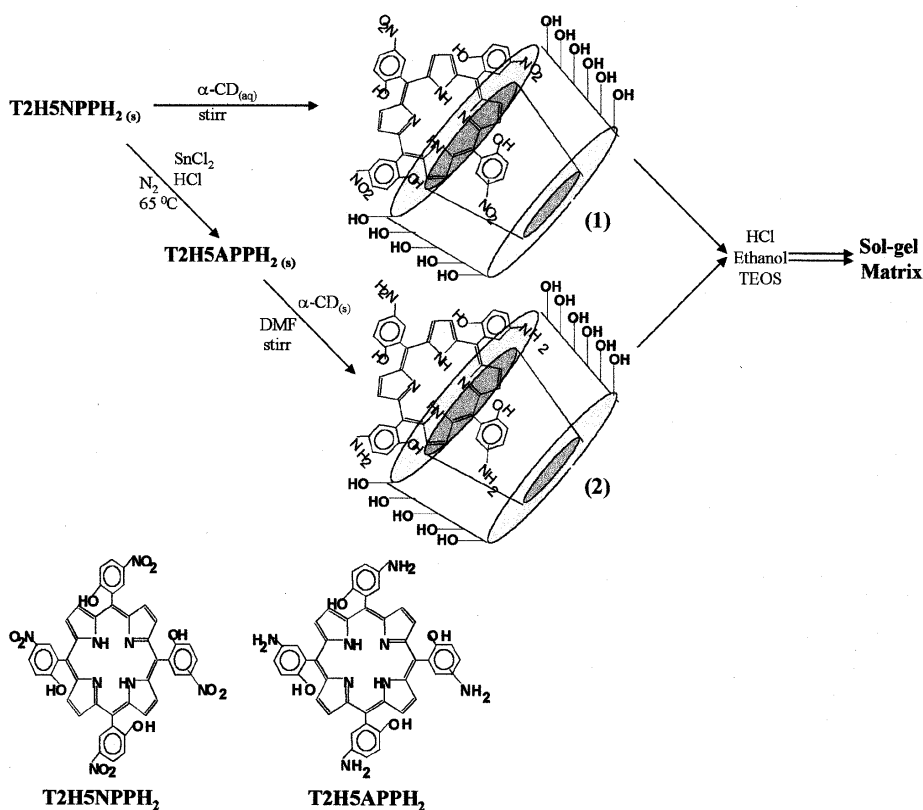
1. Introduction

The central importance of porphyrins in heme proteins has stimulated much interest in their water-soluble derivative model compounds. Porphyrins are investigated and employed in a wide range of fields such as catalysts of oxidation processes, biomimetic compounds, supramolecular devices, in design for new products in medicine and as contrast agents for magnetic resonance imaging [1–4]. Cyclodextrins (CD) are cyclic oligosaccharides composed of 6, 7 and 8 glucose units, named α -, β - and γ -CD, respectively [5–6]. Cyclodextrins are moderately soluble in water and are known to include molecules or fragments in their hydrophobic cavities. This inclusion may perturb the photophysical and photochemical properties of the encapsulated guest molecule [7, 8].

*The paper presented at the International Conference on Sol-Gel Materials, SGM 2001, Rokosowo, Poland.

**Corresponding author, fax: +55-16 633 8151, e-mail: osaserra@usp.br.

Scheme 1



Scheme 1. Preparation route of T2H5NPPH₂ (1) and T2H5APPH₂ (2) α -CD inclusion compounds entrapped in sol-gel matrix

Sol-gel materials popularity results from a number of interesting features, including that they can be manufactured at low temperatures; their microstructure can be controlled to some extent; they are optically transparent and have some other promising properties [9]. The most current methodology consists in the hydrolysis of an alkoxide precursor followed by condensation and polymerization to produce a gel with a continuous inorganic network [10, 11].

In this work we studied the inclusion complex of tetrakis(2-hydroxy-5-nitrophenyl)porphyrin (T2H5NPPH₂) with α -cyclodextrin (1, Scheme 1) in aqueous solution and in a solid state. The solid inclusion compound was studied when it is doped in a rigid sol-gel matrix. Similarly, we also investigated the tetrakis(2-hydroxy-5-aminophenyl)porphyrin (T2H5APPH₂), which we expected to be covalently linked to the α -cyclodextrin (2, Scheme 1).

2. Experimental procedure

α -cyclodextrin and TEOS (tetraethylorthosilicate) were purchased from Aldrich. T2H5NPPH₂ was synthesized as described in [12] and transformed to T2H5APPH₂ by reduction with SnCl₂ and HCl, under nitrogen atmosphere, at 65 °C (FTIR = 1658 cm⁻¹, *n*NH₂) [13]. To obtain the inclusion complex (**1**), a solution of T2H5NPPH₂ in dichloroethane (DCE) was added to a α -cyclodextrin aqueous solution (1:100 molar ratio). The two-phase system were stirred and heated (~40 °C) until all DCE was evaporated and the porphyrin transferred to the aqueous solution. To determine the equilibrium constant (K_1) between the porphyrin and α -CD, 5.0 cm³ of a 3.5·10⁻⁵ mol·dm⁻³ solution of T2H5NPPH₂ in DCE was added into equal volume of α -cyclodextrin aqueous solution at various concentrations (4.9; 3.5; 1.75; 1.05; 0.7; 0.35(×10⁻⁵) mol·dm⁻³). After the porphyrin addition, the UV-Vis absorption spectra were recorded. The solution with a molar ratio 1:100 (T2H5NPPH₂: α -CD) was evaporated and the solid complex was analyzed by excitation and emission luminescence spectroscopy.

In order to prepare solid matrices, 2.0 cm³ of ethanol, 2.0 cm³ of TEOS, 1.0 cm³ of water and 0,750 cm³ of HCl (1.0 mol·dm⁻³) was added into 10.0 mg of T2H5NPPH₂- α -CD and T2H5APPH₂- α -CD complexes, respectively. The resulting solution was stirred for 30 minutes and then allowed to stand at 25 °C. A xerogel with glassy appearance was obtained after 3 days of aging for both complexes. The materials were submitted to absorption in infrared region and luminescence analyses. The absorption spectra (UV-Vis) were recorded on an UV-Vis spectrophotometer (Hewlett Packard 8452 Diode Array). FTIR spectra were recorded for solid materials in KBr pellets, in a Perkin Elmer FT-IR 1600. The luminescence data were obtained in a spectrofluorometer (SPEX Fluorolog III TRIAX550) at room temperature. The fitting curve was obtained by using the ORIGIN[®] program.

3. Results and discussion

The synthetic route for preparation of the inclusion complexes is shown in Fig. 1. To form inclusion complex, T2H5NPPH₂ in DCE was stirred with α -CD in aqueous solution. The equilibrium constant (K_1) was estimated for the formation of 1:1 inclusion complex from the equation [14]:

$$\frac{1}{(A - A_0)} = \frac{1}{a'} + \frac{1}{a'K_1[a - CD]} \quad (1)$$

where a' is a constant. The equation is valid only if the concentration of porphyrin is much lower than the concentration of α -CD.

The absorption UV-Vis spectra of the T2H5NPPH₂- α -CD solutions (maxima at 432 nm), with increasing α -CD concentration, are shown in Fig. 1. The plot of 1/(A-A₀)

against $1/[\alpha\text{-CD}]$ gives a straight line (Fig. 2), and, from this plot ($Y = A + BX$, where $A = 3.88539$, $B = 3.19345 \cdot 10^{-5}$) we evaluate that the K_1 value is $1.22 \cdot 10^5 \text{ mol}^{-1} \cdot \text{dm}^{-3}$. Moreover, this plot suggests the formation of the 1:1 T2H5NPPH₂- α -CD inclusion complex:

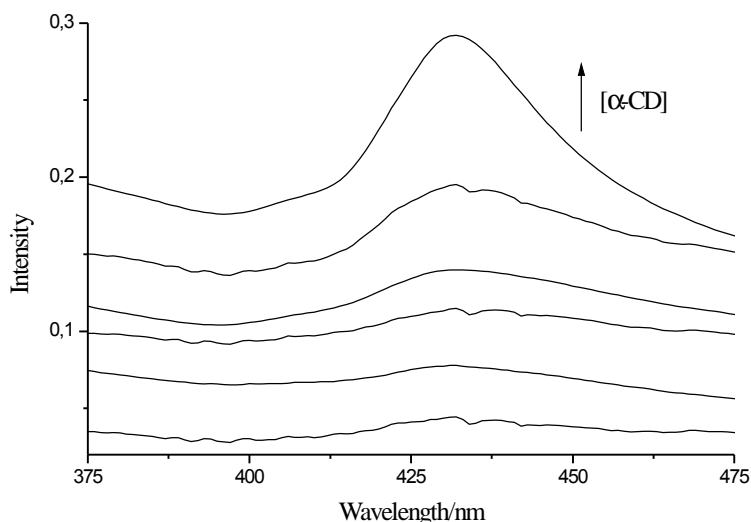
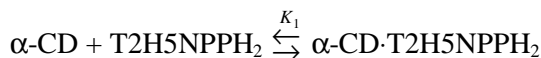


Fig. 1. Absorption spectra of T2H5NPPH₂ ($3.5 \cdot 10^{-5} \text{ mol} \cdot \text{dm}^{-3}$) in aqueous solutions of the following concentrations of α -CD: $0.35 \cdot 10^{-5}$; $0.7 \cdot 10^{-5}$; $1.05 \cdot 10^{-5}$; $1.75 \cdot 10^{-5}$; $3.5 \cdot 10^{-5}$ and $4.9 \cdot 10^{-5} \text{ mol} \cdot \text{dm}^{-3}$

For the inclusion of water-soluble tetrakis(4-sulfonatophenyl)porphyrin in α -CD, Hamai and Koshyama [15] obtained the value of $7.2 \cdot 10^2 \text{ dm}^3 \cdot \text{mol}^{-1}$ for the 1:1 inclusion complex. Also Mosinger et al. [16] found the value of $4.5 \cdot 10^3 \text{ mol}^{-1} \cdot \text{dm}^{-3}$ as the equilibrium constant for same anionic porphyrin into 2-hydroxypropyl α -CD. This higher value for K_1 is consistent with our results, since we observed that the uncharged porphyrin formed a more stable system with the hydrophobic pocket of the CD.

The emission spectra of T2H5NPPH₂ in DCE, T2H5NPPH₂- α -CD inclusion complex (in aqueous solution and in a solid state) and the sol-gel matrix are shown in Fig. 3. The peaks related with these spectra are presented in Table 1. The excitation (at approximately 422 nm) and emission bands (at 658 and 713 nm) are the same in all environments, indicating that the T2H5NPPH₂ maintained its luminescent properties and structural stability under the experimental conditions.

FTIR spectroscopy of the T2H5NPPH₂- α -CD in sol-gel matrix was undertaken to confirm the formation of the Si-O bond (Table 1). The IR spectrum showed a band at 1073 cm^{-1} correspondent to a Si-O stretching mode [17], indicating the formation of the matrix network.

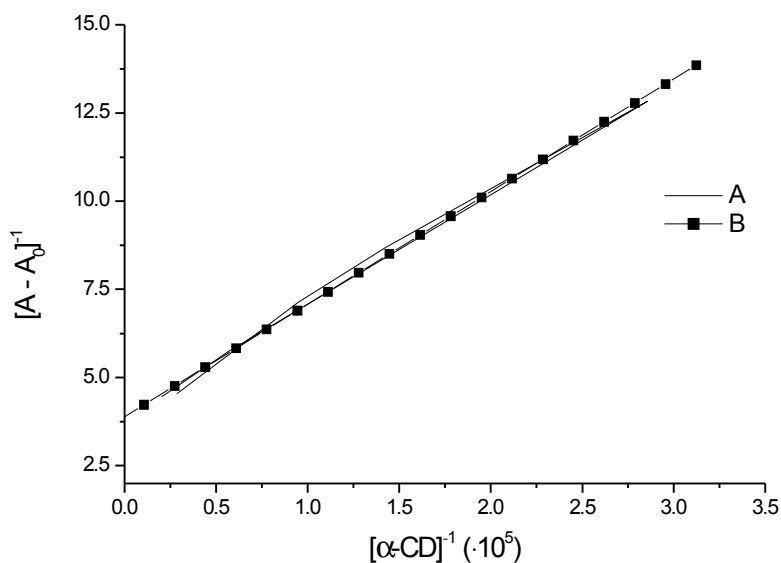


Fig. 2. Doubly-reciprocal plot for the absorbance of T2H5NPPH₂ ($3.5 \cdot 10^{-5}$ mol·dm⁻³) in aqueous solution containing various amounts of α -CD ($\lambda_{\text{obs}} = 432$ nm) (A) and the fitted linear equation $Y = A + B$; $A = 3.88539$ and $B = 3.19345 \cdot 10^{-5}$

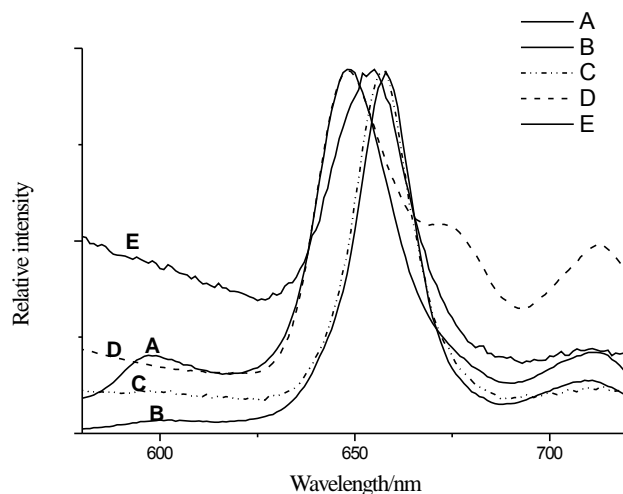


Fig. 3. Emission spectra: T2H5NPPH₂ in DCE (A), T2H5NPPH₂ with α -CD inclusion compound in water (B) and in a solid state (C); T2H5NPPH₂ (D) and T2H5APPH₂ (E) with α -CD inclusion compound in sol-gel matrix

The luminescence spectra of T2H5APPH₂- α -CD showed the maximum peak of excitation at 426 nm and of emission at 648 nm (Fig. 3), similar to the correspondent T2H5NPPH₂. The FTIR spectrum of the T2H5APPH₂- α -CD did not confirm the formation

of a secondary amine bond, what points to the formation of the inclusion complex between α -cyclodextrin and tetrakis(2-hydroxy-5-aminophenyl) [T2H5APP₂- α -CD (2)], that is not covalently bonded. The FTIR band at 1658 cm⁻¹ (ν NH₂ of T2H5APP₂), 1158 cm⁻¹ (group C–O–C of CD) and 3373 cm⁻¹ (group C–OH of CD) confirmed that the structures of porphyrin and cyclodextrin are not modified in the sol–gel process.

Table 1. Excitation and emission maximum and FTIR assignments obtained for T2H5NPPH₂ and T2H5APPH₂ and their inclusion compounds with α -CD in different media

Compound	Excitation I_{\max}/nm	Emission I_{\max}/nm	FTIR [11]	
			cm^{-1}	assignment
α -CD solid	–	–	1154 3400	C–O–C C–OH
T2H5NPPH ₂ in DCE	422	658, 713	–	–
T2H5NPPH ₂ - α -CD (aq)	427	657, 713 (w*)	–	–
T2H5NPPH ₂ - α -CD (s)	425	654, 713 (w)	1582 3403	–NO ₂ C–OH
T2H5NPPH ₂ - α -CD sol–gel matrix	424	598, 648, 713	1073	Si–O
T2H5APPH ₂ - α -CD sol–gel matrix	426	648, 713	1658 1080	–NH ₂ Si–O

*w – weak.

4. Conclusions

T2H5NPPH₂ maintained its luminescent properties in all environments: aqueous media, solid state and in sol–gel matrix, suggesting a structural stability under the experimental conditions. In addition, an enhancement in the emission of T2H5NPPH₂- α -CD in the inorganic matrix has been observed, leading to the conclusion that the use of α -CD is a valid methodology to solubilize organic molecules in order to produce designed luminescent materials by the sol–gel technology.

Acknowledgements

We thank for the financial supports from FAPESP, CAPES and CNPq.

References

- [1] KUMAR K.R., BALASUBRAMANIAN S., GOLDBERG I., *Inorg. Chem.*, 1998, 37, 514.
- [2] CAROFIGLIO T., FORNASIER R., LUCCHINI V., ROSSO C., TONELLATO U., *Tetrahedron Letters*, 1996, 38, 45, 7919.
- [3] YUSHMAMOV V.E., IMASATO H., TOMONIAGA T. T., TABAK M., *J. Inorg. Biochem.*, 1996, 61, 233.
- [4] *The Porphyrin Handbook*, K. M. Kadish, K. M. Smith and R. Guilard (Eds.), 2000, Academic Press.
- [5] MATSUSHIDA Y., HIKIDA T., *Chem. Phys. Letters*, 1999, 313, 85.

- [6] HEDGES A.R., *Chem. Rev.*, 1998, 98, 2035.
- [7] FATIN-ROUGE N., BUNZLI J.G., *Inorg. Chem. Acta*, 1999, 293, 53.
- [8] TABUSHI I., SHIMIZU N., SUGIMOTO T., SHIOZUKA M., YAMAMURA K., *J. Am. Chem. Soc.*, 1977, 99, 7100.
- [9] BRINKER C.J., SCHERER G.W., [in:] *Sol-Gel Science*, 1990, San Diego, Academic Press.
- [10] FUQUA P.D., DUNN B., ZINK J.I., *J. Sol-Gel Sci. Techn.*, 1998, 11, 241.
- [11] RIBEIRO A.O., BIAZZOTTO J.C., SERRA O.A., *J. Non-Cryst. Solids*, 2000, 273, 198.
- [12] NERI C.R., IAMAMOTO Y., SERRA O.A., 23th Annual Meeting of Brazilian Society of Chemistry, (Poços de Caldas – Brazil) 2000, QI 021.
- [13] KRUPER W. J., CHAMBERLIN T. A., KOCHANNY M., *J. Org. Chem.*, 1989, 54, 2753.
- [14] CONNORS K.A., *Binding Constants – The Measurements of Molecular Complex Stability*, 1987, New York, Wiley.
- [15] HAMAI S., KOSHIYAMA T., *J. Photochem. Photobiol., A: Chem.*, 1999, 127, 135.
- [16] MOSINGER J., DEUMIÉ M., LANG K., KUBÁT P., WAGNEROVÁ D.M., *J. Photochem. Photobiol., A: Chem.*, 2000, 130, 13.
- [17] WILLIAMS D.H., FLEMING I., *Spectroscopy Methods in Organic Chemistry*, 4th Ed., 1989, McGraw-Hill, New York.

Highly porous aerogels of very low permeability*

J. PHALIPPOU^{**}, T. WOIGNIER, R. SEMPÉRÉ, P. DIEUDONNÉ

Laboratoire des Verres – UMR CNRS 5587, Université de Montpellier 2,
Place Eugène Bataillon, 34095 Montpellier Cedex 5, France

In this paper, we firstly investigate the way the pores are created in silica gel during gelation. Then we show that the solid particle arrangement acts on the geometrical pore characteristics (pore volume and pore size distribution). According to the pore size value, the permeability of gels is quite low even if the value of the gel porosity exceeds 95%. Analogous properties can be extended to silica aerogels for which now the solvent is replaced by air. Consequently, and according to their low permeability, light weight aerogels exhibit very striking response to mechanical stresses. Here we report unusual experiments allowing us to estimate the mechanical properties of aerogels thanks to their low value of the average pore size. Moreover, one demonstrates that aerogels may be densified at room temperature using an external isostatic pressure. In that case, the pore size may be tailored with respect to the nature and the characteristics of the starting aerogel. The evolution of the textural properties such as the mean pore size and the specific surface area of these tailored aerogels is investigated as a function of isostatic pressure.

1. Introduction

A gel is the result of the setting up of a solid network in a previously homogeneous liquid. As obtained, the gel which occupies the whole volume of starting liquid is a two-phase material. The solid part concerns the network, and the remaining volume is occupied by the liquid. The pore liquid, according to chemical reactions giving rise to the solid, mainly consists of water and alcohol. Consequently, it is called the solvent. Obviously, the solvent is located within the pores of the gel. The liquid may be replaced by air. Such a change, if uncontrolled, leads to a gel shrinkage which deeply modifies the initial texture. The shrinkage, associated to drying, is minimized if drying is performed under supercritical conditions for the solvent.

The gel formation is the final result of a series of elementary reaction steps. The first step is the formation of particles. Then these particles begin to aggregate and resulting clusters stick together to build up the percolating network. Floating clusters,

*The paper presented at the International Conference on Sol-Gel Materials, SGM 2001, Rokosowo, Poland.

** Corresponding author, e-mail: phalippo@crit.univ-montp2.fr.

with time, aggregate to the network. We can say that the texture of the gel network may be considered as achieved when an equilibrium between the solid and liquid chemical species is established.

2. Gel formation

The evolution of the initial liquid toward the gel involves the formation of individual solid particles. These particles appear as a result of a classical nucleation and growth mechanism. However, the nature of the starting solution influences the features of the elementary particles.

Regarding an aqueous solution, the silica solubility is around 100 ppm at room temperature and under neutral conditions. The dissolved silica chemical species are silicic acid molecules, $\text{Si}(\text{OH})_4$, which can easily react together, to give rise to more polycondensed species. According to Iler [1], monomers transform into dimers and higher condensed molecules up to cyclic compounds. The cyclic compounds are assumed to give rise to solid particles as a result of an internal condensation of silanol $\text{Si}-\text{OH}$ groups. The polyion $(\text{Si}_8\text{O}_{20})^{8-}$ is often assumed as the onset of the particle formation [2]. The size of this colloidal particle is of about 1 nm [1].

As soon as the particle is created, it can aggregate with other surrounding ones or it can grow by surface addition of monomers. Obviously, these two mechanisms occur simultaneously. However, their importance mainly depends on the electric charge borne by the particle surface. The electric charge depends on the pH of the solution. The isoelectric point of silica is obtained when particles are in an aqueous solution of pH at about 2. For pH within the range from 8 to 9, the silica particles are negatively charged and the repulsive forces between particles (measured by the zeta potential) are significant.

Consequently, the particles do not collide and the polycondensation between particles is prevented, so the particles grow without aggregation. In such a case the size of particles can reach 30 nm, a value unusually high. Generally, gels obtained by aggregation in aqueous solution are constituted by particles the size of which varies between 5 and 10 nm.

Regarding gels obtained from organometallic compounds, the situation is not so clear. Organometallic compounds of silicon are transformed owing to two chemical reactions of hydrolysis and polycondensation. The hydrolysis reaction must be carried out by adding a solvent in which organic compound and water are miscible. Alcohol is often used. Consequently, the silica solubility depends on the alcohol/water ratio that is evolving when the gelation proceeds. The monomer, which is soluble in alcohol, reacts with water to give rise to chemical species which, according to the condensation reaction, are constituted by an increasing number of $[\text{SiO}_4]$ chemical units. The early solid particles which form in the solution have likely size within the range of 0.5–1 nm. They polycondense very quickly to form the tenuous solid network

of the gel. When the hydrolysis is carried out under weakly acidic or neutral conditions, the size of particles is very small.

Gels prepared from organometallic compounds are the most investigated because they show a high purity and total absence of alkali ions. These cations are known to modify the texture and to induce crystallization if the gel is heat treated. Moreover, with respect to the miscibility of liquids (organometallic compounds/alcohol/water) only a small amount of organosilicon compounds, which transform into solid silica, can be introduced in the starting solution. Gel densities in the range of 0.1 to 0.25 are usually obtained.

In the following sections, we will focus on these kinds of gels or aerogels. The gel establishes according to an aggregation phenomenon of particles. Such aggregation gives rise to a disordered 3D arrangement. The gel texture is generally described by different methods. The first one consists of describing the texture by means of an aggregation of particles having the same size but exhibiting different co-ordination numbers. The second one assumes that these particles are located at the edges of a cubic cell. Another way to build up a structure close to that of gel consists of a cubic cell the edges of which are constituted by cylinders made of dense silica. Recently, description of gel texture has been obtained from computer simulations.

The texture of a gel in its wet state is expected to be preserved by a supercritical drying treatment. The texture of the corresponding aerogel is determined by two experimental characteristics. The first one is the apparent density r_a , which is related to the porosity through the relation:

$$r_r = \frac{r_a}{r_s} = 1 - P \quad (1)$$

where r_r is the relative density, r_s the skeletal density (2.2 g/cm³ for silica gel) and P – the porosity.

Figure 1 shows the apparent density as a function of the volume occupied by one gram of gel.

On the other hand, for particles having the same size, the mean co-ordination number \bar{n} of a particle is related to the porosity by the relation [3]:

$$\bar{n} = 2 \exp 2.4(1 - P) \quad (2)$$

which indicates that the mean co-ordination number approaches 2.0 when the porosity approaches 100%. In that case, the texture consists only of linear chains of infinite length.

The texture of gel depends on the aggregation of particles. The mean co-ordination number is within the range from 2 to 3. This value corresponds to a special sequency of particle assembly (Fig. 1).

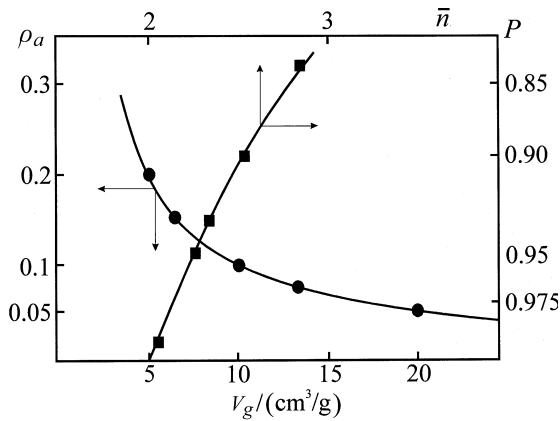


Fig. 1. Bulk density r_a (or porosity P) as a function of the volume occupied by 1 g of a gel; \bar{n} is the mean co-ordination number of elementary particle and V_g the porous volume

Hence, for a porosity of 95%, corresponding to an aerogel having a bulk density of 0.11 g/cm^3 , the mean co-ordination number is 2.25. Such a value can be expressed by a sequence of particles for which the number of particles having a co-ordination number of 2 is 3 times higher than that having a co-ordination number of 3. Hence a sequence 3-2-2-3 would describe the texture of the gel (Fig. 2).

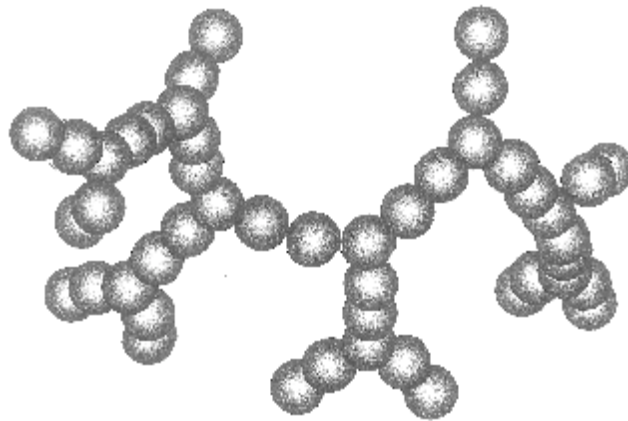


Fig. 2. Schematic texture of a hypothetical gel of a density of 0.11 g/cm^3

The second textural characteristic is the specific surface area S . It is generally obtained from nitrogen adsorption experiments performed at 77 K.

The geometric specific surface area is related to the particle size by the relation:

$$S = \frac{3}{R r_s} \quad (3)$$

where R is the radius of particles. Figure 3 shows that the particle size is directly estimated from the specific surface area. However, the experimental surface area is

lower than the geometric one, according to the fact that the adsorbed molecule cannot cover the whole particle surface [4]. An area is lost at the contact between assumed spherical non intersecting particles. A more precise value of the particle radius is obtained using the equation:

$$R = \frac{1375 - \sqrt{(1375)^2 - 4S \times 128.9\bar{n}}}{2S} \quad (4)$$

where R is expressed in nm and S in $\text{m}^2 \cdot \text{g}^{-1}$.

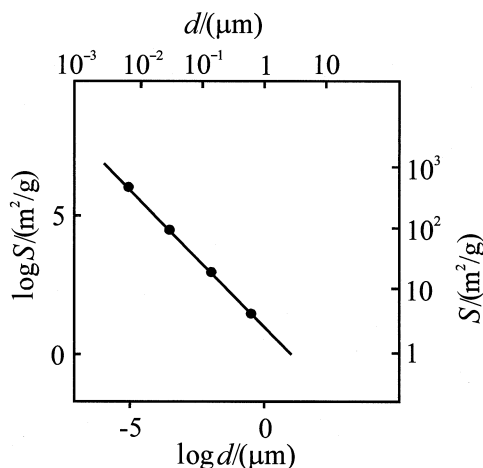


Fig. 3. Specific surface area S as a function of particle size d

Given the specific surface area ($400 \text{ m}^2 \cdot \text{g}^{-1}$) of the previously selected aerogel, the particle size would be of 6.7 nm as estimated from the Eq. (3), while Eq. (4) provides a value of 6.4 nm. Considering that the pore has a dimension of a few particles [5], the pore diameter should be within the range of mesoporosity, easily measured using adsorption–desorption isotherm according to the BJH theory [6].

The model of the cubic cell, the edges of which consist of a chain of pearls, is shown in Fig. 4a. The porosity is related to the number x of spheres located between those forming the vertices of an edge by the relation:

$$r_r = 1 - P = \frac{\pi(1+3x)}{6(1+x)^3} \quad (5)$$

For the selected sample $x = 2$ and the number of particles forming the edge is 3.

Obviously, assuming that there are no necks between particles which are in contact, the specific surface area ($400 \text{ m}^2 \cdot \text{g}^{-1}$) leads to previously calculated particle size (i.e., 6.7 nm). Hence, the edge of the cell has a dimension of 33.5 nm.

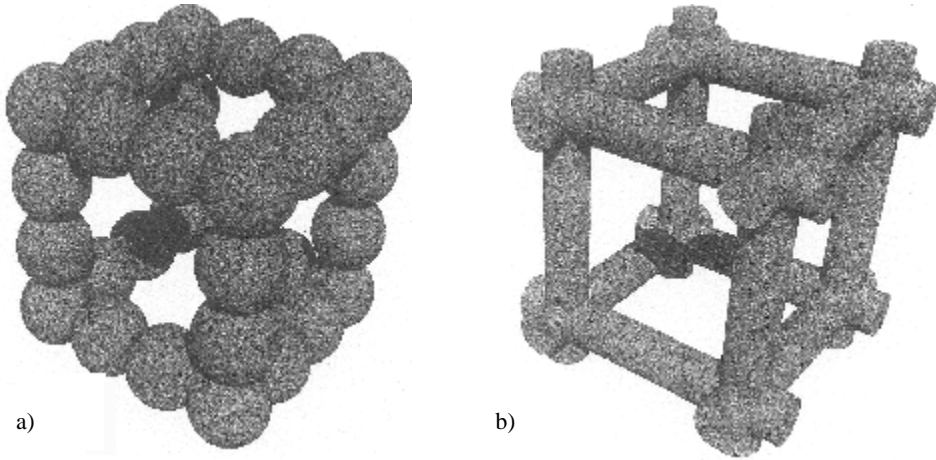


Fig. 4. Geometric models proposed for the gel texture:
 a) the edges in the form of a chain of pearls, b) cubic cell made of cylinders

Assuming that the pores within the cell (Fig. 4a) can be described by a cylinder, the diameter d_p of the pore corresponds to a circle which can be inscribed in the face of the cell:

$$d_p \approx 27 \text{ nm}$$

Identical calculations can be done using the model of cubic cell made of cylinders [7]. In that case, the porosity is related to the cylinder length l and the cylinder radius a by the relation:

$$r_r = 1 - P = 3\pi \frac{a}{l} - 8\sqrt{2}a^3 \quad (6)$$

In addition, the specific surface area is given by:

$$S = \frac{1}{ar_s} \left[\frac{6\pi l - 24\sqrt{2}a}{3\pi l - 8\sqrt{2}a} \right] \quad (7)$$

The two relations allow us to estimate cell parameters. Given the above reported values of the porosity and of the specific surface area, the cylinder length is equal to 29.5 nm and the cylinder radius equal to 2.1 nm. Consequently, corresponding pore diameter is 25.3 nm, a value close to the previous one.

The last manner to describe the texture of a gel is to simulate such a material using computer models. Computer simulations have been previously used to account for the fractal geometry of gel textures. It has been demonstrated that a fractal dimension of 1.8 is obtained for a diffusion limited cluster–cluster aggregation. Such a fractal di-

mension corresponds well to base-catalysed aerogels. On the other hand, reaction limited cluster–cluster aggregation gives rise to a fractal dimension higher than 2 [8]. The simulated obtained network is expected to describe neutral or acidic catalysed gels.

Small angle X-ray or neutron scattering experiments [9] allow us to measure the fractal dimension. Additionally, the cross over between the fractal and the Porod's regime indicates the size of elementary particles. It has been previously found that the particle size varies between 0.4–0.6 nm for neutral-catalysed aerogels and 1–2 nm for base-catalysed aerogels. The mean pore size may be roughly estimated from the models. It is in the range of 10–50 nm [10].

3. Pore size determination

Up to now, a crude estimate of a mean pore size has been derived with respect to the models. The pore size mainly depends on two parameters: the size of primary particles and the porosity. To summarize, the mean pore size of a gel is within the mesopore domain.

The pore size can be estimated from different techniques. The literature reports a few experiments performed using ^1H NMR in the wet state [11, 12]. This technique permits to separate different kinds of water molecules and the interactions spin–network and spin–spin may be used to identify the amount of water molecules which are located at the surface and those which, located within the pore, diffuse freely. The respective amounts are calculated with the aid of a quite simple model [12], whose application to gels is questionable. The second method used to estimate the pore size distribution is called thermoporometry. It is based on the fact that water within the pores crystallises at the temperature decreasing with the pore size, or more precisely – as a function of the curvature radius of a pore [13]. This technique shows that the mean pore size is related to the sample nature but remains in the mesopore (1–30 nm) range [14].

It is worth noticing that those two mentioned techniques require a gentle solvent exchange to fill the pores with water molecules. Sometimes the solvent exchange induces a network dimensional change. In that case, an experiment with a solvent other than water is needed.

Supercritical drying is a process which allows one to dry the gel theoretically without shrinkage. That occurs in fact for base-catalysed gels which are formed of large particles connected together by large necks. Neutral or acidic gels generally shrink a little during this drying treatment. It is obvious that the texture of aerogels can be analysed by usual adsorption–desorption isotherms of nitrogen (or argon). Both the BET theory [15] for specific surface area and the BJH theory for the pore size distribution are widely used. They confirm that the specific surface area varies between 200 and 800 $\text{m}^2\cdot\text{g}^{-1}$ while the pore size distribution spans over a range of 5–30 nm. Recent work demonstrated that these experiments must be carried out with care with respect to the dimensional changes which occur during experiments [16].

It is worth noticing that accurate transmission electron microscopy experiments provide also information about the pore size [17, 18].

The characteristic features of gels are summarized below:

- gels are materials of a low solid content,
- the main phase is fluid (liquid or gas),
- due to a high porosity the elastic moduli are quite small,
- even if the mechanical strength is relatively low, the associated strain is considerable.

A gel exhibits pronounced strains when subjected to very small stresses. In addition, its specific surface area is large and the mean pore size is in the range of mesopores. Consequently, the solid chains of the gel network are very close and are highly reactive with respect to the specific surface.

4. The permeability and its measurement

The permeability D of a porous material having open porosity is a property which accounts for ability of a fluid to go through it.

The fluid flow through a porous material is expressed by Darcy's law:

$$J = -\frac{D}{h} \nabla P \quad (8)$$

Here the flow is considered as laminar. The flux J is inversely proportional to the liquid viscosity h . It depends also on the pressure gradient ∇P applied to liquid. Such a relation applies quite well to liquids flowing through gels. It also accounts for gas diffusion through aerogels. However, for very dense aerogels or partially densified aerogels, the flux corresponds to a peculiar regime called molecular or Knudsen regime. Such a regime establishes when the mean free path of gas molecule becomes higher than the pore diameter [10, 19, 20].

A common way to measure the permeability of a porous material is to estimate the amount of liquid which passes through it per unit of time (Fig. 5).

The experiment works very well for typical porous material. However, because of the small pore sizes, gels show low permeability. In such a case, the flux of liquid is difficult to measure. Usually to improve the measurement of the amount of liquid which flows through the sample the level of liquid is measured using a capillary tube. Moreover, to speed up the experiment a pressure is often applied to the liquid. Unfortunately, for very weakly permeable and compliant material, the pressure causes bending of the sample. The upper part of the material is under a compressive stress. As a result, the size of pores locally reduces and the permeability measurement is erroneous. In addition, the capillary tube may play a role analogous to that of a thermometer and the liquid level can vary according to room temperature, when not precisely controlled.

The gel permeability is easily measured by the thermal expansion method [21]. This method takes advantage of the low mechanical properties of gels. Details of the experimental set-up were previously reported [21]. In few words, the gel containing a non-reactive liquid like alcohol is rapidly heated. During this heating run, the liquid within the pores has no time to escape out of the solid network. It is under compressive stress and, in turn, the solid network is under tensile stress. Because of the low elastic properties of the network, the net result is a solid expansion. If the gel is then maintained at the constant temperature, the liquid has now plenty of time to leave the pores. Consequently, the solid network is under a decreasing stress. The sample contracts down to its initial dimension. Scherer et al. [21] have demonstrated that the experimental curve may be fitted with a theoretical equation containing a hydraulic relaxation time t . This time contains parameters related to the liquid and the solid phases, respectively.

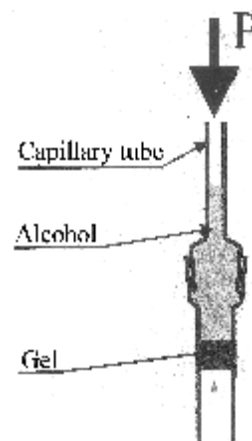


Fig. 5. Usual apparatus allowing the measurement of the permeability of porous material

$$t = \frac{ha^2}{DM} \quad (9)$$

In this expression a is the radius of the rod of a gel and M is the modulus associated with the propagation of longitudinal waves. M is related to the bulk compression K and the shear G moduli according to:

$$M = K + \frac{4}{3}G \quad (10)$$

A simple and elegant method to measure the permeability is the method of three-point bending which does not require special equipment [22]. A sample (cylindrical or prismatic) of gel is suddenly stressed to be deformed down to a selected strain value. In the first instant, the liquid cannot escape from the gel and, consequently, one can say that the sample deforms but its whole volume remains constant. Thus, the sample behaves as an incompressible fluid. The Poisson coefficient is 0.5 and the apparent Young's modulus E_a :

$$E_a = 2G(1+n) = 3G \quad (11)$$

corresponds to the value of three shear moduli.

Obviously, with time, the liquid can leave the upper compressed surface and enter the lower surface under tension. The Poisson coefficient is 0.2 and the real Young's modulus equal to $2.4G$ is then obtained.

Scherer [22] shows that the curve $W(t)/W(0)$ (where W is the force applied) as a function of time may be fitted with a mathematical expression containing a relax a-

tion time parameter. This parameter, as indicated before, contains the permeability of a gel. The permeability of gels depends obviously on their nature. For acid-catalysed gels, the permeability is in the range of 10 nm^2 . It is twice as high for base-catalysed aerogels. These values confirm a very low permeability of gels. This is the main property responsible for gel cracking occurring during several steps of drying process. For a classical drying, the gel shrinks until the liquid at the network surface enters the pores. During this first step, the liquid flux is driven by the liquid evaporation rate V_E , which can be expressed as the weight loss per unit of time:

$$V_E \propto J = \frac{D}{h} |\nabla P| \quad (12)$$

Consequently, in the case of fast evaporation rates and because of the low gel permeability, the pressure (or stress) gradient between the liquid located at the surface and that in the sample core is high enough to induce cracking [23].

Cracking of large pieces of gels during supercritical drying is also related mainly to permeability, mechanical strength and sample dimensions. The first step of supercritical drying consists of heating the gel in an autoclave. During heating, an expansion is expected. In the case of large pieces of a gel and too fast heating rate, cracking will be observed [24]. Shapes of the cracks are associated with the gel shrinkage. For acid-catalysed gels the shrinkage leads to formation of gels surrounded by syneresis liquids. During heating the liquid flows out freely in all directions. The cracks of the gel do not have a preferred direction. Conversely, a base-catalysed gel does not shrink. Thus, during heating the liquid expands the gel which comes into contact with the walls of an autoclave. Hence, the liquid can only escape through the top surface. Consequently, the gel is under pure tensile stress. It cracks into several slices of about the same thickness (Fig. 6).

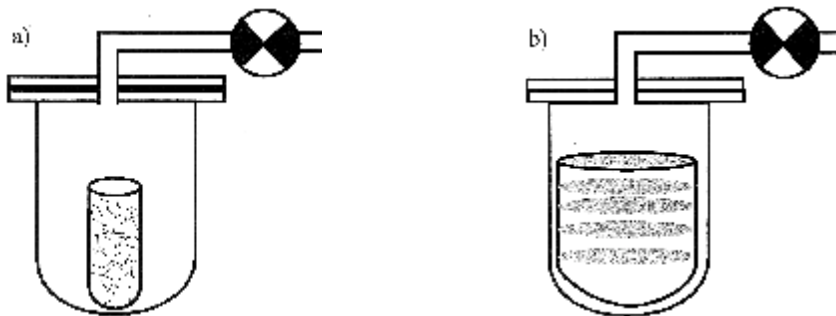


Fig. 6. Cracking of a) neutral- or acid-catalysed gel associated to thermal expansion inside an autoclave, b) base-catalysed gel treated under analogous conditions

In the supercritical drying process when the pressure and temperature are higher than those corresponding to the critical point of the solvent, a supercritical fluid is

obtained. A valve is open to depressurize the autoclave and, consequently, to transform supercritical fluid into gas. If the valve opening is too fast, the superfluid inside the gel remains at a pressure higher than that of superfluid surrounding the sample. The pressure gradient can lead to gel cracking.

5. Advantages of such weakly permeable and porous materials

Because of a low solid content, gels are used to store dangerous liquids which will escape slowly if a leak in the container wall occurs [25]. There also have been attempts to benefit from the thermal insulating properties of aerogels. Investigations concern translucent silica aerogels and highly transparent aerogel plates which are placed between two glass sheets [26].

Some ultraporous aerogels possess elastic modulus so weak that it is quite difficult to measure it. We can take advantages of the low permeability to estimate bulk modulus. An aerogel placed in a non-wetting liquid such as mercury will not have pores invaded by the surrounding liquid. For other porous materials, as the pressure applied to mercury increases, pores having smaller and smaller size will be filled by mercury. For aerogels the mercury cannot enter pores due to their small size. The net effect of the applied pressure is to shrink the sample. In the elastic regime:

$$K = -V \frac{dP}{dV} \quad (13)$$

the bulk modulus K is evaluated from the inverse of the slope of the curve describing the variation of the volume sample as a function of applied pressure [27] (Fig. 7).

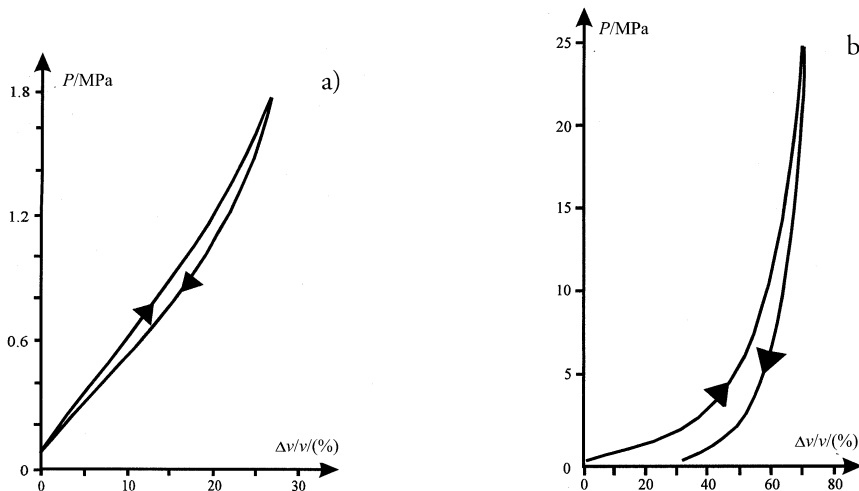


Fig. 7. Relative volume shrinkage as a function of isostatic pressure:
a) elastic regime, b) densification regime

Otherwise, subjecting an aerogel sample to a relative high pressure leads to irreversible volume shrinkage – a real densification occurs [28–30]. Such a room temperature densification depends on the nature of the chemical species covering the pores surface. In order to better understand the densification mechanism a set of base-catalysed fractal aerogels has been prepared. Samples were investigated using small angle X-ray scattering [31]. The curve of the scattering intensity $I(\mathbf{Q})$ as a function of the wave vector \mathbf{Q} on a log scale shows that the slope in the fractal range remains unchanged. The fractal dimension does not vary. The cross-over between the fractal and the Porod's range is not shifted with densification. Thus, the size of primary particles is not modified by room temperature densification resulting from isostatic compression. Note that densification performed by sintering heat treatment leads to the increase in the size of primary particle. The only variation observed concerns the correlation length x which firstly shows a considerable decrease, then tends to a constant value as the sample density increases.

It has been suggested that under compression pressure the fractal blobs interpenetrate. Such a phenomenon requires to break a few chains to permit a better cluster interpretation, but also an increase of the bonds which are created when silanol groups beared by two different chains come into contact. In the first instants the damage caused by bond breaking induces a little decrease of the elastic modulus and correlatively an increase of internal friction [32]. Obviously, for a more pronounced densification, the created bonds become very numerous, the entanglement increases inducing an enhancement of elastic constants.

With respect to this proposed mechanism – mesopores having the largest size and which are likely located between the fractal blobs must disappear first. In order to investigate the pore size distribution as a function of densification, nitrogen adsorption–desorption experiments have been carried out and the pore size obtained from the BJH theory.

During densification a pronounced decrease of the mean size of mesopore is observed (Fig. 8a) while their distribution narrows (Fig. 8b).

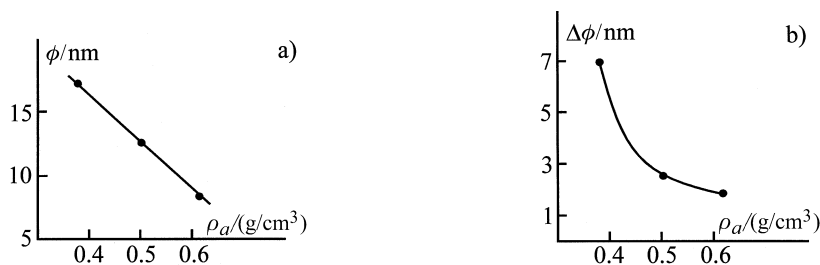


Fig. 8. Density dependence of: a) the mean pore size f , b) the width at middle height Δf of the pore size distribution

Another very striking property of these room-temperature densified aerogels is related to the non-variation of the primary particle size. Obviously, with densification,

the number of particles cannot evolve and consequently the specific surface area remains unchanged [33, 34]. Thus a novel family of materials is obtained. For a given mass of aerogels, the developed surface no more depends on the bulk density. Hence, densified aerogels have a reduced total volume but they exhibit the same specific surface. In other words, the surface per unit volume of material increases as the density rises (Fig. 9).

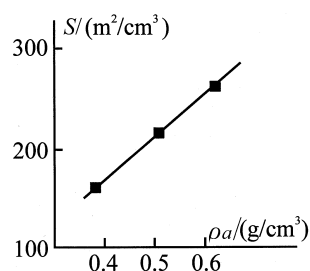


Fig. 9. Evolution of the surface S developed by one cubic centimetre of compressed material as a function of bulk density r_a

6. Conclusion

Gels and aerogels are very porous materials. They have low permeability which decreases as the material shrinks. Any process intended to transform or to modify the gel must be considered according to this specific property. Low permeability has been demonstrated to be useful for determination of elastic properties of very brittle aerogels and to densify them at room temperature. During densification by compression, as the pressure increases, aerogels show the following properties:

- The specific surface area remains constant.
- The elastic constants increase.
- The distribution of pore size narrows.

Aerogels which are room temperature-densified and which additionally exhibit a high specific surface are likely able to sinter easily. Fully dense silica glass is expected to be obtained at a very low sintering temperature and for a low duration of time.

Moreover, the mean pore size may be varied according to the isostatic pressure value. Pore surface may be covered by guest compounds. Such host material can be then thermally sintered to obtain doped silica glass.

References

- [1] ILER R.K., *The chemistry of silica*, 1971, New York, Wiley, p. 484.
- [2] ENGELHARDT V.G., ALTENBURG W., HOEBBEL D., WIEKER W.Z., *Anorg. Allg. Chem.*, 1977, 418, 43.
- [3] MEISSNER H.P., MICHAELS A.S., KAISER R., *Ind. Eng. Chem. Process. Des. Div.*, 1964, 3, 202.
- [4] AVERY R.G., RAMSAY J.D.F., *J. Coll. Int. Science*, 1973, 42 (3), 597.
- [5] RAMSAY J.D.F., AVERY R.G., *Br. Ceram. Proc.*, 1986, 38, 275.
- [6] BARRET E.P., JOYNER L.G., HALENDA P.P., *J. Am. Ceram. Soc.*, 1938, 60, 309.
- [7] SCHERER G.W., *J. Am. Ceram. Soc.*, 1977, 60, 236.
- [8] MEAKIN P., JULLIEN R., *J. Chem. Phys.*, 1988, 89 (1), 246.
- [9] WOIGNIER T., PHALIPPOU J., VACHER R., *J. Mater. Res.*, 1989, 4, 688.
- [10] HASMY A., BEURROIES I., BOURRET D., JULLIEN R., *Europhys. Lett.*, 1995, 29, 567.
- [11] BROWNSTEIN K.R., TARR C.E., *J. Mag. Resonance*, 1977, 26, 17.

- [12] GALLEGOS D.P., MUNN K., SMITH D.M., STERMER D.L., J. Colloid. Inter. Science, 1987, 119, 127.
- [13] BRUN M., LALLEMAND A., QUINSON J.F., EYRAUD C., Thermochim. Acta, 1977, 21, 59.
- [14] DUMAS J., QUINSON J.F., SERUGHETTI J.J., J. Non-Cryst. Solids, 1990, 125, 244.
- [15] BRUNAUER S., EMMET PH., TELLER E., J. Am. Ceram. Soc., 1938, 60, 309.
- [16] REICHENAUER G., SCHERER G.W., J. Non-Cryst.Solids, 2000, 277, 162.
- [17] BOURRET D., Europhys. Lett., 1988, 6–8, 731.
- [18] RUBEN G.C., HRUBESH L.W., TILLOTSON T.M., J. Non-Cryst. Solids, 1995, 186, 209.
- [19] GROSS J., REICHENAUER G., FRICKE J., J. Phys. D, Appl. Phys., 1988, 22, 1447.
- [20] BEURROIES I., BOURRET D., SEMPÉRÉ R., DUFFOURS L., PHALIPPOU J., J. Non-Cryst. Solids, 1995, 186, 328.
- [21] SCHERER G., HDACH H., PHALIPPOU J., J. Non-Cryst. Solids, 1991, 130, 157.
- [22] SCHERER G.W., J. Non-Cryst. Solids, 1992, 142, 18.
- [23] BRINKER C.J., SCHERER G.W., *Sol-Gel Science*, Academic Press, 1990, New York, p. 453.
- [24] PHALIPPOU J., SCHERER G.W., WOIGNIER T., BOURRET D., SEMPÉRÉ R., J. Non-Cryst. Solids, 1995, 186, 64.
- [25] PAJONK G., TEICHNER S.J., *Principles and applications of pore structural characterization*, Haines and Rossi-Dorier (Eds.), 1985, Bristol, J.W. Arrosmith, p. 227.
- [26] FRICKE J., J. Non-Cryst. Solids, 1988, 100, 169.
- [27] DUFFOURS L., WOIGNIER T., PHALIPPOU J., J. Non-Cryst. Solids, 1996, 154, 283.
- [28] PIRARD R., BLACHER S., BROUERS F., PIRARD J.P., J. Mater. Res., 1995, 10, 2114.
- [29] SCHERER G.W., SMITH D.M., QIU X., ANDERSON J., J. Non-Cryst. Solids, 1995, 186, 316.
- [30] DUFFOURS L., WOIGNIER T., PHALIPPOU J., J. Non-Cryst. Solids, 1995, 186, 321.
- [31] BEURROIES I., DUFFOURS L., DELORD P., WOIGNIER T., PHALIPPOU J., J. Non-Cryst. Solids, 1998, 24, 38.
- [32] CALAS S., LEVELUT C., WOIGNIER T., PELOUS J., J. Non-Cryst. Solids, 1998, 225, 244.
- [33] DIEUDONNÉ PH., PHALIPPOU J., J. Sol-Gel Science and Techn., 1999, 14, 1.
- [34] DIEUDONNÉ PH., DELORD P., PHALIPPOU J., J. Non-Cryst. Solids, 1998, 225, 220.

Structure, spectroscopy and dielectric properties of BaTiO₃:Eu³⁺ nanocrystallites prepared by the sol–gel method*

D. HRENIAK¹, E. ŁUKOWIAK¹, K. MARUSZEWSKI^{1,2**}, R. PAŹNIK³, W. STRĘK¹

¹Institute for Low Temperature and Structure Research, Polish Academy of Sciences, Wrocław, Poland

²Mechanical Faculty, Institute of Materials Science and Applied Mechanics,
Wrocław University of Technology, Wrocław, Poland

³Chemistry Department, Opole University, Opole, Poland

Eu³⁺-doped BaTiO₃ nanocrystalline powders have been obtained by sol–gel method. Their morphology, structure and dielectric properties have been investigated as a function of sintering temperature. The powders sintered at the temperatures below 800 °C demonstrate luminescence behaviour characteristic of the inversed symmetry Eu³⁺ sites, where only the ⁵D₀ → ⁷F₁ transitions are allowed. Above this temperature the system undergoes a phase transition characterized by lack of inversion symmetry enabling the dipole–electric transitions.

Key words: barium titanate, europium, nanocrystallites, sol–gel processing, luminescence

1. Introduction

Barium titanate (BaTiO₃) is a classical example of a ferroelectric crystalline material. The BaTiO₃ ceramics are widely applied in electronic devices as high-permittivity capacitors, infrared detectors or transducers. It is well known that ferroelectric and optical properties of ferroelectric ceramics depend on the grain size [1]. Recently, the sol–gel route has been suggested for preparation of transparent, nanostructured BaTiO₃ monolithic xerogels [2]. The size-dependence of the ferroelectric phase transition of small BaTiO₃ particles has been a subject of many reports [3–10]. The ferroelectric crystal size of about 50 nm has been reported [7] as critical for ferroelectric properties.

*The paper presented at the International Conference on Sol-Gel Materials, SGM 2001, Rokosowo, Poland.

**Corresponding author, e-mail: marusz@int.pan.wroc.pl.

In this paper, we present the preliminary studies of structural, optical and dielectric properties of BaTiO₃ nanocrystallites (nc-BaTiO₃) doped with Eu³⁺ ions. They were prepared by the modified sol–gel method. It is well known that for crystal structure evaluation of crystalline materials X-ray powder diffraction (XRD) is used quite often. However, in the case of nc-BaTiO₃ it is not a sensitive enough technique to unravel subtle structure characteristics existing in the nanoscale range. It has been reported that XRD measurements were used only to probe global structure for BaTiO₃ crystallites [8]. However, there exist methods which are more suitable for investigation of local structure and symmetry changes: combination of XRD and Raman scattering [7, 8] or infrared spectroscopies [11], measurements of the second harmonic-generation [8, 12] and photoluminescence studies [13]. We employed the europium(III) ion as an optical probe for structural investigations and detection of phase transitions in the nanocrystalline grains. The fluorescence properties of the europium(III) ion were investigated as a function of the sintering temperature. The basic dielectric properties of Eu³⁺: BaTiO₃ nanocrystalline powders were determined.

2. Experimental

2.1. Preparation

The europium-doped BaTiO₃ crystalline powders were prepared by the sol–gel method similar to that described by Tian et al. [14]. Barium acetate Ba(CH₃COO)₂ (Aldrich 99%), titanium butoxide Ti(OC₄H₉)₄ (Alfa Aesar 99+%) and europium oxide Eu₂O₃ (Koch-Light Laboratories 99.99%) were used as starting materials. Acetyl acetone C₅H₈O₂ (Aldrich 99+%) and acetic acid (POCh p.a.) were selected as solvents of titanium butoxide and barium acetate, respectively. Europium chloride EuCl₃·6H₂O was obtained by reacting stoichiometric amount of europium oxide with hydrochloric acid of analytical grade (POCh). Dissolved barium acetate was added dropwise to titanium butoxide solution under stirring. The obtained solutions were vigorously stirred at 50 °C for about 2 h. The europium salt was dissolved in small amount of water and added slowly to the obtained transparent, yellow sol with 1 molar percent of Eu vs. BaTiO₃. The obtained solution was heated at approximately 100 °C for 24 h to form barium titanate (BT) gel powders. The samples of crushed gels were heated at 750 °C (A), 800 °C (B), 900 °C (C), 1100 °C (D) and 1200 °C (E). Pure, undoped samples of nc-BaTiO₃ were obtained in a similar manner.

2.2. Apparatus

Fluorescence spectra were recorded on an Ocean Optics SD 2000 spectrophotometer. Decay curves of luminescence were recorded with a Jobin-Yvon TRW 1000 spectrophotometer equipped with a photomultiplier (Hamamatsu R928). XRD diffractograms were measured using CuK α source radiation on a DRON-3 powder

diffractometer. The mean crystallite diameters were estimated applying the Scherrer formula [15] to the X-ray diffraction patterns. Electrical properties were measured using computer-based apparatus for dielectric measurements in the frequency range 100–1 MHz.

3. Results and discussion

3.1. XRD measurements

The x-ray diffraction results of the undoped samples as a function of heating temperatures are shown in Fig. 1. The recorded patterns show that all the samples were well crystallized. The nanocrystalline particle sizes were estimated to be 24–30 nm for the samples A, B, C and about 43 nm for the samples D and E. Sharp peaks in all the recorded XRD patterns could be ascribed to pseudocubic paraelectric phases [16] which (probably) co-exist with the tetragonal ferroelectric BaTiO₃ phase [17] in the case of D and E.

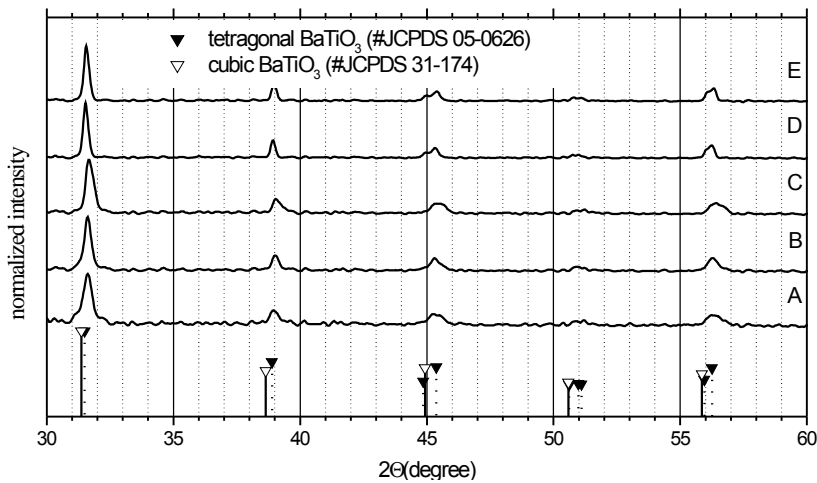


Fig. 1. XRD patterns of BaTiO₃ heated at different temperatures

3.2. Luminescence

The emission spectra of BaTiO₃:Eu³⁺ nanocrystallites prepared at different temperatures and measured at 300 K and 77 K are shown in Fig. 2. The spectra consist of characteristic bands attributed to the ⁵D₀ → ⁷F_J (J = 0, 1–4) transitions. With increasing crystallite sizes the band with the maximum at 616 nm (the hypersensitive electric-dipole ⁵D₀ → ⁷F₂ transition) becomes much weaker as compared to the band with the maximum at 595 nm (assigned tentatively to the magnetic-dipole ⁵D₀ → ⁷F₁ transition). These changes are probably due to the variations in symmetry of the envi-

ronment of the Eu^{3+} ions and may be linked to the structural changes possible for the sample processed at temperatures above 1100 °C.

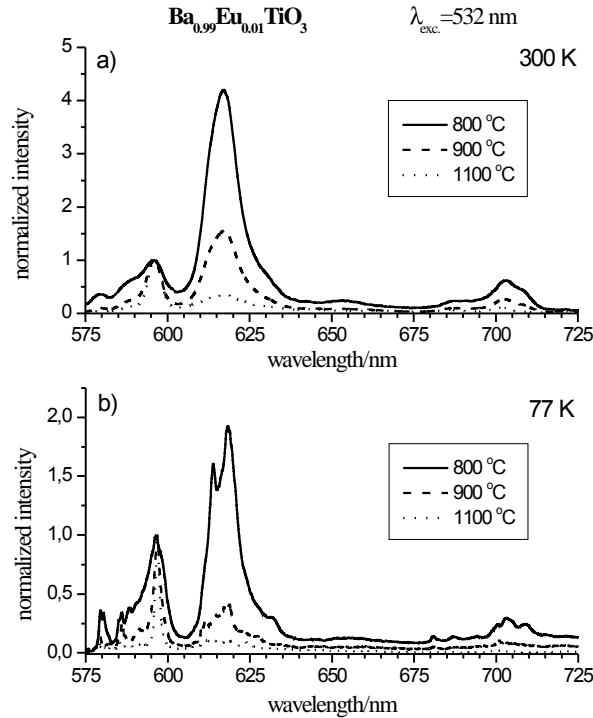


Fig. 2. Emission spectra of Eu^{3+} -doped BaTiO_3 powders prepared at different temperatures

Assuming the existence of the areas with the local tetragonal phase (what is in agreement with the XRD data) it can be assumed that the symmetry changes observed in the Eu^{3+} emission spectra are related to phase transitions occurring in those areas. The europium ions are positioned either inside of those spots. Changes in luminescence spectra and stabilization of the tetragonal phase by Y [19] and Pr [20] ions have been reported for cubic ZrO_2 . The emission spectra measured at room temperature are poorly resolved while the spectra measured at 77 K demonstrate a complex structure characteristic of the multi-site Eu^{3+} spectra.

3.3. Decay time measurements

We have measured the dependence of the emission decay times of the band attributed to the ${}^5\text{D}_0 \rightarrow {}^7\text{F}_1$ transition on the size of the $\text{BaTiO}_3:\text{Eu}^{3+}$ grains. The examples of emission decays measured at 595 nm are shown in Fig. 3. As it can be seen the characteristic decay times increase systematically with increasing temperature. They

are shorter for BaTiO₃ sintered at lower temperatures and the emission decay profiles demonstrate clearly non-exponential character. The shorter decay times recorded for the samples heated at 800 °C and 900 °C may be due to the presence of small amounts of –OH groups in the crystallites leading to quenching of the Eu³⁺ fluorescence. For the samples sintered at higher temperatures (1100 °C and 1200 °C) the emission decays are perfectly exponential and the estimated emission lifetimes are very long ($t = 2.2$ ms at 300 K and $t = 3.5$ ms at 77 K).

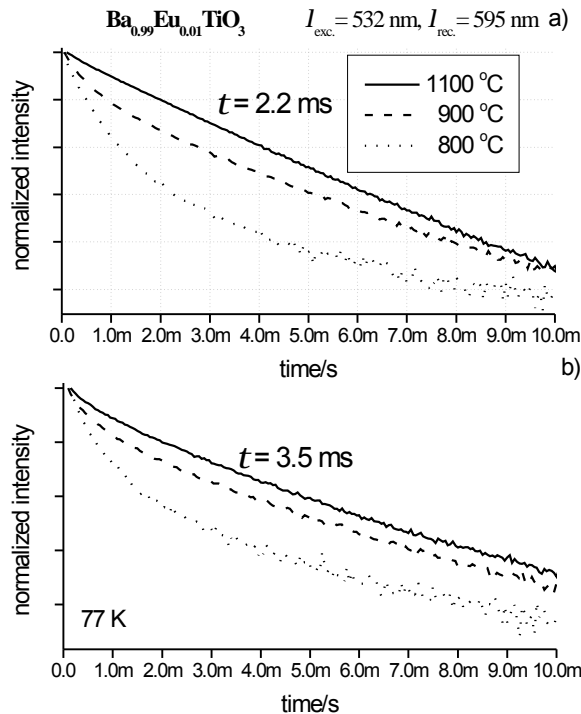


Fig. 3. Emission decay curves of Eu³⁺-doped BaTiO₃ powders prepared at different temperatures. The decays were obtained at 300 K (a) and at 77 K (b)

In our opinion, the characteristic non-exponential decay for samples treated at 800 °C and 900 °C is due to the aggregation of the Eu³⁺ ions, which is more pronounced for smaller grains. Analogous results have been reported for Eu³⁺-doped Lu₂O₃ nanocrystallites [18].

3.4. Dielectric studies

Dielectric studies have been performed in a wide temperature range. The electric permittivity ϵ_r' and dielectric loss $\tan \delta$ have been measured at different frequencies for the undoped BaTiO₃ powders sintered at 800 °C and 1100 °C. During the first

cycle of heating we have observed the maximum of ϵ_r' in the range 300–330 K. This maximum has not been observed in the second (Fig. 4) and successive cycles of heating. This effect results most likely from the material dehydration. There has been observed only a slight change of permittivity during further heating. During cooling of the sample we have observed monotonic decrease of permittivity. In this case we have not observed the maximum in the range of 300–330 K and only a weak temperature dependence of dielectric permittivity. Comparison between the room-temperature values of ϵ_r and $\tan\delta$ at different frequencies is presented in Table 1.

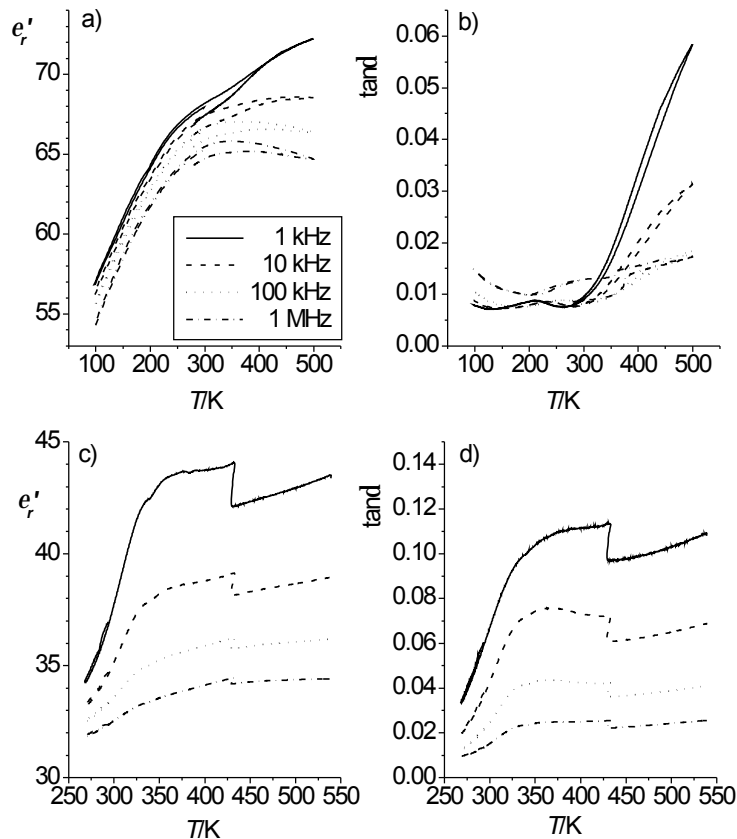


Fig. 4. Temperature-dependency of electric permittivity ϵ_r' and loss tangent $\tan\delta$ of europium-doped BaTiO_3 prepared at 800 °C (a, b) and at 1000 °C (c, d) measured at different frequencies

These results are distinctly different from those obtained for typical ferroelectric BaTiO_3 which exhibits ϵ_r' in the range 10^3 – 10^4 [1]. Undoped samples demonstrated also the hysteresis loops characteristic of ferroelectric materials (Fig. 5), but the value of spontaneous polarization was estimated to be only $1.0 \cdot 10^{-3} \text{ C} \cdot \text{m}^{-2}$. It is almost an order of magnitude smaller than that observed for tetragonal ferroelectric phase

BaTiO₃ monocrystals ($7.5 \cdot 10^{-2} \text{ C} \cdot \text{m}^{-2}$) [1]. This fact indicates that the paraelectric phase dominates in undoped samples.

Table 1. Room temperature values of ϵ_r' and $\tan \delta$ at different frequencies

Frequency/kHz	Sample B (24 nm)		Sample D (43 nm)	
	ϵ_r'	$\tan \delta$	ϵ_r'	$\tan \delta$
1	68	0.009	37	0.065
10	67	0.008	35	0.041
100	66	0.008	33	0.023
1000	65	0.009	32	0.014

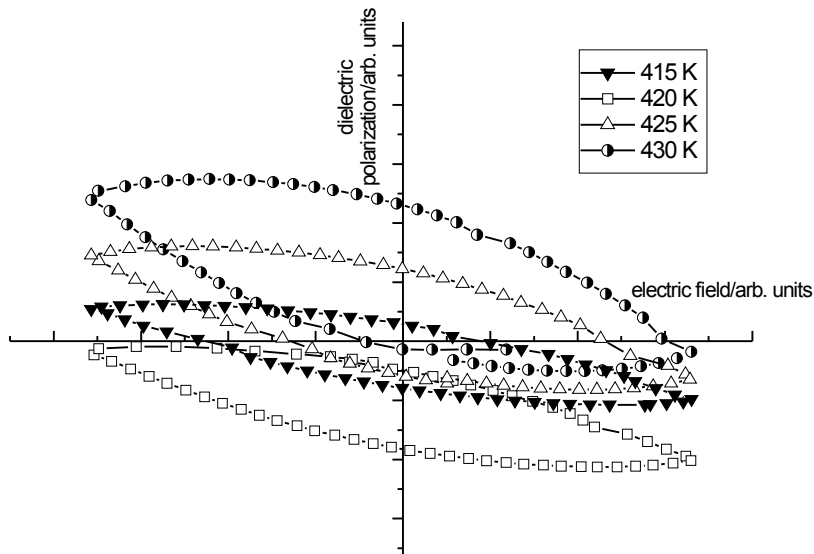


Fig. 5. Ferroelectric hysteresis loops of europium-doped BaTiO₃ obtained at 1100 °C measured at different temperatures

4. Conclusions

The nc-BaTiO₃ nanocrystals doped with Eu³⁺ ions have been obtained by the sol-gel technique. The structure and morphology of the BaTiO₃ grains has been determined. The fluorescence properties of the Eu³⁺ ion were investigated as a function of thermal sintering of the nc-BaTiO₃. It was found that with increasing temperature the intensity of the $^5D_0 \rightarrow ^7F_2$ transition decreased significantly as compared to the $^5D_0 \rightarrow ^7F_1$ transition. Above 1100 °C the second one dominates the spectrum. This suggests that above this

temperature a local phase transition occurs in the material influencing the symmetry of the Eu^{3+} ion sites, being probably rhombohedral at 77 K and tetragonal at 300 K. The synthesized nc-BaTiO₃ can well be described as pseudocubic, with some fraction of the particles retaining ferroelectricity.

Acknowledgements

The dielectric measurements have been performed in the laboratory of Prof. Z. Czaplą at the Institute of Physics, University of Wrocław. This work was partially supported by a KBN grant No. PBZ-KBN-013/T08/45.

References

- [1] NALWA H.S., *Handbook of Low and High Dielectric Constant Materials and Their Applications*, 1999, USA, Academic Press.
- [2] VASILJEV V.A., VOROTILOV K.A., YANOVSKAYA M.I., SOLOVIEVA L.I., SIGOV A.S., *J. Sol-Gel Sci. Techn.*, 1998, 13, 877.
- [3] UCHINO K., SADANAGA E., HIROSE T., *J. Am. Ceram. Soc.*, 1989, 72, 1555.
- [4] SAEGUSA K., RHINE W.E., BOWEN H.K., *J. Am. Ceram. Soc.*, 1993, 76, 1505.
- [5] SHIH W.-H., LU Q., *Ferroelectrics*, 1994, 154, 71.
- [6] SHIH W.Y., SHIH W.-H., AKSAY I. A., *Phys. Rev. B*, 1994, 50, 575.
- [7] ZHANG M.-S., YU J., CHEN W., YIN Z., *Progress Cryst. Growth Charact. Mat.*, 2000, 33.
- [8] FREY M.H., PAYNE D.A., *Phys. Rev. B*, 1996, 54, 3158.
- [9] MCNEAL M.P., JANG S.-J., NEWNHAM R.E., *J. Appl. Phys.*, 1998, 83, 3288.
- [10] AYYUB P., PALKAR V.R., CHATTOPADHYAY S., MULTANI M., *Phys. Rev. B*, 1995, 51, 6135.
- [11] BUSCA G., BUSCAGLIA V., LEONI M., NANNI P., *Chem. Mater.*, 1994, 6, 955.
- [12] LINES M.E., GLASS A.M., *Principles and Applications of Ferroelectrics and Related Materials*, 1977, Oxford, Clarendon.
- [13] ZHANG M.-S., YU J., CHEN W., ZHANG W., YIN Z., *Solid St. Comm.*, 2001, 119, 659.
- [14] HU-YONG TIAN, *Thermochimica Acta*, 2000, 360, 57.
- [15] KLUG P., ALEXANDER L.E., *X-ray Diffraction Procedure*, 1954, New York, Wiley, Chap. 9.
- [16] Joint Committee for Powder Diffractions Standards, Card No. 31-174.
- [17] Joint Committee for Powder Diffractions Standards, Card No. 05-174.
- [18] ZYCH E., HRENIAK D., STREK W., *J. Phys. Chem.*, accepted for publication.
- [19] PAJE S.E., LLOPIS J., *J. Phys. Chem. Solids*, 1994, 55, 671.
- [20] SAVOINI B., MUNOZ SANTIUSE J.E., GONZALES R., *Phys. Rev.*, 1997, B 56, 5856.

Optical behaviour of sol–gel derived photonic structures formed by submicron silica spheres*

M. JASIORSKI¹, K. MARUSZEWSKI^{1, 3**}, W. STRĘK¹

¹Institute of Low Temperature and Structure Research, Polish Academy of Sciences, 50-950 Wrocław, Poland

²Mechanical Faculty, Institute of Materials Science and Applied Mechanics,
Wrocław University of Technology, Wrocław, Poland

Sol–gel synthesis of powders consisting of regularly shaped submicron silica spheres (\varnothing 400–600 nm) is described. IR and absorption spectra of such powders have been obtained. The IR spectra demonstrate that the silica spheres heated at 800 °C are hydroxyl-free. The TEM measurements show that the dimensions of silica nanoparticles do not change during heating. Films of self-organized silica nanospheres deposited on a glass support exhibit the photonic crystal effect.

Key words: silica submicron spheres, photonic effect, sol–gel method

1. Introduction

In the last decade synthesis and optical properties of photonic crystalline structures have been intensely investigated. Photonic crystals are characterized by frequency-forbidden band-gaps in a broad frequency region [1–4] of electromagnetic radiation. The characteristic feature of such materials is their opalescence. It has been demonstrated [5–9] that photonic crystals offer a number of potential applications such as filters, inhibitors of spontaneous emission or thresholdless lasers. Three-dimensional photonic crystals are typically formed by spatially arranged structures of closely packed submicron spheres. The most popular photonic structure is represented by opal formed by silica microspheres. Other examples of such photonic materials are microstructures built from polystyrene or latex microspheres. In this work, we report a sol–gel synthetic yielding regularly shaped silica microspheres which suspensions are capable of forming thin films exhibiting the photonic crystal effect. Preliminary spectroscopic investigations of the material obtained have also been performed.

*The paper presented at the International Conference on Sol-Gel Materials, SGM 2001, Rokosowo, Poland.

** Corresponding author, e-mail: marusz@int.pan.wroc.pl.

2. Experimental

The uniform silica particles were synthesized following the base-catalyzed polycondensation of silicic acid groups using tetraethoxysilane in alcoholic medium [10]. This procedure leads to formation of giant silica macromolecules. A mixture of 42 cm³ of ethanol (99.6%) and 7.5 cm³ of aqueous ammonia solution (NH₃, 25%, POCh, Gliwice) was mixed with 3.1 cm³ of tetraethoxysilane (TEOS, 99%, Fluka). The solution was stirred in a plastic flask with a magnetic stirrer at room temperature for 1.5–2 h. We have also varied the synthetic conditions by adding different volumes of aqueous ammonium: 1.9 cm³ (a), 3.75 cm³ (b), 7.5 cm³ (c), 11.2 cm³ (d), 15 cm³ (e). Then the material was left for solvent to evaporate. Powders were dried at 80 °C for three days. Such materials were then sintered at higher temperatures (200 °C for 16 h, 600 °C for 16 h and 800 °C for 16 h).

Photonic crystal structures were obtained by redispersing silica spheres in dimethylformamide (DMF) and leaving them to naturally sediment on glass plates. The structures obtained exhibit opalescence characteristic to photonic crystals.

The silica spheres prepared were characterized by transmission (TEM) and scanning (SEM) electron microscopies. TEM studies were carried out on a Philips CM20 microscope operating at 200 kV and providing a 0.24 nm point-to-point resolution. SEM measurements were performed on a scanning electron microscope Joel JSM 5800LV. The absorption spectra were measured on a Ocean Optics 2000 spectrophotometer. The IR measurements were carried out at room temperature. Spectra were obtained with a Bruker IFS-88 FT spectrometer in the region of 4000–400 cm⁻¹ with the resolution of 2 cm⁻¹. Polycrystalline powders were obtained by grinding in an agate mortar. Their suspensions in Nujol were placed between KBr wafers and the IR spectra were measured.

3. Results and discussion

TEM pictures of the products obtained with different amounts of aqueous ammonia (the catalyst) are shown in Fig. 1. The first picture (Fig. 1a) shows formless sol–gel silica glassy material obtained with 1.9 cm³ of aqueous ammonia. Fig. 1b demonstrates silica powder consisting mostly of formless material with some single spherical particles. This sample was obtained with 3.75 cm³ of aqueous ammonia. Further increase of the amount of aqueous ammonia results in the internal structure of the obtained powders becoming more regular and the particles gaining spherical shape. Fig. 1c shows the regular silica spheres (diameter ca. 415 nm) prepared using 11.2 cm³ of aqueous ammonia. Similar materials have been obtained with 7.5 cm³ (the spheres of diameter ≈ 600 nm) and 15 cm³ (the spheres diameter ≈ 500 nm) of aqueous ammonia. It has been observed that the shape and size of the silica nanoparticles did not change with temperature. The TEM micrographs of the sample obtained with

11.2 cm³ of ammonia solution (see Fig. 1c) heated at 200 °C, 600 °C and 800 °C are virtually identical.

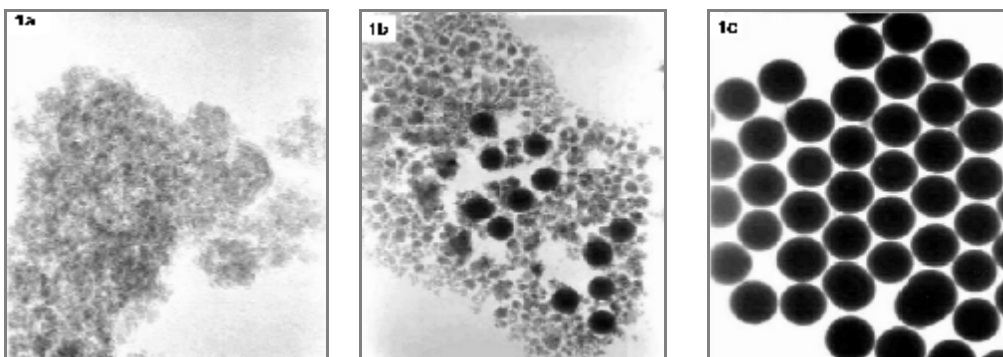


Fig. 1. TEM micrographs of the sol-gel powders obtained with different amounts of aqueous ammonia: a) 1.9 cm³, b) 3.75 cm³, d) 11.2 cm³

Figure 2 presents the IR spectra of the silica spheres measured at the successive stages of the thermal treatment. As it can be seen, increase in temperature results in intensity decrease of the band at approximately 3400 cm⁻¹ which indicates the diminishing in the hydroxyl groups content in the silica powder.

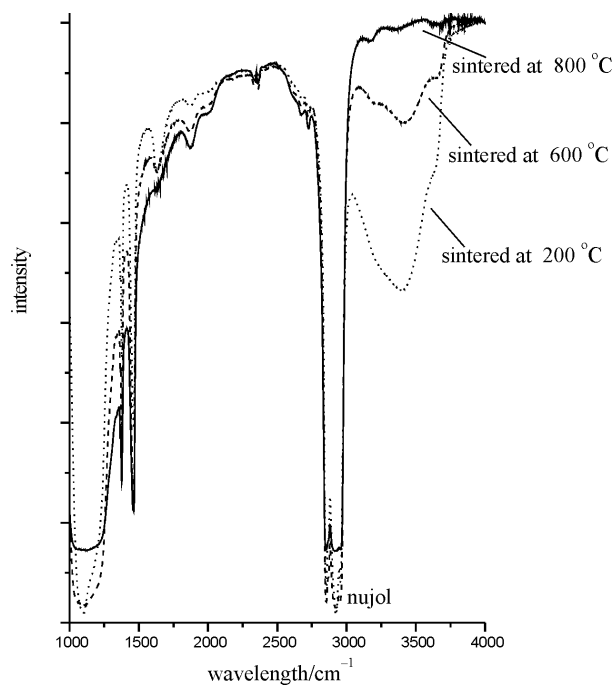


Fig. 2. IR spectra of the silica spheres sintered at different temperatures

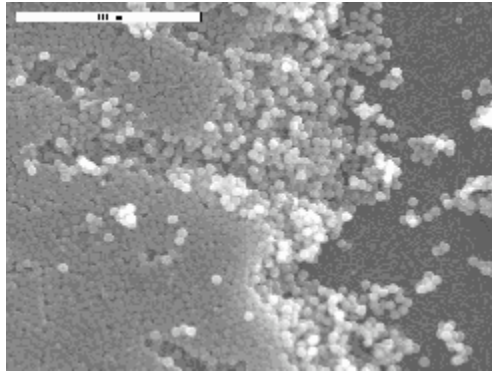


Fig. 3. SEM micrograph of a silica spheres on a glass support

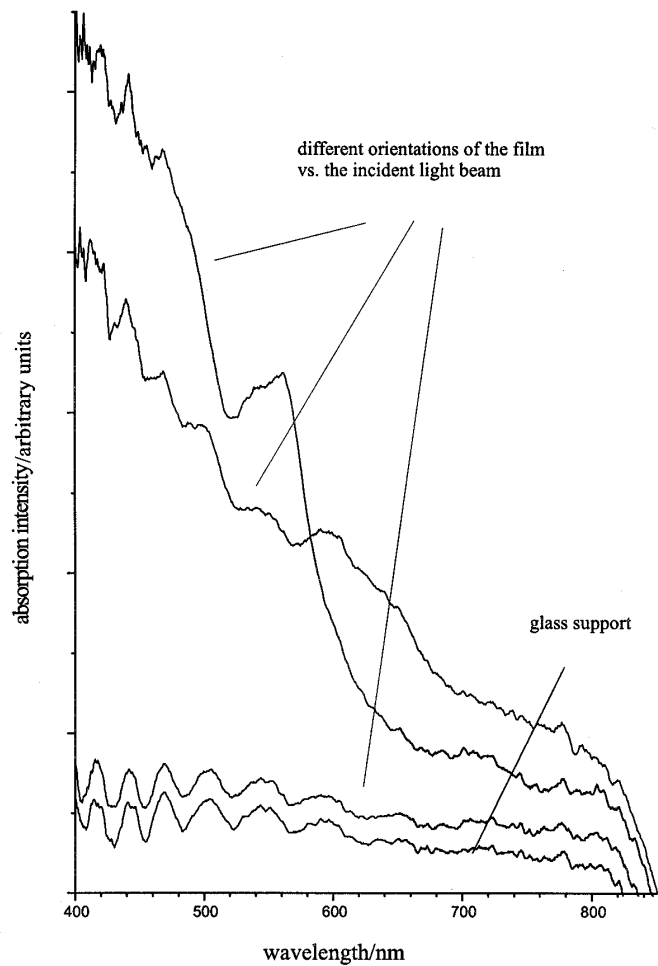


Fig. 4. Absorption spectra of a thin film of silica spheres on a glass support obtained at different angles between the film and the incident light beam

The silica nanospheres were placed on glass supports in the form of thin films. Figure 3 presents a SEM micrograph of such a film. The self-assembled films of silica spheres demonstrate strong opalescence. The absorption spectra of such films obtained at different orientations of the glass support versus the incident light wavelength are shown in Fig. 4. A shift of the absorption edge with the changes of the angle of the incident light can be seen. Since a thin film consisting of the uniform silica spheres has formed on the support in a random manner, changes of the film position in the light path result in random changes of the absorption edge (the sample's apparent colour). The same effect is responsible for random opalescence of natural opals. This effect demonstrates the photonic crystal character of the investigated materials.

4. Conclusions

The sol-gel-based method of preparation of submicron spherical silica particles is reported. The nanospheres morphology has been studied by the TEM method. It has been found that all silica particles possess uniform spherical shape and virtually identical size (ca. 400 nm). It has been observed that with increasing temperature of sintering water contamination was significantly reduced while the particles size remained unchanged. Photonic crystal behaviour of the films formed by silica spheres placed on planar glass supports has been observed.

Acknowledgements

The authors thank dr. K. Heiman (Technical University of Wrocław) for the SEM micrographs. This work was supported by the grant from the Polish Committee for Scientific Research (Grant No. KBN 3 T09B 027 18).

References

- [1] YABLONOVICH E., *Phys. Rev.*, 1987, 58, 2059.
- [2] *Photonic Band Gap Materials*, *Opt. Soc. Am. B*, 1993, 10, 2.
- [3] BRINKER C.J., SCHERER G. W., *Sol-gel Science*, 1990, New York, Academic Press Inc.
- [4] STOBER W., FINK A., BOHN E., *J. Colloid Interface Sci.*, 1968, 26, 62.
- [5] SALVAREZZA R.C., VAZQUEZ L., MIQUEZ H., MAYORAL R., LOPEZ C., MESEGUER F., *Phys. Rev. Lett.*, 1996, 77, 4572.
- [6] LOPEZ C., VAZQUEZ L., MESEGUER F., MAYORAL R., OCANA M., MIGUEZ H., *Superlattices Microstructures*, 1997, 22, 399.
- [7] REYNOLDS A., LOPEZ-TEJEIRA F., CASSAGNE D., GARCIA-VIDAL F.J., JOUANIN C., SANCHEZ-DEHESA J., *Phys. Rev. B*, 60 1999, 11422.
- [8] BOGOMOLOV V.N., KURDYUKOV D.A., PROKOFEV A.V., SAMOILOVICH C.M., *Pisma Zh. Eksp. Teor. Fiz.* (in Russian), 1996, 63, 496.

- [9] BOGOMOLOV N.V., GAPONENKO S.V., GERMANENKO I.N., KAPITONOV A.M., PETROV E.P., GAPONENKO N.V., PROKOFEV A.V., PONYAVINA A., SILVANOVICH N.I., SAMOILOVICH S.M., *Phys. Rev. E*, 1997, 55, 7619.
- [10] ROGACH E., KORNOWSKI A., GAPONENKO N.V., KAPITONOV A.M., GAPONENKO S.V., ROGACH A.L., EYCHMULLER A., [in:] V.E. Borisenko, A.B. Filonov, S.V. Gaponenko, V.S. Gurin Physics (Eds.), *Chemistry and Application of Nanonstructures*, 1999, Singapore, World Scientific, p. 111.

LUMINESCENT MATERIALS, RECOGNITION PHASES OF THE CHEMICAL SENSORS AND HETEROGENEOUS CATALYSTS PREPARED BY SOL-GEL METHOD

Andrzej M. Klonkowski

Faculty of Chemistry, University of Gdańsk, 80-952 Gdańsk, Poland

Abstract

The sol-gel process enables one to prepare oxide xerogels at room temperature. By using this method, it is possible to encapsulate a wide variety of organic, complex (organometallic) molecules and metallic nanoparticles stabilized by organic ligands in the inorganic or inorganic/organic hybrid matrix. Studies of this new type of inorganic/organic composite have evolved towards the deliberate doping of the supramolecular species. This review gives three examples of how doped xerogel materials prepared by the sol-gel method are emerging as an important means of producing new materials. The first part of this review is devoted to luminescent materials which are based on the antenna effect and are composed of Eu(III) complex (luminescence centre) entrapped in xerogel matrix. In this case results of the experiments concerning the coordination sphere composition show that a cryptand ligand with aromatic groups and an aromatic co-ligand, settle efficient action the antenna effect and isolate the central ion from each efficient quenchers, as *e.g.* water molecules. Secondly, silica xerogel samples with entrapped series of three fluorescent chemosensors of the *Ant-R-Ant* type, where *Ant* is an anthryl group and *R* is a receptor (spacer) with donor atoms, were prepared as chemical recognition phases. The recognition phase with fluorosensor of the type *Ant-N-O-O-N-Ant*, where N and O are donor atoms, can be regenerated many times and seems to be most promising system for the fluorescent chemical sensor. In the third part of this paper, ligand protected metal nanoclusters as immobilized catalysts are the point of interest. This type of heterogeneous catalysts are much less investigated than the bare metal particles on supports. The main interest is focused on the function of the ligands.

Keywords: sol-gel, xerogel, ligand, organometallic

1. Introduction

The synthesis of materials by the sol-gel process generally involves the use of metal alkoxides or organical derivatives of these alkoxides which undergo hydrolysis and condensation polymerisation reactions to give alcogel and then xerogel after drying. The synthesis of oxides and organically modified oxides by this approach has been a subject of several books and reviews [1–4].

The method has received considerable attention because it possesses a number of desirable characteristics. It enables one to prepare glasses at far lower temperatures than is possible by using conventional melting. Compositions which are difficult to obtain by conventional means because of volatilisation, high melting temperatures or crystallization problems can be produced. In addition, the sol-gel method is a high-purity process which leads to excellent homogeneity. Finally, the sol-gel approach is adaptable to producing bulk pieces as well as films and fibres.

During the past ten years it has been widely recognized that the sol-gel process may be used to encapsulate organic and organometallic molecules as well as metallic nanoclusters in an inorganic or inorganic/organic hybrid medium. It is now evident that the synthesis of this types of xerogels is not limited to just a few substances. The flexible solution chemistry and the ability to prepare a matrix with little or no heating means that the sol-gel approach is compatible especially with a wide variety of organic molecules. In general, the list of dopants in this case is constantly expanding [5].

Prior to the sol-gel work, the incorporation of organic, organometallic and metallic species in solids generally was restricted to the use of frozen solvents or organic polymer matrices. The present approach represents a totally new type of inorganic/organic composite material because the oxide skeleton not only offers a significantly more ionic environment but also is thermally, chemically and dimensionally more stable. Thus, studies of organic, organometallic or metallic doped xerogels have began to develop substantial breadth; from investigations of doped xerogels for luminescent materials, to the development of recognition phases of optical chemical sensors and heterogeneous catalysts.

2. Luminescent materials

Materials containing lanthanide ions have been used as phosphors and laser materials because of their sharp, intensely luminescent *f-f* electronic transitions. In particular, a number of lanthanide complexes showed a bright and narrow lanthanide ion emission. These emissions usually resulted from the so called "antenna effect", which is defined as a light conversion process *via* an absorption-energy transfer-emission sequence involving distinct absorbing by a ligand (light collector) and emitting by a metal ion. In such a process, the quantities that

contribute to the luminescence intensity are: (i) the intensity of the ligand absorption, (ii) the efficiency of the ligand-to-metal energy transfer, and (iii) the efficiency of the metal luminescence (see Fig. 1).

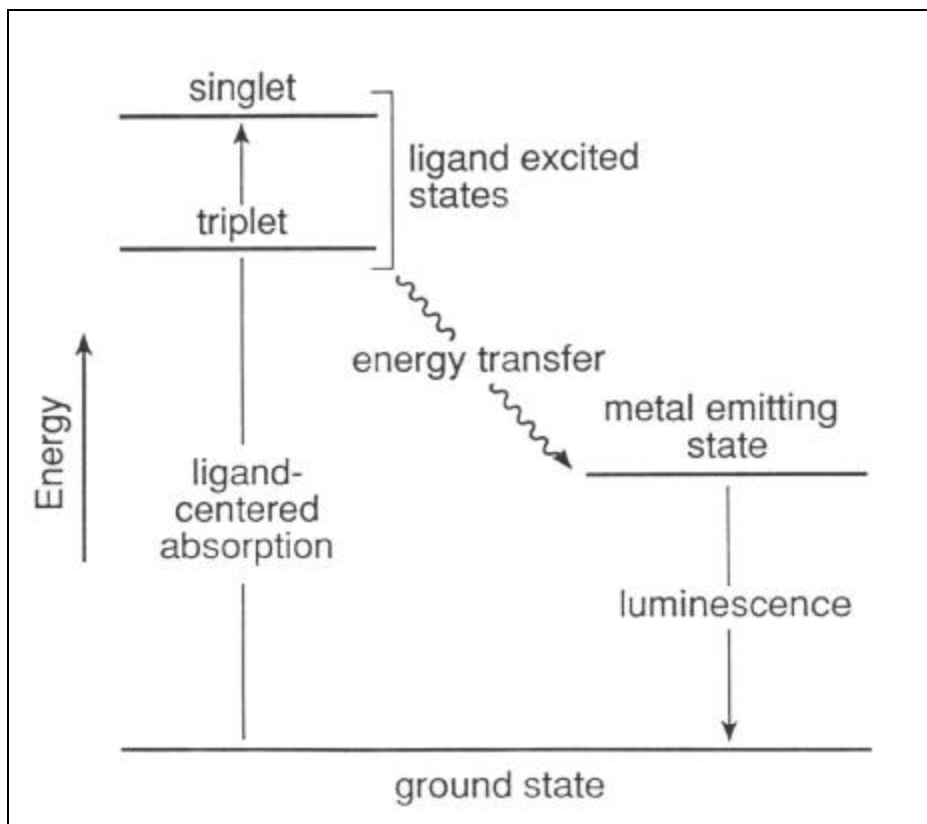


Fig. 1. Schematic representation of the antenna effect involving absorbing ligand and emitting metal subunits [6].

This phenomenon has been reviewed by Sabbatini et al. [6]. The luminescence properties of lanthanide complexes in a variety of solutions have extensively been investigated [7–11] which demonstrated that lanthanide complexes have superior fluorescence properties with respect to simple salts in solutions. However, conventional ligands are not able to give rise to inert complexes, especially in aqueous solution where solvent molecules efficiently compete to occupy coordination sites. In fact, the cryptand ligands possess spheroidal cavities and donors atoms, like oxygen and nitrogen. This type of ligands makes high stable complexes with lanthanide ions and is able to shield the encapsulated ion from interaction with surrounding.

In order to increase the intensity of the lanthanide luminescence exploiting the antenna effect, complexes with strongly absorbing cryptands have been designed, e.g. cryptands with aromatic segments, e.g. 2,2'-bipyridine (bpy), 1,10-phenanthroline (phen) or 3,3'-biisoquinoline (biq), which show intense absorption bands in the UV region due to $\pi-\pi^*$ transitions.

In attempt to improve the luminescence properties of Eu(III) cryptates, the bpy or biq units of cryptands were replaced with bpyO₂ or biqO₂ [12]. Results on the luminescence of Eu(III) complexes with the dioxide derivatives have shown that the included central metal ion is better protected from interactions with water than in the case of the [Eu bpy derivative]³⁺ or [Eu biq derivative]³⁺ cryptate and that these complexes present a significant gain in light-conversion efficiency over earlier europium cryptates.

The sol-gel process is a potentially attractive means of synthesizing novel luminescent materials. The incorporation of lanthanide complexes, particularly europium(III) complexes has been investigated in details [13–20]. Xerogels doped with Eu(III) complexes have shown substantially improved luminescence characteristics with respect to comparable materials containing simple metal.

According to the theory of non-radiative transitions in lanthanide complexes [21–23], the non-radiative relaxation between various J states may occur by interaction of the electronic levels of the lanthanide ion with suitable vibrational modes of the environment. The efficiency of these processes depends on the energy gap between the ground and excited states and the vibrational energy of the oscillators [21, 22, 24]. When solvents containing O–H groups are coordinated to lanthanide ions, efficient non-radiative deactivations take place via

vibronic coupling with the vibrational states of the O–H oscillators [25–27]. If the O–H oscillators are replaced by the low frequency O–D oscillators, the vibronic deactivation pathway becomes much less efficient.

In order to reduce the non-radiative decay from the excited state of Eu(III) we tried to eliminate O–H oscillators in the short range, i.e. in the coordination environment of the central ion and in the long range, i.e. in the xerogel matrix. To realize the short-range approach we have tested several ligands for Eu(III) ion luminescence characteristics [19]. Among the ligands used, the best results (*i.e.* the higher emission intensity and longer lifetime) shows the [*biqO*₂.2.2] cryptand, where *biqO*₂ is 3,3'-biisoquinoline-2,2'-dioxide (Fig. 2A, structure 1).

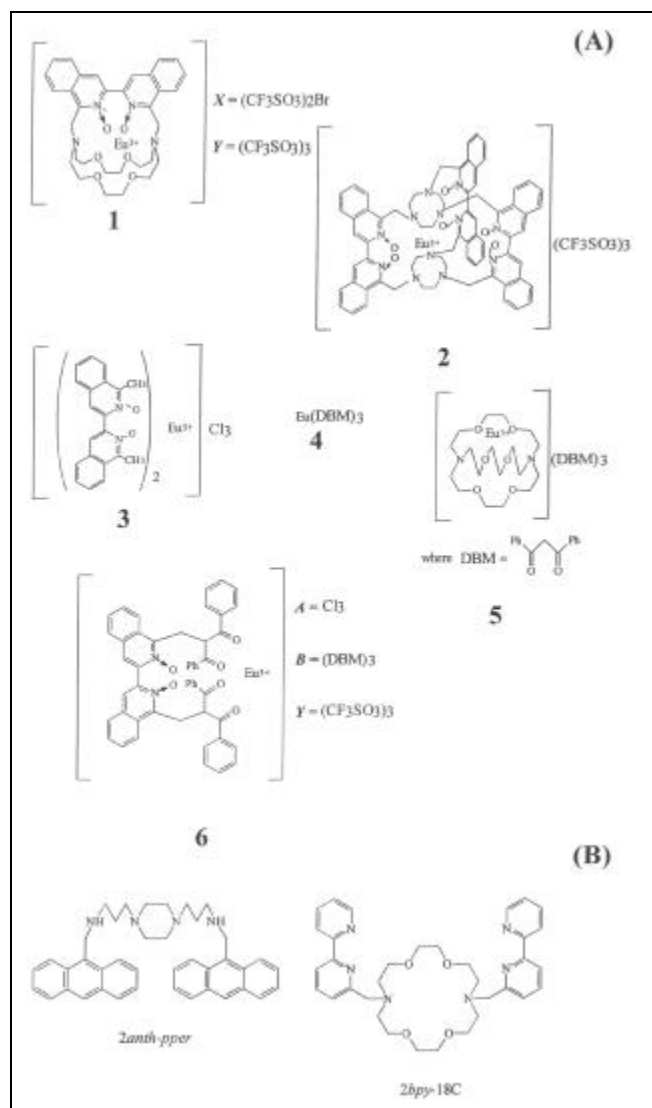


Fig. 2. Molecular structures of the studied: (A) Eu(III) complexes (cryptates) and (B) some co-ligands.

Luminescence intensity can be increased if the coordination sphere is completed additionally with co-ligands such as 1,10-phenanthroline (*phen*), 2,2'-bipyridine (*bpy*), triphenylphosphine oxide (*TPPO*) [19, 20] or other aromatic systems replacing water molecules from the first coordination sphere of Eu(III) (in Fig. 2B). To eliminate the O–H quenchers in the long range of Eu(III) surrounding we used D₂O instead of H₂O as a reagent and deuterated methanol (MeOD) instead of MeOH as a solvent in the sol-gel procedure – cf. in Tab. 1 [19].

Tab. 1. Preparation procedure and its influence on the relative luminescence intensity I_{rel} in the band maximum and luminescence lifetime t of the cryptate 1 immobilized in $[\text{SiO}_{4/2} + \text{Si}(\text{CH}_3)_2\text{O}_{2/2}]$ xerogel.

Reagents	Solvent	Catalyst	Relative intensity (I_{rel}) ^a	Lifetime $t / \mu\text{s}$ ^b
$\text{Si}(\text{OCH}_3)_4 + \text{H}_2\text{O}$	CH_3OH	Acetic acid	0.36	574
$\text{Si}(\text{OCH}_3)_4 + \text{D}_2\text{O}$	CH_3OH	Acetic acid	0.40	587
$\text{Si}(\text{OCH}_3)_4 + \text{D}_2\text{O}$	CH_3OD	Acetic acid	1.0	608

^a $\lambda_{exc} = 352 \text{ nm}$, $\lambda_{em} = 622.6 \text{ nm}$

^b $\lambda_{exc} = 394 \text{ nm}$, $\lambda_{em} = 615.0 \text{ nm}$

Good results can be also obtained if the Eu(III) cryptate is encapsulated in methyl-modified silicate xerogel dried by means of $(\text{Me}_3\text{Si})_2\text{NH}$ agent and additionally at elevated temperature (Fig. 3) [20].

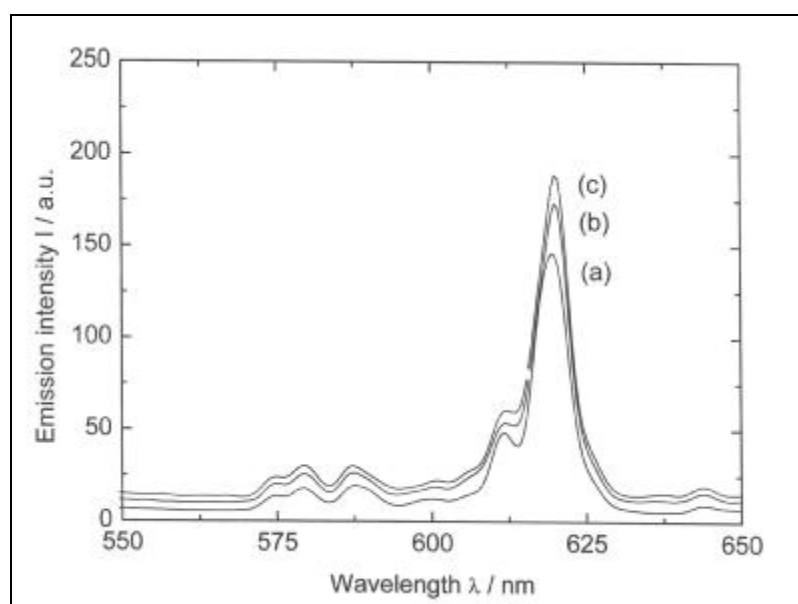


Fig. 3. Emission spectra of material prepared by entrapment of cryptate salt 1X in methyl modified silicate matrix: (a) dried at room temperature, (b) after reaction with $(\text{Me}_3\text{Si})_2\text{NH}$ reagent and (c) after the reaction as previously and drying at 80°C . $\lambda_{exc} = 3$ [27]

To improve luminescence properties, i.e. to enhance the emission intensity and lengthen the lifetime of the Eu(III) excited state in the materials, we recently analyse influence of ligands, coligands, anions and matrix materials on the Eu(III) luminescence characteristics in its complexes (cryptates). Such components of the matrix materials as oxide mixtures (titania-silica and zirconia-silica), polydimethylsiloxane (PDMS) as well as 3-glycidoxypropyl-modified oxide strongly influence on the luminescence activity. In general, Eu(III) ion should be isolated particularly from effectively quenching O–H groups. On the other hand, O–H oscillators can be eliminated from the materials by a chemical agent and/or by drying in elevated temperature. Finally, the prepared materials with the Eu(III) cryptate were tested after exposure to UV radiation during a time period. Namely, there is problem related to photodegradation of the organic antenna system in a luminescent material during excitation by high-energy quanta [28].

It is now evident that in such multiply systems as the luminescent materials with Eu(III) complexes prepared by the sol-gel procedure, efficiency of their luminescence depends first of all on presence of quenching O–H oscillators not only in the shortest distance from the central ion (first coordination sphere), but also in the long distance, i.e. in matrix.

3. Recognition phases of the fluorescent chemical sensor

Luminescence is perhaps the most convenient and an easily detectable property which can be used to signal the occurrence of molecular events in real time and in real space. Owing to fluorescence, it can be unambiguously detected even at very low concentrations and can be switched on and off (enhanced/quenched) through well-defined mechanisms, namely electron transfer or energy transfer [29].

Luminescent molecular receptors capable of sensing a variety of analytes (H^+ [30], *s*- and *d*-block metal ions [31, 32], anions [33] and amino acids [34]) have been developed. Most of them have been designed by following a two-component approach, *i.e.* by covalently linking a receptor subunit displaying selective affinity towards the envisaged substrate to luminescent fragment (*fluorophore*) [35]. The sensing compounds incorporating a binding site, a fluorophore, and a mechanism for communication between the two are called *fluorescent chemosensors (fluorosensors)* [30, 36–40].

Recently, many investigations have been done on chelation-enhanced fluorescence [41] to make fluorosensors. In all these systems [35, 42], complexation by non-transition-metal ions or protonation of the amino groups present enhances the fluorescence quantum yield, as fluorescence quenching due to *photoinduced electron transfer (PET)* in the receptor molecule will no longer be operative. Transition-metal-based molecular fluorescent signalling systems are eagerly awaited [30, 39, 40, 43]. These systems would be useful not only at real-time and real-space monitoring devices in biology but also as versatile molecular switching devices. Transition metal ions are known as effective fluorescence quenchers [44–46]. We present here the very rare systems [41] where transition metal ions Cu(II) and Ni(II), along with Co(II) and Zn(II) ions, cause enhancement of fluorescence. The signalling possibilities arise from the fact that the fluorophore-spacer-receptor system in the cation-free situation has been chosen such that its fluorescence is switched off by the PET process, as in Fig. 4 [47, 48].

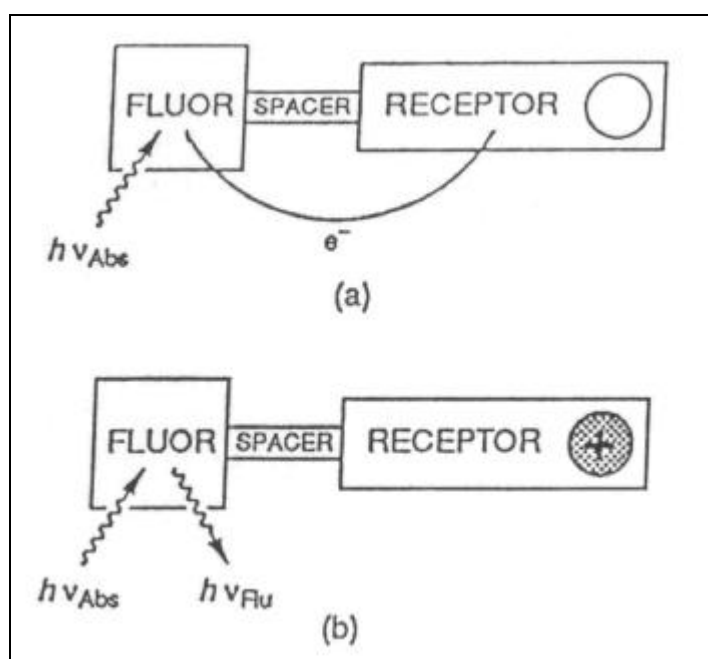


Fig. 4. Schematic representation of photoinduced processes in a 'fluor-spacer-receptor' signalling system (a) when cation-free and (b) when cation-bound.

The PET process, in turn, can be suppressed by the entry of a cation into receptor by the cation-induced increase of the ionisation/oxidation potential of the receptor. At the simplest level this is an electric field effect. However, other ways of inhibiting electron transfer are available such as these three approaches: conformational changes, local polarity modulations, and hydrogen bonding. Such a suppression of the PET process means that fluorescence becomes the dominant decay channel of the excited fluorophore [30]. Thus, cation entry is signalling by photon output when interrogated by excitation photons.

The fluorophore and the receptor units can be connected covalently or non-covalently. In the simplest covalently linked fluorophore-receptor systems, a $-(CH_2)_n-$ bridge may suffice to keep the two subunits together. However, the features of the spacer are not irrelevant, as they affect the signal transduction mechanism and, ultimately, determine signalling efficiency (Fig. 5).

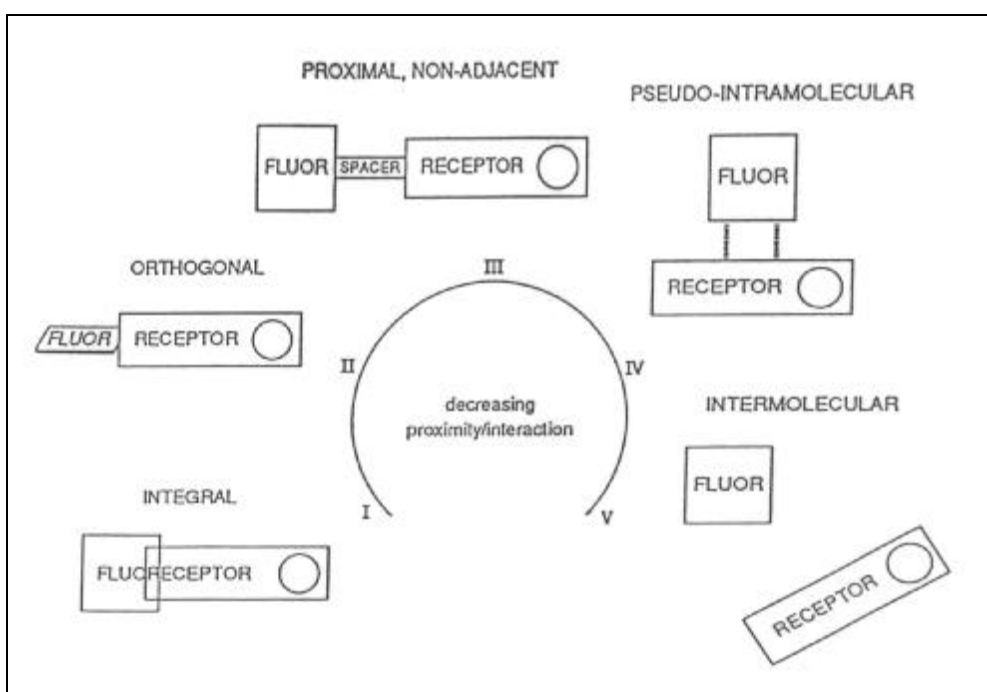


Fig. 5. Molecular structure schemes of the type 'fluor-receptor' used in fluorescent chemosensors [29].

Glass is traditionally the favourite support for optical sensors [49–51]. The special characteristics of glass, which include transparency, chemical inertness and inexpensive manufacturing procedures combine with ability to the geometric configurations and the physical characteristics of glass, make it a most suitable support for diagnostic photometry. However, due to simpler immobilisation procedures, most sensor devices utilise polymeric supports for chemical recognition phases despite their inferior optical characteristics [52, 53].

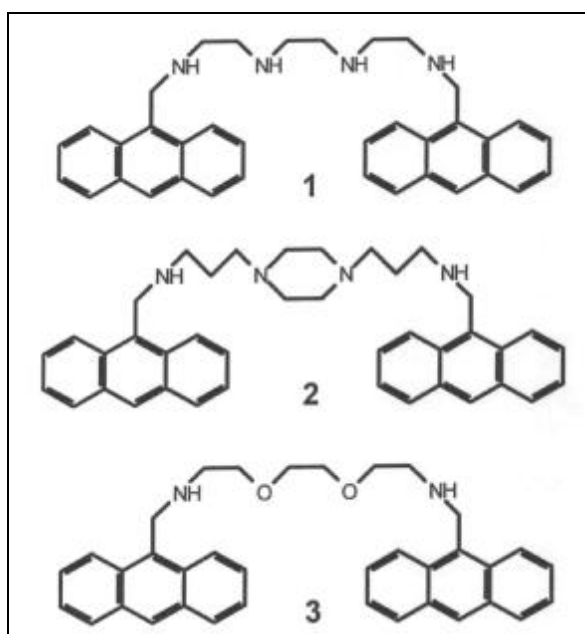


Fig. 6. Molecular structures of the studied bis-9-anthryl derivatives of the type Ant-R-Ant, where R is a quadridentate receptor spacer [63].

About ten years ago, a novel immobilising method was introduced using the sol-gel polymerisation process [5, 54, 55]. Here, the dopants are incorporated in the dry gel (xerogel) at the early stages (or even before

initiation) of the hydrolysis and polycondensation processes. Thus, when the xerogel is formed the dopants remain physically encapsulated within the microporous gel matrix but maintain their ability to interact with diffusing species [56–58]. Such materials have been used in a range of recognition phase configurations. These includes monoliths and deposited films, end-coated and side-coated optical fibres and planar waveguides, and some novel configurations such as packed capillary tubes [59]. Some years ago Wolfbeis, Reisfeld and Oehme [60] have reviewed the principles of optical sensors based on the use of the sol-gel technique, in particular their fabrication, working principles, and various configurations.

In our paper [61–64] are discussed experiments with chemical recognition phases consist of the prepared fluorosensors (*bis-9-anthryl* quadridentate derivatives, Fig. 6) immobilised in porous silica xerogel by the sol-gel procedure.

The results show that the supramolecular system **1** of the type *Ant-N-O-O-N-Ant*, where N and O are donor atoms in the receptor (spacer or ligating) group, is the most useful as fluorosensor. This chemosensor is more sensitive for Cu(II) than for other transition metal ions such as *e.g.* Co(II), Ni(II) and Zn(II) ions (Fig. 7).

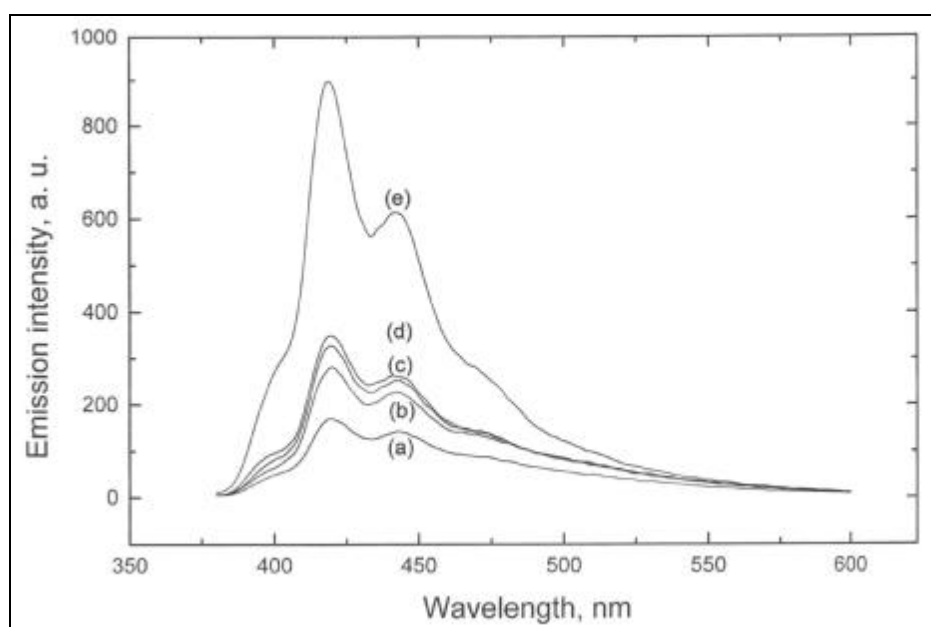


Fig. 7. Fluorescence emission spectra of the NOON fluorosensor: (a) uncomplexed and complexed with: (b) Co(II), (c) Ni(II), (d) Zn(II), and (e) Cu(II) ions [63].

Our experiments show that the sol-gel process is a versatile fabrication method to prepare chemical recognition phases of fluorescent chemical sensor. The recognition phases consist of silica as a matrix and *bis-9-anthryl* derivatives as fluorescent chemosensors for transition metal ions in aqueous solution.

Among the fluorosensors the molecular system **1**, *i.e.* *Ant-N-O-O-N-Ant*, (see Fig.) is the most promising as a component of the recognition phase in the fluorescent chemical sensor for Cu(II) ions.

4. Heterogeneous catalysts

The use of ligands stabilized transition metal clusters on the one hand and of unprotected, bare nanoparticles on the other hand as homogeneous and heterogeneous catalysts, respectively, is extensively described in the literature [65]. In particular, supported metal particles are traditionally applied in industrial catalysis for many purposes. The catalytic behaviour of bare particles on supports has been studied as a function of size and shape in a huge number of papers in the course of the last decades, whereas ligand protected clusters are much less investigated as immobilized catalysts. The main interest was focused on the function of the ligands. Indeed, they can increase or reduce activity, however, it has also been shown that the influence of ligands with respect to selectivity may also be of some interest. Schmid et al. [66, 67] have been able to show that ligand stabilized Pd clusters in the size range of 3–4 nm show very good activity and selectivity on various supports when they are used for the semihydrogenation of hex-2-yne to *cis*-hex-2-ene. The ligands consisted of variously substituted phenantrolines. It could be observed that, depending on the kind of substituent, *e.g.* alkyl groups of various lengths, the activities changed considerably, whereas the selectivity was in any case close to 100%.

On the other hand, in the case of very small Pd nanoparticles (1.5 nm) in a supported form with and without ligands to semihydrogenate hex-2-yne, is observed that for the phenantroline protected clusters the

selectivity is only ca. 80–90%, whereas for the bare clusters it is 100 %. From experience of Schmid et al. [68] this result could not be expected. Whatever the reason for that behaviour may be, it becomes clear that catalytic studies with clusters of definite size and environment are valuable materials to work out principles.

An important progress consists of the preparation of water soluble nanoclusters using hydrophilic P- and N-donors as stabilizers [69–71]. Further miscellaneous agents have been used for this purpose [69, 72–83]. Colloidal metal systems stabilized either by surfactants or by solvents are very monodisperse and have been applied successfully as precursors to heterogeneous catalysts [84–87]. Electron microscopy has confirmed that the discrete metal particles may be deposited onto supports without and unwanted agglomeration. This is a major prerequisite for size selective studies in heterogeneous catalysis.

In our experiments we used with success amino- and thiol-trialkoxysilane derivatives as stabilizers of metal nanoparticles, such as Pd, Pt i Rh, in sol. In the next stage owing to the sol-gel process are prepared very monodisperse metal clusters supported on the organically modified xerogels. These pre-prepared nanometals stabilized by ligand amino or thiol groups may be used as easily accessible precursors for a new type of heterogeneous catalysts. These precursors may be optimized independent of the support by varying the particle size, composition, and structure of metallic system. Further, the coverage of the metal surface by various protective shells and intermediate layers, for example, oxygen or sulfur, may be used for modifications of the active component. This is visualized in Fig. 8.

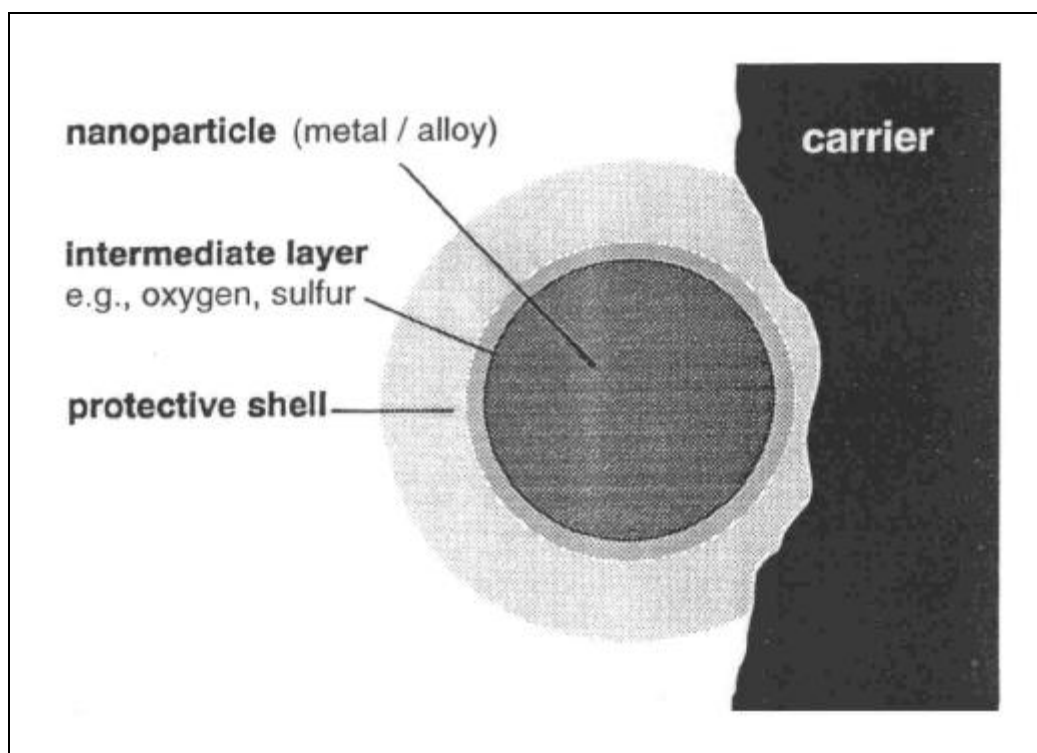


Fig. 8. The catalyst precursor concept [88].

The perfect protection of the nanometallic hydrosols by various alkoxide-derivatives allows the handling of the precursors even in concentrated alcoholic solution. Further, the use of amino- or thiol modified alkoxides as the protective shell around the metal core enables the efficient fixation the metal particles by covalent bonds on an oxide support. The supported metal particles are very resistant to agglomeration even under extreme conditions [88].

Acknowledgement

The presented studies were supported by the Polish Scientific Research Council (Grants 7 T09A 106 20, 3 T09A 136 17 and DS-UG/8280-4-0091-0).

References

1. L.L. Hench and J.K. West, Chem. Rev. 90 (1990), 33.
2. C.J. Brinker, G. Scherer, Sol-Gel Science: The Physics and Chemistry of Sol-Gel Processing. Academic Press, San Diego 1989.

3. Sol-Gel Technology. L.C. Klein (Ed.), Noyes Publications, Park Ridge NJ 1988.
4. L.C. Klein, *Annu. Rev. Mater. Sci.* 15 (1985), 227.
5. B. Dunn, J.I. Zink, *J. Chem. Mater.* 1 (1991), 903.
6. N. Sabbatini, M. Guardigli, *Coord. Chem. Rev.* 123 (1993), 201.
7. G.A. Crosby, R.E. Whan, R.M. Alire, *J. Chem. Phys.* 34 (1961), 741.
8. L.R. Melby, N.J. Rose, E. Abramson, J.C. Caris, *J. Am. Chem. Soc.* 86 (1964), 5117.
9. J.L. Kropp, M.W. Windsor, *J. Chem. Phys.* 42 (1965), 1590.
10. W.R. Dawson, J.L. Kropp, M.W. Windsor, *J. Chem. Phys.* 45 (1966), 2410.
11. J. Kleinerman, *J. Chem. Phys.* 42 (1969), 1590.
12. J.-M. Lehn, C.O. Roth, *Helv. Chim. Acta* 74 (1991), 572.
13. D. Levy, R. Reisfeld, D. Avnir, *Chem. Phys. Lett.* 109 (1984), 596.
14. X.P. Fan, W.Q. Wang, G.H. Xiong, *Mater. Sci.* B21 (1993), 55.
15. M.J. Lockhead, K.L. Bray, *J. Non-Cryst. Solids* 170 (1994), 143.
16. X.P. Fan, W.Q. Wang, G.H. Xiong, *Mater. Lett.* 27 (1996), 177.
17. X.P. Fan, M.Q. Wang, Z.Y. Wang, Z.G. Hong, *Mater. Res. Bull.* 32 (1997), 1119.
18. K. Czarnobaj, M. Elbanowski, Z. Hnatejko, A.M. Klonkowski, S. Lis, M. Pietraszkiewicz, *Spectrochim. Acta A*, 54 (1998), 2183.
19. A.M. Klonkowski, S. Lis, Z. Hnatejko, K. Czarnobaj, M. Pietraszkiewicz, M. Elbanowski, *J. Alloys Compd.*, 300–301 (2000), 55.
20. Z. Hnatejko, A.M. Klonkowski, S. Lis, K. Czarnobaj, M. Pietraszkiewicz, M. Elbanowski, *Mol. Cryst. Liq. Cryst. A*, 354 (2000) 207.
21. W.T. Carnal, in: *Handbook on the Physics and Chemistry of Rare Earths*. K.A. Gschneider, L. Eyring, (Eds.), vol. 3, North-Holland, Amsterdam 1979, p. 237.
22. R. Reisfeld, *Struct. Bonding*, Springer Verlag, Berlin 1975, 22, 123.
23. W. Stręk, *J. Chem. Phys.*, 76 (1982), 5856.
24. F.K. Freed, *Top. Appl. Phys.*, 15 (1976), 23; G. Stein, E. Wurzburg, *J. Chem. Phys.* 62 (1975), 208.
25. Y. Haas, G. Stein, *J. Phys. Chem.*, 75 (1971), 3677.
26. B. Yan, H. Zhang, S. Wang, J. Ni, *J. Photochem. Photobiol. A. Chem.*, 112 (1998), 231.
27. A.M. Klonkowski, S. Lis, M. Pietraszkiewicz, Z. Hnatejko, K. Czarnobaj, M. Elbanowski, *Chem. Mat.*, in press.
28. V. Balzani, F. Scandola, *Supramolecular Photochemistry*. Ellis Harwood, London 1991, p. 73.
29. R.A. Bissell, A.P. de Silva, H.Q.N. Gunaratne, P.L. M. Lynch, G.E.M. Maguire, K.R.A.S. Sundanayake, *Chem. Soc. Rev.*, 1992, 187.
30. A.P. de Silva, H.Q.N. Gunaratne, T. Gunnlaugsson, A.J.M. Huxley, C.P. McCoy, J.T. Rademacher, T.E. Rice, *Chem. Rev.*, 97 (1997), 1515.
31. L. Fabbri, M. Licchelli, P. Pallavicini, A. Perotti, D. Sacchi, *Angew. Chem., Int. Ed. Engl.*, 33 (1994), 1975.
32. L. Fabbri, I. Faravelli, G. Francese, M. Licchelli, A. Taglietti, *Chem. Commun.*, 1998, 971.
33. L. Fabbri, G. Francese, M. Licchelli, A. Taglietti, *Chem. Commun.*, 1997, 581.
34. A.W. Czarnik, *Acc. Chem. Res.*, 27 (1994), 302.
35. *Fluorescent Chemosensors for Ion and Molecule Recognition*. A.W. Czarnik (Ed.), Amer. Chem. Soc., Washington DC 1993.
36. B. Valeur, in: *Topics in Fluorescence Spectroscopy*. J.R. Lakowicz (Ed.), Plenum Press, New York 1994, vol. IV, p. 21.
37. A.W. Czarnik, in: *Topics in Fluorescence Spectroscopy*. J.R. Lakowicz (Ed.), Plenum Press, New York 1994, vol. IV, p. 49.
38. J.-M. Lehn, *Angew. Chem., Int. Ed. Engl.*, 27 (1988), 89.
39. A.P. de Silva, H.Q.N. Guanaratne, C.P. McCoy, *Nature*, 364 (1993), 42.
40. P. Ghosh, P.K. Bharadwaj, S. Mandal, S. Ghosh, *J. Am. Chem. Soc.*, 118 (1996), 1553 and references therein.
41. Fernandez-Gutierrez, A. Munoz de la Pena, in: *Molecular Luminescence Spectroscopy: Methods and Applications*. S.G. Schulman (Ed.), Wiley, New York 1985, p. 371.
42. A.W. Czarnik, *Chem. Biol.*, 2 (1995), 423.
43. A.W. Varnes, R.B. Dodson, E.L. Wehry, *J. Am. Chem. Soc.*, 94 (1972), 946 and references therein.
44. K. Rurack, U. Resch, M. Senoner, S. Dachne, *J. Fluoresc.*, 3 (1993), 141.
45. J.A. Kemlo, T.M. Shepherd, *Chem. Phys. Lett.*, 47 (1977), 158.
46. R.S. Davidson, *Adv. Phys. Org. Chem.*, 19 (1983), 1; *Photoinduced Electron Transfer*. M.A. Fox (Ed.), Parts A-D, Elsevier, Amsterdam 1988.

-
47. A.J. Bryan, A.P. de Silva, S.A. de Silva, R.A.D.D. Rupasinghe, K.R.A.S. Sandanayake, *Biosensors*, 4 (1989), 169.
 48. *Chemical Sensors*, T. Edmont (Ed.), Blackie, Glasgow 1988.
 49. P. Roper, *Am. Ind. Hygiene Assoc. J.*, 35 (1974), 438.
 50. *Molecular Luminescence Spectroscopy: Methods and Applications*. S.G. Schulman (Ed.), Wiley, New York 1989.
 51. G. Serra, A. Schirone, R. Boniforti, *Anal. Chim. Acta*, 232 (1990), 337.
 52. T. Nakagama, M. Yamada, T. Hobo, *Anal. Chim. Acta*, 231 (1990), 7.
 53. R. Zusman, C. Rottman, M. Ottolenghi, D. Avnir, *J. Non-Cryst. Solids*, 122 (1990), 107.
 54. B. Dunn, J.I. Zink, *J. Chem. Mater.*, 1 (1991), 903.
 55. S. Braun, S. Rappoport, R. Zusman, D. Avnir, M. Ottolenghi, *Mater. Lett.*, 10 (1990), 1.
 56. D. Levy, B.I. Kuyavskaya, I. Zamir, M. Ottolenghi, D. Avnir, O. Lev, *J. Sep. Sci. Technol.*, 27 (1991), 589.
 57. J.C. Pouxviel, B. Dunn, J.I. Zink, *J. Phys. Chem.*, 93 (1989), 2134.
 58. A. Salma-Schwok, D. Avnir, M. Ottolenghi, *J. Am. Chem. Soc.*, 113 (1991), 3984.
 59. B.D. MacCraith, C.M. McDonagh, G. O'Keefe, A.K. McEvoy, T. Butler, F.R. Sheridan, *Sensor Actuat. B-Chem.*, 29 (1995), 51.
 60. O.S. Wolfbeis, R. Reisfeld, I. Oehme, *Structure Bonding*, 85 (1996), 51.
 61. R. Ostaszewski, A.M. Klonkowski, K. Kledzik, *Supramol. Chem.*, 12 (2000), 131.
 62. A.M. Klonkowski, K. Kledzik, R. Ostaszewski, *J. Incl. Phenom. Mol.*, 35 (1999), 165.
 63. A.M. Klonkowski, K. Kledzik, R. Ostaszewski, in: *Coordination Chemistry of the Turn of the Century*, G. Ondrejovic, A. Sirota (Eds.), Slovak Technical University Press, Bratislava 1999, p. 289.
 64. A.M. Klonkowski, K. Kledzik, R. Ostaszewski, J. Jezierska, *J. Mater. Chem.*, in the press.
 65. For a summarizing review containing ca. 400 references see L.N. Lewis, *Chem. Rev.*, 93 (1993), 813.
 66. G. Schmid, S. Emde, V. Maihack, M. Meyer-Zaika, St. Peschel, *J. Mol. Catal. A*, 107 (1996), 95.
 67. G. Schmid, V. Maihack, F. Lantermann, St. Peschel, *J. Chem. Soc., Dalton Trans.*, 1996, 589.
 68. G. Schmid, M. Bäuml, M. Geerkens, I. Heim, C. Osemann, T. Sawitowski, *Chem. Soc. Rev.*, 28 (1999), 179.
 69. J.S. Bradley, in: *Clusters and Colloids*. G. Schmid (Ed.), VCH Publishers, Weinheim 1994.
 70. G. Schmid, *Chem. Rev.*, 92 (1992), 1709.
 71. H. Liu, N. Toshima, *J. Chem. Soc., Chem. Commun.*, 1992, 1095.
 72. J.S. Bradley, *Chem. Mater.*, 5 (1993), 254.
 73. K. Torigoe, K. Esumi, *Langmuir*, 9 (1993), 1664.
 74. C. Larpent, F. Brisse-Le Menn, H. Patin, *Mol. Catal.*, 65 (1991), L35.
 75. T. Sato, S. Kuroda, A. Takami, Y. Yonezawa, H. Hada, *Appl. Organomet. Chem.*, 5 (1991), 261.
 76. T. Sato, *J. Appl. Phys.*, 68 (1990), 1297.
 77. T. Sato, *J. Chem. Soc., Faraday Trans. 1*, 83 (1987), 1559.
 78. H. Hirai, Y. Nakao, N. Toshima, *Chem. Lett.*, 5 (1978), 545.
 79. M. Ohtaki, M. Komiyama, H. Hirai, N. Toshima, *Macromolecules*, 24 (1991), 5567.
 80. N. Toshima, *J. Phys. Chem.*, 95 (1991), 7448.
 81. N. Toshima, *J. Phys. Chem.*, 96 (1992), 9927.
 82. H. Hirai, Y. Nakao, N. Toshima, *Chem. Lett.*, 9 (1982), 905.
 83. N. Toshima, M. Ohtaki, T. Teranishi, *Reactive Polym.*, 15 (1991), 135.
 84. H. Bönemann, W. Brijoux, R. Brinkmann, E. Dinjus, Th. Jousen, B. Korall, *Angew. Chem.*, 103 (1991), 1344; *Angew. Chem. Int. Ed. Engl.*, 30 (1991), 1312.
 85. H. Bönemann, W. Brijoux, R. Brinkmann, R. Fretzen, Th. Jousen, R. Köppler, B. Korall, P. Neiteler, J. Richter, *J. Mol. Catal.*, 76 (1994), 129.
 86. H. Bönemann, W. Brijoux, R. Brinkmann, E. Dinjus, R. Fretzen, Th. Jousen, B. Korall, *J. Mol. Catal.*, 74 (1992), 323.
 87. H. Bönemann, R. Brinkmann, P. Neiteler, *Appl. Organomet. Chem.*, 8 (1994), 361.
 88. H. Bönemann, W. Brijoux, in: *Advanced Catalysts and Nanostructured Materials. Modern Synthetic Methods*. W.R. Moser (Ed.), Academic Press, San Diego 1996, Chap. 7.

Redispersible nanopowders for wet chemical coating processes. Application to transparent conducting coatings*

N. AL-DAHOUDI, M.A. AEGERTER**

Institut für Neue Materialien gem. GmbH-INM, Department of Coating Technology,
Im Stadtwald, Geb. 43, 66123 Saarbruecken/Germany

$\text{In}_2\text{O}_3:\text{Sn}$ (ITO) sols made of crystalline nanoparticles fully redispersable in an ethanol solution containing hydrolyzed organosilanes have been developed to get thick conducting transparent and antiglare coatings on substrates which do not withstand high temperature such as plastics (PMMA, polycarbonate) and already processed glasses. The coatings were deposited by spin, dip and spray coating processes and cured by UV irradiation and/or by a low temperature heat treatment ($T = 130\text{ }^\circ\text{C}$) in air and reducing atmosphere. Their electrical, optical, textural and mechanical properties are reported. Stable sheet resistance as low as $2\text{ k}\Omega$ was obtained with a single 500 nm thick transparent layer. Antiglare-antistatic coatings exhibiting similar sheet resistance, a gloss of 60–70 GU, a clarity of 75–90% and an optical resolution > 8 lines/mm were obtained by a room temperature spraying process. The abrasion resistance of the transparent coatings is in agreement with DIN 58196 G10 – class 1, the adhesion with DIN 58196-K2 (tape test) and the pencil hardness (ASTM D 3363-92a) is 1H.

Key words: sol-gel, coatings, electronic conductivity, ITO nanoparticles, low temperature processing, plastic substrates

1. Introduction

Transparent conducting inorganic (TCO) coatings are today widely used as electrodes in optoelectronic devices (displays, smart windows and mirrors, etc.), as IR reflecting layers in low-emissivity glazings and oven windows, as heatable layers in defrosting windows, for electromagnetic shielding or dissipating static, etc. The most important materials bearing such properties are very thin metal layers (Ag, Au, etc.), conducting polymers and n-type oxide semiconductors such as indium tin oxide (ITO), fluorine or antimony doped tin dioxide (FTO, ATO), aluminium or gallium-doped zinc oxide (AZO, GZO).

*The paper presented at the International Conference on Sol-Gel Materials, SGM 2001, Rokosowo, Poland.

**Corresponding author: phone 0049-681-9300-317, fax: 0049-681-9300-249, email: aegerter@inm-gmbh.de.

For the last group of materials practically all physical and chemical processes have been tested [1]. Wet chemical processes such as CVD, AACVD, spray pyrolysis and conventional sol–gel techniques require either a hot substrate ($T > 400$ °C) or a substrate which can be heated after the deposition to such a high temperature. These processes are therefore only adequate to coat glasses [2]. Moreover the conventional sol–gel process does not allow the deposition of thick layers and low sheet resistance can only be obtained with a multilayer coating. As it is necessary to repeat the whole coating procedure (deposition, drying, sintering) many times, the process is not well adapted for industrial application.

There is therefore a great interest to find a way to deposit by a sol–gel technique (spray, dip and spin coating) a single thick conducting layer, especially on substrates which do not withstand high temperature such as plastic materials and already processed glass devices. Till now, only physical deposition techniques are adequate [2].

One possible issue for the development of thick TCO coatings is the use of hybrid organic-inorganic sols containing a very large amount of already conducting crystalline oxide nanoparticles. Hybrid sols are known to allow the deposition of thick coatings which can be fully processed at low temperature, $T < 130$ °C (and also at high temperature). A high filling of the sol with crystalline n-type semiconducting nanoparticles which can be linked together with an adequate organic binder should assure a reasonable conductivity. Moreover, the use of nanoparticles assures a low light scattering and a high transparency of the coatings. $\text{In}_2\text{O}_3:\text{Sn}$ (ITO) and $\text{SnO}_2:\text{Sb}$ (ATO) conducting crystalline nanoparticles have been already developed in our institute. Their preparation, characterization and use for the development of conducting ATO membranes and ATO and ITO coatings sintered at high temperature have been reported [3–8].

The present paper summarizes the optical, electrical, mechanical and textural properties of thick transparent and antiglare conducting ITO coatings processed at temperature as low as 130 °C and deposited on plastics and glasses. Earlier reports can be also found in [9–11].

2. Experimental

The detailed preparation of redispersible crystalline ITO nanoparticles can be found in [9]. They exhibit the cubic In_2O_3 phase and no phase separation or orientation of the crystallites have been detected. The crystallite size determined by X-ray diffraction (222 peak) or transmission electron microscopy (TEM) is about 15 nm. The particles have a density of 6.45 g/cm^3 corresponding to 92% of the theoretical density of In_2O_3 . The agglomerated particles can be fully redispersed in ethanol or water down to their primary size (ca. 15 nm) and a highly stable paste (> 1.5 year) have been obtained [9].

The sols developed to produce transparent conducting coatings were prepared as follows: an ethanolic solution containing 25 wt. % of redispersed ITO nanoparticles was modified by adding various amounts of hydrolyzed 3-glycidoxypropyltrimethoxy-

silane (GPTS) or 3-methacryloxypropyltrimethoxysilane (MPTS) under ultrasonic bath. PMMA, polycarbonate (PC) and glass substrates were coated by spin and dip coating process. The resulting films were cured in air or reducing atmosphere at 130 °C up to 20 hours, by UV irradiation with an average intensity of 105 mW/cm² during up 110 s (Beltron) or by a combination of both treatments.

The sols developed to produce antiglare conducting coatings were prepared as follows: an ITO nanoparticles solution (25 wt. %) was modified by adding GPTS. The sols were sprayed at room temperature for a period of 15 to 20 seconds using a SATA mini-jet spray gun (0.5 mm nozzle, 3 bar) on polycarbonate or glass substrates. The coatings, a few μm thick, were polymerized by UV irradiation (105 mW/cm², during 100 s).

The thickness of the coatings t was determined using a Tencor P10 stylus profilometer and the average roughness was measured with a Zygo New view 5000 white light interferometer. The morphology of the coatings (surface and cross section) was observed by scanning electron microscopy (SEM JEOL 6400) and HR-TEM (Philips, 200 keV), respectively. The abrasion resistance of the coatings was tested according to DIN 58196-G10 – rubbing with an eraser under a load of 9.8 N and DIN 58196-H25 – rubbing with a cloth under a load of 9.8 N, their hardness using the pencil test (ASTM D 3363-92a) and their adhesion using the tape test DIN 58196-K2.

Optical transmission and reflection were determined using a Variant Cary 5 E spectrophotometer in the wavelength range from 300 to 3000 nm while haze, clarity and gloss of the antiglare coatings were measured using a ByK Gardner Plus and a micro-TRI reflectometer.

The sheet resistance R_s was measured by a 4-point technique and a contactless measurement device (Leighton Electronics Inc.). The resistivity was calculated from $r = R_s \cdot t$.

3. Results and discussion

3.1. Transparent conducting coatings

The evolution of the sheet resistance of a 500 nm thick single layer MPTS/ITO coatings deposited on a 3 mm thick PC substrate is shown in Fig. 1 as a function of the sol composition for different annealing treatments, such as heat treatment in air, UV irradiation and annealing in nitrogen gas. Similar overall behaviour has been obtained with GPTS/ITO coatings. Whatever the treatment is, R_s for pure ITO remains high ($> 1 \text{ M}\Omega$.) and the coating adhesion is poor. Cured MPTS/ITO coatings present a minimum of the sheet resistance for a composition volume ratio of 6%. A heat treatment in air at 130 °C only slightly decreases the sheet resistance. In fact, IR spectroscopy shows that contrary to what can be observed with pure MPTS coatings, the heat treatment does not build a well defined Si-O-Si network (observed at 1050 cm⁻¹) and the presence of ITO particles seems to impede the polymerization and condensation processes [9]. On the opposite the UV treatment drastically reduces the

sheet resistance. IR spectroscopy [9] shows that this treatment eliminates completely the C=C band (1036 cm^{-1}), strongly reduces the C=O band (1716 cm^{-1}) so that a well defined Si-O-Si network linking the conducting particles together is built allowing a much better conductivity. The lowest stable sheet resistance, $R_s = 15\text{ k}\Omega$ for GPTS/ITO and $R_s = 2\text{ k}\Omega$ for MPTS/ITO, have been obtained after a 110 s UV irradiation followed by a 15 h heat treatment in air at $130\text{ }^\circ\text{C}$. A further treatment in a reducing atmosphere (N_2) still lowers the value of the sheet resistance.

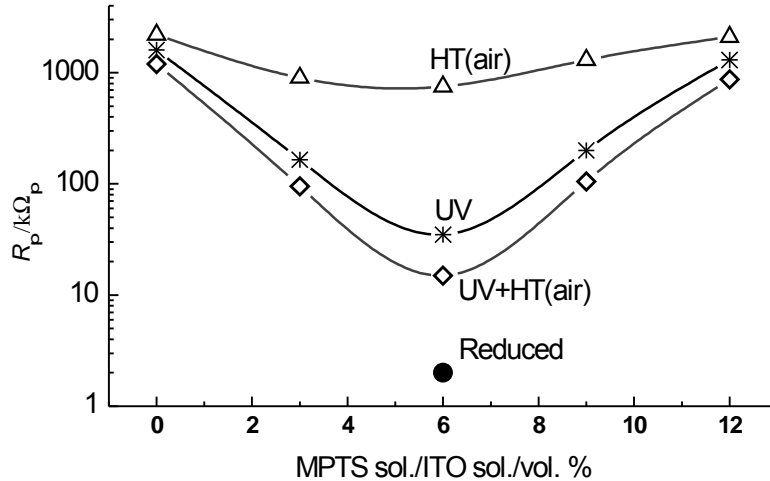


Fig. 1. Sheet resistance of 500 nm thick MPTS/ITO coatings vs. sol composition; UV: irradiation by UV light $105\text{ mW}\cdot\text{cm}^{-2}$, 110 s, HT (air): heat treatment in air: $130\text{ }^\circ\text{C}$, 15 h

The values reported above have been measured in air at least one week after the coating's production and are stable. They however strongly depend on the type of atmosphere and the shelf life. Figure 2 shows the time evolution $R_p(t)$ measured for 500 nm thick MPTS/ITO coatings obtained without and with post-annealing in reducing atmosphere (N_2) and then left in vacuum and in air (about 50% RH). Immediately after the coating production the values of the sheet resistance are much smaller than those reported above, typically $800\text{ }\Omega$ for N_2 annealed coatings. They remain constant in vacuum but steadily increase in air, to reach a maximum stable value ($2\text{ k}\Omega$) after about 7 days. Similar overall behaviour was observed with GPTS/ITO coatings.

The mechanisms leading to these variations are not yet clear, but are certainly related to the composition and the morphology of the coatings. Besides the polymerization process of MPTS an important effect of both the UV and the reducing treatment is probably to diminish the concentration of chemisorbed oxygen species on the surface of the ITO particles, which act as free electron traps surface states. This leads to an increase of the carrier concentration and consequently to a large reduction of the sheet resistance. As the coatings are still porous (see below) this behaviour is only stable if the coatings are kept in vacuum. When left in air, oxygen slowly diffuse into

the coating and is chemisorbed again at the surface grains as charged species resulting in an electron transfer from the bulk to the adsorbed species. This induces a high band bending and increases the potential barrier height leading to an increase of the resistivity which reaches a stable value after about 5–7 days [12]. In this sense the coatings act practically as a (poor) oxygen sensor.

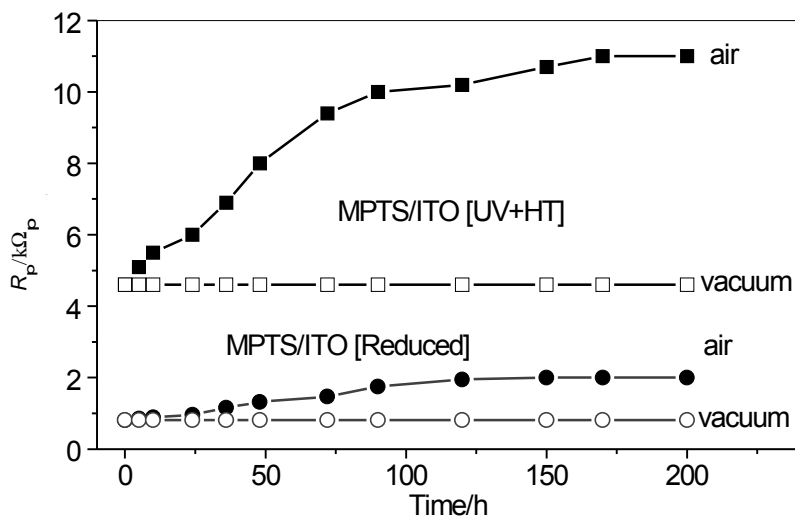


Fig. 2. Time evolution of the sheet resistance of 500 nm thick MPTS/ITO (6 vol. %) coatings left in vacuum and air. The coatings have been annealed in UV light ($105 \text{ mW}\cdot\text{cm}^{-2}$, 110 s) followed by a 15 h heat treatment in air at $130 \text{ }^\circ\text{C}$ with and without post annealing in a N_2 reducing atmosphere

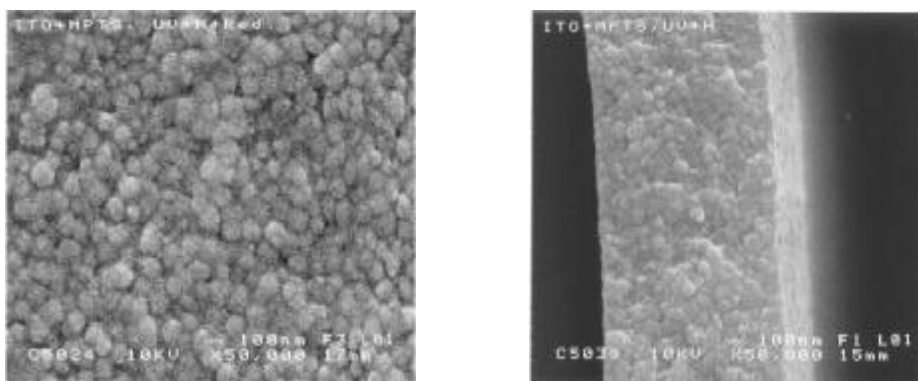


Fig. 3. SEM picture of the surface (left) and of a cross-section (right) of a MPTS/ITO coating UV cured (110 s) and heat treated at $130 \text{ }^\circ\text{C}$, 15 h

The morphology of the coatings is shown in Fig. 3. The coating cured is built of loosely packed globular grains (raspberry like) about 100 nm in size. Each grain is

made of an aggregation of 15 nm size ITO particles linked together by a small strip of polymerized MPTS (dark region on the figure).

The optical transmission and reflection spectra of a 3 mm thick PC substrate uncoated and one coated with a 500 nm GPTS/ITO layer are shown in Fig. 4. A high transmission of about 87% is observed in the visible range. The influence of the carrier is clearly seen by the strong absorption occurring in the near IR range (900 nm $< \lambda < 2000$ nm) and the increase of the reflection for $\lambda > 2 \mu\text{m}$.

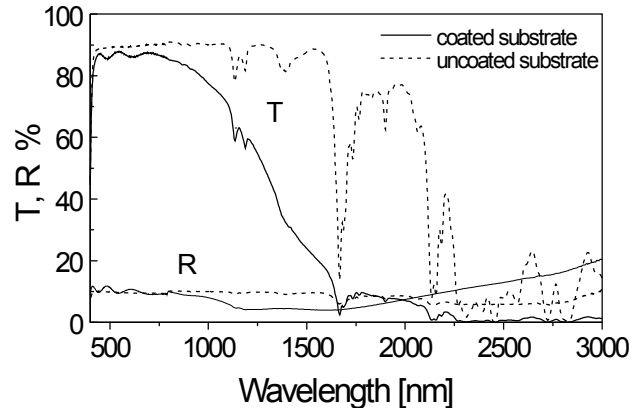


Fig. 4. UV-near IR transmission (T) and reflection (R) measured against air of a 500 nm thick GPTS/ITO coating deposited on a 3 mm thick polycarbonate (PC) substrate and of an uncoated PC substrate

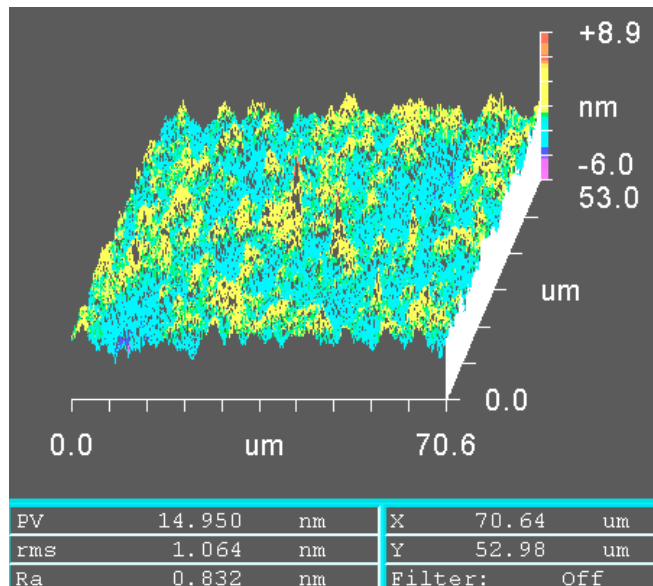


Fig. 5. Morphology of the surface of a 500 nm thick MPTS/ITO coating measured by white light interferometry with a lateral resolution of 600 nm

The morphology of the surface of the coating measured by white light interferometry with a lateral resolution of 600 nm is shown in Fig. 5. The coatings are extremely smooth and homogeneous with a roughness value $R_a = 0.85$ nm, with a peak-to-valley maximum value of $PV = 14.9$ nm (probably a dust particle).

The mechanical properties of the coatings deposited on PC substrate have been studied by various tests and are compared in Table 1 with two other commercial coatings, a Japanese product and a Baytron P conducting polymer coating [13].

Table 1. Mechanical properties of conductive coatings deposited on PC substrate

Test	INM (500 nm, $R_{\infty} = 2 \text{ k}\Omega_{\infty}$)	Japanese Product ($R_{\infty} = 50 \text{ k}\Omega_{\infty}$)	Baytron P® (500 nm, $R_{\infty} = 8 \text{ k}\Omega_{\infty}$)
Tape test DIN 58196-K2	OK	OK	OK
Eraser test DIN 58196-G10	class 1	class 3	class 1
Pencil test ASTM D3363-92a	1 H	HB	1 H

The results show that the adhesion property tested using the Tape test procedure was good for all of them. No scratch (class 1) could be observed after 10 cycles with an eraser under a load of 10 N with our coatings and a 500 nm thick, 8 $\text{k}\Omega_{\infty}$ polymer coating made with the Baytron P product [13], but the Japanese product was highly scratched (class 3). The hardness measured using the Pencil test was 1H for our coating, HB for the Japanese product and 1 H for the Baytron P coating.

3.2. Antiglare conducting coatings

The spray gun delivers droplets with average size of 25 μm . When arriving on the cold substrate, they spread and form a rough surface which can be polymerized by UV irradiation or by heating at $T \approx 130$ °C. The thickness of the coatings is in the range of a few μm .

Table 2. Typical gloss, haze, clarity, resolution and abrasion of antiglare coatings deposited on plastic and glass substrates and cured by UV irradiation

Gloss @ 60°	Haze/%	Clarity/%	Resolution (USAF chart)	Abrasion (9.8 N)
60–70	≤ 10	75–90	≥ 8 lines/mm	DIN 58196-H 25

XRD measurements are in agreement with the random cubic In_2O_3 structure with crystallite size reflecting the size of the ITO particles (15 nm). Figure 6 shows the surface morphology of such coatings observed with an optical microscope. The size of

the surface features varies from about 10 to 100 μm and the average roughness of the coatings measured by the profilometer along a 500 μm length is $R_a = 0.2 \mu\text{m}$ with height variation of $\pm 0.4 \mu\text{m}$. The sheet resistance is about $2.5 \text{ k}\Omega$. Table 2 shows the results of the optical and abrasion properties of the coatings.

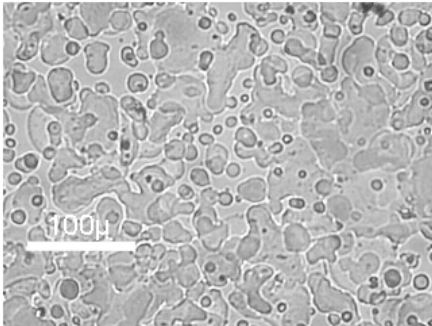


Fig. 6. Surface morphology of antiglare coatings sprayed at room temperature on a PC substrate and UV polymerized

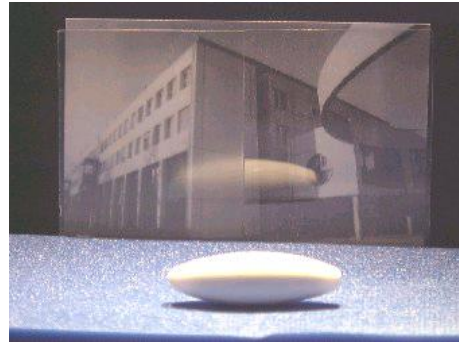


Fig. 7. Glare of a white object placed in front of a AS-AG coated plastic (left) and an uncoated one (right). The picture of the building placed 2 cm behind the substrates is clearly visible in both configurations

Figure 7 shows the optical effect of such coatings. The image (entrance of INM) placed 2 cm behind a coated and a non-coated substrate is clearly visible and the glare of the white object placed in front of the substrates is strongly reduced at the coated side.

4. Conclusions

Stable hybrid pastes and sols allowing the deposition of conducting, antistatic and antiglare-antistatic coatings fully processable at low temperature ($T < 130 \text{ }^\circ\text{C}$) have been developed. They have been obtained by modifying an ethanolic suspension of dispersed crystalline ITO nanoparticles with hydrolyzed silanes (GPTS/MPTS) acting as a binder. Transparent ($T \sim 90 \text{ }^\circ\text{C}$) single layers as thick as 500 nm have been obtained by spin or dip coating processes on plastic (PMMA, PC and glass substrates). The curing process involves a UV irradiation (105 mW/cm^2 , 110 s) followed by a heat treatment at $T = 130 \text{ }^\circ\text{C}$ during 15 h and then a reducing treatment in nitrogen. The coating exhibits a stable sheet resistance as low as $2 \text{ k}\Omega$. (resistivity $r = 1.0 \cdot 10^{-1} \Omega \cdot \text{cm}$). The abrasion resistance is in agreement with DIN 58196-G10 class 1, the pencil hardness is 1 H and the adhesion passes the tape test ASTM D 3363-92c. The roughness is low, $R_a = 1 \text{ nm}$. Antistatic coatings with similar sheet resistance presenting an antiglare effect ($\text{GU} \sim 65$) have been obtained on the same substrates by a spray process at room temperature followed by a UV annealing. All these coatings are stable under UV or visible light irradiation. Their properties are presently better than those obtained with commercial conductive polymers.

References

- [1] HARTNAGEL H.L., DAWAR A.L., JAIN A.K., JAGDISH G., *Semiconducting Transparent Thin Film*, 1995, Bristol, IOP Publishing.
- [2] PULKER H.K., *Coatings on Glass*, 2nd ed., 1999, Elsevier.
- [3] GOEBBERT C., AEGERTER M.A., BURGARD D., NASS R., SCHMIDT H., Proc. Materials Research Society, MRS, Nanostructured Powders and their Industrial Application, 520, 293–309, 1998.
- [4] BURGARD D., GOEBBERT C., NASS R., SCHMIDT H., AEGERTER M.A., *J. Sol–gel Science and Technology*, 1998, 13, 789–792.
- [5] GOEBBERT C., AEGERTER M.A., BURGARD D., NASS R., SCHMIDT H., *J. Mater. Chem.*, 1999, 9, 253–258.
- [6] GOEBBERT C., NONNINGER R., AEGERTER M.A., SCHMIDT H., *Thin Solid Film*, 1999, 351, 79–84.
- [7] GOEBBERT C., BISHT H., NONNINGER R., AEGERTER M.A., SCHMIDT H., Proc. Materials Research Society, MRS, Multicomponent oxide films for electronics, 1999, 574, 199–204.
- [8] GOEBBERT C., BISHT H., AL-DAHOUDI N., NONNINGER R., AEGERTER M.A., SCHMIDT H., *Journal of Sol–Gel Science and Technology*, 2000, 19, 201–204.
- [9] AL-DAHOUDI N., BISHT H., GOEBBERT C., KRAJEWSKI T., AEGERTER M.A., *Thin Solid Film*, 2001, 392, 299–304.
- [10] AL-DAHOUDI N., AEGERTER M.A., [in]: Proc. of the Sixth International Conference on Frontiers of Polymers and Advanced Materials ICFPAM, 4–9 March, 2001, Recife/Brazil, in print.
- [11] AL-DAHOUDI N., AEGERTER M.A., [in]: Proceedings of the 1st International Materials Symposium MATERIALS 2001, 9–11 April, 2001, Coimbra/Portugal, in print.
- [12] CASTRO M.S., SUÁREZ M.P., ALDAO C.M., *J. of the European Ceramic Society*, 2001, 21, 1115–1119.
- [13] Made by dip coating according to the Baytron® P Technical Information.

Opportunities for sol-gel materials in fuel cells*

LISA C. KLEIN

Rutgers-the State University of New Jersey, Ceramic & Materials Engineering,
607 Taylor Road, Piscataway, NY 08854-8065, USA

Fuel cells are electrochemical devices that convert the chemical energy of a fuel and oxidant directly to electrical energy. Three types of fuel cells are (a) proton-exchange membrane fuel cells (PEMFC), (b) molten carbonate fuel cells (MCFC) and (c) solid oxide fuel cells (SOFC). In each case, there is a role for sol-gel processing. In the case of PEMFC, sol-gel modifications to the membrane are designed to increase the operating temperature. In the case of MCFC, sol-gel corrosion barriers extend the lifetime of the current collector. Finally, sol-gel processing is being used to assemble the electrolyte and electrode layers in SOFC and related oxygen generating devices. Examples are given for the application of sol-gel processing in each system, pointing out the derived benefits and areas for further development.

Key words: sol-gel materials processing, fuel cells, proton exchange, molten carbonate, solid oxide

1. Introduction

Fuel cells are electrochemical cells that convert the chemical energy of a fuel and an oxidant to electrical energy by a process involving an invariant electrode-electrolyte system [1]. Fuel cell systems are built for a wide range of power requirements from a few hundred watts to megawatts. Transportation fuel cells are being promoted for their high-energy efficiency and low emissions, compared to internal combustion engines. In addition, fuel cells are being developed for stationary applications, as back up generators and co-generation systems.

Sol-gel processing is finding its way into the fabrication of fuel cell components. Our interest is to find places where sol-gel processing offers either an advantage or unique capability. In some cases, sol-gel processing is a substitution for a conventional process, for example, where tape cast layers are used in a solid oxide fuel cell. In other cases, sol-gel processing offers a new approach, for example, where gel is incorporated into a polymer for a proton exchange membrane (also called polymer

*The paper presented at the International Conference on Sol-Gel Materials, SGM 2001, Rokosowo, Poland.

electrolyte) fuel cell. The motivation for trying sol–gel processing is based on our previous use of sol–gel processing in other electrochemical devices, both lithium-ion batteries and electrochromic displays.

2. Previous use of sol–gel processing in electrochemical devices

2.1. Lithium ion batteries

Recall for a moment, the basic galvanic cell. The cell consists of an anode, a cathode and an electrolyte. In a lithium rechargeable battery, the cathode material is an intercalation compound with a layered or framework structure [2].

On charging the Li is oxidized at the cathode:



and reduced at the anode



In lithium batteries, sol–gel processing has been applied principally to the solid electrolyte [3].

The electrolyte is the critical feature in a galvanic cell, including fuel cells, because it has to transport ions back and forth between the cathode and anode. The electrolyte has to have a wide electrochemical potential window and stability during charge/overcharge and discharge/over-discharge. A solid electrolyte has to have mechanical stability. While it serves as a separator and membrane, it is also rigid, holding the components of the cell fixed.

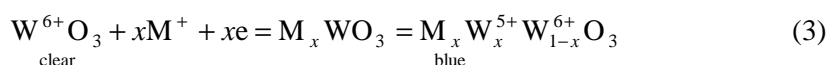
One problem with solid electrolytes is that they may not have high ionic conductivity. One way around this problem is thin film electrolytes. A natural advantage of the sol–gel process is the fact that a film of oxide can be deposited directly from solution [4].

It is well known that ionic transport in solid electrolytes is an activated process, and the temperature dependence of ionic conductivity is represented by an Arrhenius-type equation with apparent activation energy. In most fast ion conductors, the activation energy is indicative of the energy of motion rather than the energy to form charge carriers. That is the population of mobile carriers is high and needs only to be set in motion. The desired features in a fast ion conductor are a large number of mobile ions, a large number of sites for the ions, relatively low activation energy, and ease of fabrication in complex shapes. Compared to crystalline fast ion conductors, sol–gel processed ion conductors, in particular lithium containing silicates, are isotropic, have more channels for fast ion conduction, and have fewer restrictions on composition [5].

2.2. Electrochromic devices

Another example of a galvanic cell is an electrochromic (EC) device, which is a multilayer construction where one of the layers shows electrochromic properties [6–8]. Certain compounds, especially oxides of polyvalent metals, exhibit coloration that depends on the oxidation state of their cations. This property leads to electrochromism, which is a reversible and visible change in transmittance. The oxidation–reduction reactions are electrochemically induced using low voltages, on the order ± 1 V dc.

The most well known “chromogenic” material is tungsten trioxide (WO_3) forming deep blue alkali and hydrogen tungsten bronzes (M_xWO_3) on reduction. The reaction is expressed by the following equation:



where M is hydrogen or alkali and $0 < x < 1$.

There are several approaches to the preparation of transition metal oxides [9]. One of the routes is to prepare a solution using alkoxides only. The available alkoxides are only slightly soluble in common organic solvents and are very reactive with water, making them difficult to handle. Another route is to use salts such as oxychlorides as the network former oxide precursor. The third route is to use colloidal sols. A sol, which is a colloidal suspension of small particles (1–1000 nm) in a liquid, is obtained after hydrolysis–condensation reactions of the precursor. The least expensive precursor is tungstic acid. Other reasons for choosing tungstic acid are its aqueous nature, its ability to be recycled, the presence of W–O–W bonds in the sols, and the absence of crystallinity. One drawback of tungstic acid sols is that they turn into a gel in 30 min.

For sol–gel electrolytes in electrochromic devices, the primary advantage is high lithium ionic conductivity [10]. Of course, the electrolyte has to have high electronic resistivity, high ionic conductivity, and no defects (pinholes). The commercially introduced devices have “no moving parts” meaning no mobile protons that will defeat the memory capability of the device [11].

For lithium batteries and electrochromic devices, sol–gel processing seems well suited. On the one hand, gels are inorganic and rigid, which means that the sol–gel electrolyte can operate at modest temperatures while playing the role of a mechanical divider between the electrodes. On the other hand, sol–gel processing is practical for large area coatings where sols can be applied directly to substrates and in successive sol–gel layers.

3. Use of sol–gel processing in fuel cells

Buoyed by the success of sol–gel processing in batteries and electrochromic devices, we have extended its use to other electrochemical devices and systems. Because

of the high interest in alternative power generation, fuel cells are a natural area for investigation.

3.1. Proton exchange membrane fuel cells (PEMFC)

Recent advances have made proton-exchange membrane fuel cells (PEMFC), a leading alternative to internal combustion and diesel engines for cars, trucks and buses. These advances include the reduction of the platinum electrode catalyst needed, and membranes with high specific conductivity, good water retention and long lifetimes [12]. A major limitation of the current PEMFC is that the Pt anode electrocatalysts is poisoned by CO at the 5 to 10 ppm level in the state-of-the-art fuel cells operating at about 80 °C [13, 14]. One approach to solving the CO poisoning problem is to operate at higher temperature where the free energy of adsorption of CO on Pt has a larger positive temperature dependence than that of H₂, which means that the CO tolerance level increases with temperature [15].

A complication in current PEMFC's is water management. The proton conductivity of the PEM (Nafion) increases linearly with the water content, with the highest conductivity corresponding to a fully hydrated membrane. While it is desirable to operate a fuel cell at a temperature above the boiling point of water from the standpoint of increased reaction kinetics and lower susceptibility to poisoning, the membranes lose conductivity due to drying. Membrane dehydration also causes the membrane to shrink, which reduces the contact between the electrode and membrane, leading to the crossover of the reactant gases. The problem is that the vapor pressure of water increases very rapidly with temperatures above 100 °C. In order to maintain the needed hydration for the polymeric membrane and the partial pressures of the reactant gases, the total pressure has to be increased significantly.

To solve both the CO poisoning and the water management problems, the present state-of-the-art PEM's need to be modified. One way to enhance the water retention of Nafion is incorporation of hydrophilic oxides (e.g. SiO₂). Difficulties have been encountered because the metal oxide particles are micron size and are not sufficiently small to enter the nanopore structure of the membrane [16]. To overcome this problem, a sol-gel technique has been used to introduce a polymeric oxide into the perfluorosulfonic acid membrane. Using this method, it was shown that the oxides enter the fine channels (~5 nm) [17].

Silicophosphate gels have been shown to be fast proton-conducting solids. The mobility of protons increases when the protons are strongly hydrogen-bonded. Compared with Si-OH, phosphate gels are better for high protonic conduction because the hydrogen ions are more strongly bound to the non-bridging oxygen. Also, the hydrogen in the P-OH group is more strongly hydrogen-bonded with water molecules, resulting in an increase in the temperature necessary to remove the water. The introduction of cations such as Zr⁴⁺ into silicophosphate gels results in improved chemical stability [18, 19].

We prepared a sol of composition $60\text{SiO}_2\text{-}30\text{P}_2\text{O}_5\text{-}10\text{ZrO}_2$ sol using tetraethyl ortho-silicate ($\text{Si}(\text{OC}_2\text{H}_5)_4$, TEOS), triethyl phosphate ($\text{PO}(\text{OC}_2\text{H}_5)_3$, TEP), and zirconium *n*-propoxide ($\text{Zr}(\text{OC}_3\text{H}_7)_4$, TPZr). The sol was prepared by mixing two solutions. Solution A was prepared by mixing TEOS, half the volume of propanol (solvent), TEP, HCl (to control the pH at ~ 2) and water (molar ratio of water/(TEOS + TEP) = 2) at room temperature and stirred for 1 h. Solution B was prepared by mixing TPZr, the other half of the propanol and acetylacetone (molar ratio of acetylacetone/TPZr = 1) at room temperature and stirred for 1 h. Both solutions were subsequently mixed together and stirred for 1 h. The remaining water was added drop by drop, and then the solution was stirred for 15 min. The sol has a concentration of 70 grams of solid per liter, and a final molar ratio of water/precursors = 5.5.

The preparation of the infiltrated Nafion consisted of first pre-treating the Nafion membrane with 3 vol. % H_2O_2 for 2 hours at 80 °C, followed by 50 vol. % H_2SO_4 for 2 hours at 80 °C. The membrane was treated three times in distilled H_2O at 80 °C to remove any excess acid. After drying for 3 days at 80 °C, the membrane was immersed in the $60\text{SiO}_2\text{-}30\text{P}_2\text{O}_5\text{-}10\text{ZrO}_2$ sol for 3 hours. Then, the membrane surfaces were cleaned with propanol to avoid the formation of surface-attached silicate layers. After the treatment, the membrane was placed at room temperature for 5 hours and then in an oven at 150 °C for 2 days. The dried infiltrated samples had an average weight increase of about 10%.

For the fuel cell experiments, the Pt/C fuel electrodes (E-TEK Inc.) with a Pt loading of $0.4 \text{ mg}\cdot\text{cm}^{-2}$, were impregnated with $0.6 \text{ mg}\cdot\text{cm}^{-2}$ of Nafion (dry weight) by applying $12 \text{ mg}\cdot\text{cm}^{-2}$ of 5% Nafion solution with a brush. The electrode area was 5 cm^2 . The membrane electrode assembly (MEA) was prepared by heating the electrode/membrane/electrode sandwich to 90 °C for 1 minute in a Carver Hot-Press, followed by increasing the temperature to 130 °C for 1 minute and finally hot-pressing the MEA at 130 °C and 2 MPa for 1 minute. The MEA was positioned in a single cell test fixture, which was then installed in a fuel cell test station (Globetech Inc., GT-1000). The test station was equipped for the temperature-controlled humidification of the reactant gases (H_2 , O_2 and air) and for the temperature control of the single cell.

For the performance evaluation of the PEMFC, the single cell was fed with humidified H_2 and O_2 at atmospheric pressure (reactant gas and water vapor pressure equal to 1 atm) and the temperature of the H_2 and O_2 humidifiers and of the single cell was raised slowly to 90 °C, 88 °C and 80 °C respectively. During this period, the external load was maintained at a constant value of 0.1 ohm, to reach an optimal hydration of the membrane using the water produced in the single cell. After the single cell had reached stable conditions (i.e. current density remained constant over time at a fixed potential), cyclic voltammograms were recorded at a sweep range of $20 \text{ m}\cdot\text{V}\cdot\text{s}^{-1}$ and in the range of 0.1 V to 1 V vs. reversible hydrogen electrode (RHE) for one hour. Cell potential vs. current density measurements were then made at a relative humidity of 90–100%. The flow rates of gases were two times stoichiometric.

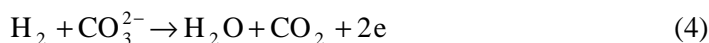
This study was carried out to know whether or not the incorporation of $\text{SiO}_2\text{-P}_2\text{O}_5\text{-ZrO}_2$ gel in Nafion enhances the current density at a fixed potential, for temperatures > 130 °C. By limiting the total pressure to 3 atm, the maximum operating temperature investigated was 140 °C since the vapor pressure of water at this temperature is 3.5 atm. In fact, we measured a significant improvement in the water management of the composite vs. the control Nafion membrane. The higher current densities and lower resistances of the composite membrane can be attributed to the water retention characteristic of the $\text{SiO}_2\text{-P}_2\text{O}_5\text{-ZrO}_2$ gel. In addition, composite membranes were less susceptible to high temperature loss of proton conductivity than unmodified Nafion. These promising results are being investigated further [20].

3.2. Molten carbonate fuel cells (MCFC)

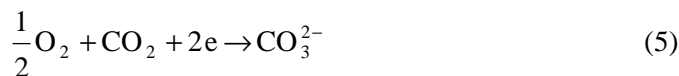
Another fuel cell design is the molten carbonate fuel cell (MCFC) [21], which operates in the temperature range 620–660 °C with an efficiency of $> 50\%$. MCFC units are produced by FuelCell Energy, Inc (Danbury, CT). These units are designed as back-up generators for intermittent use. The operational lifetimes of fuel cell systems need to be extended. In order to do so, it is necessary to limit component corrosion.

Corrosion of the lithiated NiO cathode and corrosion of the 316L stainless steel cathode current collector shorten the useful lifetime of an MCFC. The long-term performance of fuel cells depends on their resistance to degradation in an aggressive environment. The electrode reactions are:

- anode (Ni):



- cathode (NiO):



in a typical electrolyte of 62 mol % Li_2CO_3 –38 mol % K_2CO_3 at an operating temperature of 650 °C in an atmosphere containing CO, CO_2 , O_2 , H_2 , and H_2O .

During operation, the stainless steel cathode current collector forms a surface oxide, which increases the cathode/cathode current collector resistance. In addition, the surface oxide can react with the electrolyte to form LiFeO_2 and K_2CrO_4 . Hot corrosion accelerates electrolyte loss, which can cause electrode performance decay, matrix ionic resistance increase, and reactant crossover increase [22, 23]. One way to control the surface oxide formation and limit its undesirable effect is to coat the current collector, with oxides such as $\text{Li}(\text{Co,Fe})\text{O}_2$ [24].

We have prepared aqueous coatings that (1) adhere to the 316L stainless steel cathode current collector, (2) crystallize during heat treatment, (3) remain intact on

the current collector at the operating temperature of the fuel cell (650 °C), and (4) provide protection without interfering with the operation of the current collector.

The starting materials were soluble salts, cobalt acetate ($\text{Co}(\text{C}_2\text{H}_3\text{O}_2)_2 \cdot \text{H}_2\text{O}$) and iron nitrate ($\text{Fe}(\text{NO}_3)_3 \cdot 9\text{H}_2\text{O}$). These salts produce hydroxides ($\text{M}(\text{OH})_2$), oxyhydroxides (MOOH) or hydrated oxides in water, where M is Co or Fe. These solutions were reacted with lithium hydroxide. Diluted ammonium hydroxide (3M) was added to form stable colloids [25].

Lithium hydroxide and cobalt acetate were dissolved separately in distilled water. These two solutions were then mixed together and stirred vigorously. The hydrolysis of the mixture was promoted by slow addition of 3M ammonium hydroxide. Similarly, sols with ferric nitrate, or ferric nitrate plus cobalt acetate, were prepared. The sols used for coating were diluted to give a 2:1 ratio of moles water to moles oxide.

The sols were coated onto 316L stainless steel substrates using a dip-coating technique. As the surface of the substrates was somewhat rough, the samples were polished and cleaned before coating. The substrates were put into a boiling sodium carbonate/water solution to remove oil and grease, then rinsed in water, and put into a mixture of HCl/HNO_3 to remove rust and increase the activity of the surface. The substrates were rinsed again in water followed by ethanol, and dried in an oven.

During the dip-coating process, the substrates were immersed in the sol for about one minute, and then withdrawn at a speed of about 2 mm/min. After coating, the samples were put into the dryer at 100 °C and stored there until further heat treatment. After storing for up to 10 hr, the samples were heated to 650 °C for 3 hours, at a heating rate of 10 °C/min.

XRD patterns were collected from the powders of lithium cobalt oxide coatings scraped off of the substrate after heat treatment at several temperatures between 100 and 650 °C. Below 350 °C, no compounds were identified, although the diffraction patterns showed some small peaks. The first crystalline phases appeared at 350 °C, and the peaks were sharp by 550 °C. Principally, two crystalline phases exist which matched $\text{Li}_{1.47}\text{Co}_3\text{O}_4$ and a minor amount of LiFe_5O_8 . The minor phase resulted from the reaction between coating and substrate.

The XRD pattern of the powders scraped off of the substrate with nominal composition LiFeO_2 matched the pattern for LiFe_5O_8 . The coatings containing Co and Fe showed complex patterns with peaks from both the LiCoO_2 system and LiFeO_2 system.

Table 1. Coating compositions, thickness and transformation temperatures (determined by DSC)

Nominal composition	Thickness/m	Transformation temperature/°C
LiCoO_2	2.8	370–410
$\text{LiCo}_{0.5}\text{Fe}_{0.5}\text{O}_2$	1.2	225
LiFeO_2	1.2	270

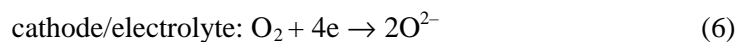
Thermal cycling tests were carried out for LiCoO_2 coatings. The cycling was from room temperature to $650\text{ }^\circ\text{C}$ for 10 cycles with a heating rate and cooling rate of $600\text{ }^\circ\text{C/h}$ and a dwell time of 0.1 hr at RT and $650\text{ }^\circ\text{C}$. This cycle was used as a simulation of how the fuel cell may be used. The microhardness was measured before and after cycling and showed little change [26]. Also, a comparison of SEM micrographs before and after thermal cycling showed the microstructures are similar. There were no obvious cracks after thermal cycling, which suggests thermal compatibility between the coating and the 316L stainless steel substrate.

4. Oxygen generators

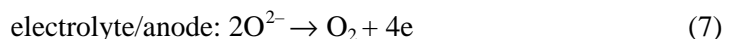
The ceramic oxygen generator is based on oxygen ion conducting technology. Its functioning is very similar to solid oxide fuel cells (SOFC). The oxygen generators that can be found in industry are usually based upon pressure swing adsorption (PSA) technology. Although they are extremely reliable, these systems have certain limitations. The purity of the oxygen is only about 95%. They require auxiliary equipment, such as inlet compressors, activators for nitrogen adsorption tanks, and the adsorbent can become ineffective when exposed to contaminated air or excess humidity.

Compared to PSA technology, ceramic oxygen generators have many advantages. The purity of the oxygen is higher (99.9%). Potentially, the size is smaller, and it is less noisy. These devices are needed for portable oxygen supplies to remote hospitals, portable welding platforms, manned space programs, and breathing air purification against contaminants such as biological agents.

An electrochemical device for oxygen generation, similar to SOFC, requires three successive layers. First, the cathode layer also serves as a catalyst for the reduction of oxygen in air. An oxygen ion-conducting layer is the electrolyte. Last, an anode layer needs to recombine the oxygen ions in O_2 . The basic operation of the oxygen generator is to make oxygen pass through an oxygen ion conducting membrane by applying a potential. Typically, an oxygen generator or SOFC operates at about $800\text{ }^\circ\text{C}$. Air diffuses through the porous cathode, usually $\text{La}_{1-x}\text{Sr}_x\text{MnO}_3$ (LSM), to the cathode/solid electrolyte interface where the oxygen is reduced:



The resulting oxygen ions cross the electrolyte under the influence of the electric field, and reach the electrolyte/anode interface. The opposite reaction of oxidation occurs, and the reformed oxygen proceeds outward through the porous anode.



The driving force for the diffusion of the oxygen ions is the difference of potential imposed by the applied voltage. Moreover, the ceramic solid electrolyte has infinite selectivity, since no gas except oxygen can cross the cell [27].

The performance of the oxygen generator depends mainly on two parameters, the current density at a given cell dc potential and the Faradaic efficiency. The current density is the amount of current that passes through a unit active area of the cell. For a commercial oxygen generator, the current density has to be at least $100 \text{ mA}\cdot\text{cm}^{-2}$.

The second parameter, the Faradaic efficiency, is a measure of the amount of current passing through an oxygen generator cell. For an oxygen generator operating at ambient pressure 1 atm and $800 \text{ }^\circ\text{C}$, the Faradaic efficiency is $13.7 \text{ cm}^3 (\text{min}\cdot\text{A})^{-1}$ when all the current is due to the oxygen ion transport. The Faradaic efficiency is then said to be 100%.

The high operating temperature leads to complex materials problems, such as interfacial diffusion, electrode sintering, and mechanical stress. In order to reduce the operating temperatures, the resistive loss occurring in the electrolyte should be minimized. One of the solutions is to decrease the thickness of the solid electrolyte from several hundred micrometers, the usual thickness in conventional cells, to a range close to ten micrometers. Among the different methods to deposit thin films, here again is an opportunity for the sol-gel process. In addition, sol-gel synthesized layers sinter at low temperature [28].

Lanthanum manganite doped with strontium (LSM) is used as the cathode material. It is also used as the anode. The solid electrolyte is yttrium-stabilized zirconia (YSZ), one of the best oxygen ion conductors at high temperature. To compensate the positive charge deficit induced by the substitution of Zr^{4+} ions by Y^{3+} ions, vacancies are created on the oxygen lattice. Moving from vacancy to vacancy, oxygen ions can diffuse through the material. Although the YSZ coating has to be thin to be an efficient ionic conductor, it remains a rigid gas separator and an electronic insulator. Platinum paste is used at the connection between the power supply and the oxygen generator.

A sol-gel process can be used for all the coatings. LSM for the cathode is at first deposited on a substrate. The YSZ for the electrolyte is then coated on the cathode. Finally LSM for the anode is deposited on the YSZ.

4.1. Yttria-stabilized zirconia (YSZ)

Due to its excellent properties as an oxygen ionic conductor, yttria-stabilized zirconia (YSZ) has been studied widely [29]. YSZ is a popular electrolyte in solid oxide fuel cells (SOFC) and is used in applications designed for oxygen separation from air.

Zirconia gels doped with yttria were prepared as follows: 60 ml of zirconium oxychloride was diluted in a mixture of water plus ethanol (1:1 by volume). Then yttrium nitrate solution (10 mole %) was added. The solution was mixed and heated up to $80 \text{ }^\circ\text{C}$ and then 50 ml of 1.5 M NH_4OH was added to promote the condensation of the species. A homogeneous white sol was obtained.

The YSZ sol, with a viscosity of about 100 cps, was applied with a brush to a platinum coated ceramic substrate. Several coatings were applied on top of each

other to build a thick enough layer. Each coating was heat-treated to 1100 °C for 5 minutes at a heating rate of 500 °C per hour to remove the organic species and to sinter this coating together with the previous one. A final heat treatment to 1200 °C at a heating rate of 500 °C per hour is done as a final sintering step.

All the samples have the stabilized cubic phase. No second phases, tetragonal zirconia or yttria oxide, were detected. The densification temperature was lower than that in the solid-state preparation where zirconia powders are reacted with yttria powder. With sol-gel processed YSZ, residual porosity is removed after firing at 900 °C for five hours [30].

The thickness increases almost linearly with the number of coatings greater than 15, with each coating contributing to approximately 0.5 micron thickness. With fewer than 30 coatings, the YSZ layers are not gas tight, but with 40 or more coatings, the YSZ can retain pressures of a few atmospheres.

For the sol-gel YSZ, both the bulk and the boundary conductivities increase with the length of the sintering heat treatment. Usually, in conventional powders, bulk conductivity is not affected by the sintering conditions, whereas the grain boundary conductivity is [31]. However, the sol-gel YSZ may experience some further densification and grain growth under the conditions of heat treatment [32, 33].

In summary, the sol-gel route to process YSZ electrolyte leads to dense and thin layers (about 20 microns) whose thickness can be controlled by the number of applied coatings. A minimum number of coatings are required to obtain gas-tight layers, due to the presence of microstructural defects on the outer surface. The conductivity of the YSZ layers improves with the length and the number of heat treatments, which promote further densification of the oxide. However, the conductivity is still lower than reported for conventional powder processing [34]. The lower values result from inhomogeneities in the microstructure remaining when all the coatings do not receive the same number of heat treatments. Nevertheless, those defects may play a role when applying the LSM gel coatings on top of the YSZ layer, since they enable the formation of an intermediate electrode/electrolyte mixed area, which reduces the interfacial voltage drop.

4.2. Lanthanum strontium manganite (LSM)

Several properties of the lanthanum manganite doped with strontium recommend it as an electrode for the oxygen generator. First of all, $\text{La}_{1-x}\text{Sr}_x\text{MnO}_3$ is a good electronic conductor. To compensate the decrease of positive charge due to the substitution of La^{3+} cations by Sr^{2+} cations, some manganese cations change their degree of oxidation from 3+ to 4+. The electrons can hop between the Mn^{3+} and Mn^{4+} . The electronic conductivity increases when the content of doping ions increases, because the concentration in Mn^{4+} ions increases. LSM is known to exhibit a semiconductor behavior for $x \geq 0.5$ and a metallic behavior for $x \leq 0.5$ [35, 36]. LSM is also an oxygen ion conductor, so a charge transfer from the bulk enhances its electrocatalytic

activity. The number of oxygen vacancies in $\text{La}_{1-x}\text{Sr}_x\text{MnO}_3$ is assumed to be close to zero when $x = 0.5$.

In the present investigation, $x = 0.33$ to achieve a high electrical conductivity, high electrocatalytic activity, and a thermal expansion compatible with YSZ. Several low temperature synthesis routes, based on solution chemistry methods, have used to prepare LSM. First, the so-called Pechini, process mixes a hydrocarboxylic acid (often citric acid) and a poly(hydroxyl alcohol) (usually ethylene glycol) with the cation salts dissolved in water. After a short time at about 100 °C, polyesterification occurs, homogeneously distributing the cations throughout the polymer. The common cation salts are nitrates [37, 38], carbonates [39], chlorides or hydroxides [40].

$\text{La}_{0.66}\text{Sr}_{0.33}\text{MnO}_3$ was prepared with lanthanum nitrate, lanthanum acetate and lanthanum chloride. After dissolution in water, they were mixed with manganese acetate and strontium nitrate, and then stirred for half an hour. A gel formed after addition of citric acid which protonates the ligands. Ethylene glycol was used for esterification and to improve solubility. Finally ammonium hydroxide was added for peptization, followed by stirring for one hour.

Within two days at 50 °C, the gels made with the $\text{La}(\text{NO}_3)_3$ and $\text{La}(\text{CH}_3\text{COO})_3$ were completely dried, whereas the one made with LaCl_3 only turned into a stiff, transparent cake. All gels then were dried at 80 °C for one day. The powders obtained after grinding were heated up to 1100 °C.

Pure LSM is observed on the XRD patterns of the powder heated at 770 °C and 1100 °C for one hour. The symmetry of the perovskite is the same for all three La-precursors, rhombohedral. The various structures of the manganite are well known [41]. The perovskite symmetry is largely determined by the concentration of Mn^{4+} cations. Mn^{4+} cations are smaller than Mn^{3+} cations, and their substitution leads to lattice shrinkage. In undoped manganite, the excess of oxygen atoms in the lattice controls the concentration of Mn^{4+} . The crystal structure depends strongly on the preparation procedure, especially the firing temperature and atmosphere. In contrast, the level of substitution fixes the concentration of Mn^{4+} cations. The temperature dependence of the conductivity is linear with a slight negative slope. While the bulk conductivity in this composition should be electronic, it appears that the small grain size and large grain boundary area are controlling the conductivity of the LSM porous electrodes [42,43]. The activation energies for samples prepared with the nitrate were lower than those prepared with the chloride or acetate, suggesting the lanthanum nitrate is the preferred lanthanum precursor for the electrodes.

Finally, the thermal expansion characteristics of $\text{La}_{0.66}\text{Sr}_{0.33}\text{MnO}_3$ and YSZ are well matched. The match is simplified because the electrode is porous, that is the contact areas between the LSM and the YSZ are small. Moreover, LSM presents a high catalytic activity for the reduction of the oxygen molecules. The major part of the oxygen ions that enter the electrolyte vacancies comes from reactions of dissociation and ionization of oxygen molecules at the Triple Phase Boundary (TPB). As its name indicates, the three phases are present in this zone located at the electrode/electrolyte interface: air, electrolyte and cathode. Starting with the oxygen

molecule and ending with the transport of oxygen ions in the electrolyte, adsorption of the molecule on the surface of the electrode, dissociation of the adsorbed molecule and finally ionization of the adsorbed atoms are all required.

In addition, LSM has good mechanical properties and long-term stability at 800 °C. It is chemically inert toward the surrounding gas, and it is chemically compatible with the YSZ, even though small amounts of undesirable phases, like La_2ZrO_7 or SrZrO_3 , appear at the interface, increasing slightly the overpotential [44].

In summary, the efficiency of the oxygen generator depends on its microstructure. The LSM electrode material has to be porous and to have a small particle size to optimize the active surface area at the TPB. At the same time, the YSZ electrolyte has to be dense and air tight. Both have to reach their final microstructure in one final heat treatment at 1200 °C in order to produce the working device. Sol-gel processing is the key to assembling the consecutive layers.

5. Conclusions

In conclusion, sol-gel processing has been used to prepare a number of complex oxide compositions. By using the sol-gel process, components that appear in fuel cells have been fabricated. These examples show the advantages of sol-gel processing for (1) forming hybrids with polymers, (2) depositing thin films in consecutive layers, and (3) creating layers that densify at temperatures below 1200 °C.

Acknowledgements

The following co-workers are thanked for their many contributions to the experimental work: Mario Aparicio, CSIC-Madrid, Spain, Sandra Mege, Altis, Paris, France, Wenzhe Chen, Fuzhou University, PRC, Mathieu Bervas and Manny Alvarez, Rutgers University.

References

- [1] KORDESCH K., SIMADER G., *Fuel Cells and Their Applications*, 1996, New York, VCH, Weinheim.
- [2] BARBOUX P., TARASCON J.M., SHOKOOHI F.K., *J. Solid State Chem.*, 1991, 94, 185.
- [3] KLEIN L.C., HO S.F., SZU S-P., GREENBLATT M., [in:] *Applications of Analytical Techniques to the Characterization of Materials*, D.L. Perry (Ed.), 1991, Plenum Press, New York, p. 101.
- [4] BRINKER C.J., HURD A.J., FRYE G.C., SCHUNK P.R., ASHLEY C.S., [in:] *Chemical Processing of Advanced Materials*, L.L. Hench and J.K. West (Eds.), 1992, New York, Wiley, p. 395.
- [5] BOILOT J.P., COLOMBAN PH., [in:] *Sol-gel Technology for Thin Films, Fibers, Preforms, Electronics and Specialty Shapes*, L.C. Klein (Ed.), 1988, New York, Noyes Publication, p. 303.
- [6] BAUCKE F.G.K., *Materials Science and Engineering*, 1991, B10, 285.
- [7] GREENBERG C.B., *Thin Solid Films*, 1994, 251, 81.
- [8] GRANQVIST C.G., *Electrochimica Acta*, 1999, 44, 3005.

- [9] LIVAGE J., [in:] *Solid State Ionics III*, G-A. Nazri, J. M. Tarascon and M. Armand (Eds.), MRS 293, 1993, Pittsburgh PA, p. 261.
- [10] MOUCHON E., KLEIN L.C., PICARD V., GREENBLATT M., [in:] *Better Ceramics Through Chemistry VI*, Eds. A. Cheetham, C.J. Brinker, M.L. Mecartney, C. Sanchez, MRS, 1994, 346, 189.
- [11] CRONIN J.P., TARICO D.J., TONAZZI J.C.L., AGRAWAL A., KENNEDY S.R., *Solar Energy Materials and Solar Cells*, 1993, 29, 371.
- [12] WAKIZOE M., VELEV O.A., SRINIVASAN S., *Electrochimica Acta*, 1995, 40, 335.
- [13] LEE S.J., MURKERJEE S., TICIANELLI E.A., MCBREEN J., *Electrochimica Acta*, 1999, 44, 3283.
- [14] DENIS M.C., LALANDE G., GUAY D., DODELET J.P., SCHULZ R., *J. Applied Electrochemistry*, 1999, 29, 951.
- [15] KREUER K.D., *Solid State Ionics*, 1997, 97, 1.
- [16] ANTONUCCI P.L., ARICO A.S., CRETIP., RAMUNNI E., ANTONUCCI V., *Solid State Ionics*, 1999, 125, 431.
- [17] MAURITZ K.A., *Materials Science and Engineering*, 1998, C6, 121.
- [18] NOGAMI M., MIYAMURA K., ABE Y., *J. Electrochemical Society*, 1997, 144, 2175.
- [19] NOGAMI M., NAGAO R., CONG W., ABE Y., *Journal of Sol-Gel Science & Technology*, 1998, 13, 933.
- [20] APARICIO M., KLEIN L.C., ADJEMIAN K., BOCARSLY A., [in:] *Ceramic Transactions: Materials for Electrochemical Energy Storage and Conversion*, A. Manthiram, G. Ceder, P.N. Kumta, S.K. Sundaram (Eds.), American Ceramic Soc., Westerville OH, 2001.
- [21] YUH C., JOHNSEN R., FAROQUE M., MARU H., *J. Power Sources*, 1995, 56, 1.
- [22] BIENDENKOPF P., SPIEGEL M., GRABKE H.J., *Materials and Corrosion*, 1997, 48, 731.
- [23] MURAI M., TAKAZAWA K., SOEJIMA K., SOTOUCHI H., *J. Electrochemical Soc.*, 1996, 143, 2481.
- [24] MAKKUS R.C., HEMMES K., DEWIT J.H.W., *J. Electrochemical Soc.*, 1994, 141, 3429.
- [25] BARBOUX P., TARASCON J.M., SHOKOOHI F.K., *J. Solid State Chemistry*, 1991, 94, 185.
- [26] CHEN W., KLEIN L.C., HUANG C., *J. Sol-Gel Science & Technology*, 2001, 27, 203.
- [27] MINH N.Q., *J. Am. Ceram. Soc.*, 1993, 76, 566.
- [28] OKUBO T., NAGAMOTO H., *J. Mater. Sci.*, 1995, 30, 749.
- [29] WEN T.L., HERBERT V., VILMINOT S., BERNIER C., *J. Mater. Sci.*, 1991, 26, 3787.
- [30] OKUBO T., NAGAMOTO H., *J. Mater. Sci.*, 1995, 30, 749.
- [31] BADWAL S.P.S., DRENNAN J., *J. Mater. Sci.*, 1987, 22, 3231.
- [32] SCHOULER E.J.L., MESHABI M., VITTER G., *Solid State Ionics*, 1983, 9, 10, 989.
- [33] VERKERK M.J., MIDDELHUIS B.J., BURGRAAF A.J., *Solid State Ionics*, 1982, 6, 159.
- [34] GIBSON I.R., DRANSFIELD G.P., IRVINE J.T.S., *J. Mater. Sci.*, 1998, 33, 4297.
- [35] HAMMOUCHE A., SCHOULER E.J.L., HENAUULT M., *Solid State Ionics*, 1988, 28, 30, 1205.
- [36] TAKEDA Y., SAKADI Y., ICHIKAWA T., IMANISHI N., YAMAMOTO O., MORI M., MORI N., ABE T., *Solid State Ionics*, 1994, 72, 257.
- [37] MAURIN I., BARBOUX P., LASSAILLY Y., BOILOT J.P., *Chem. Mater.*, 1998, 10, 1727.
- [38] CARTER S., SELCUK A., CHATER R.J., KAJDA J., KILNER J.A., STEELE B.C.H., *Solid State Ionics*, 1992, 53, 56, 597.
- [39] KUO J.H., ANDERSON H.U., *J. Solid State Chemistry*, 1989, 83, 52.
- [40] LESSING P.A., *Ceramic Bulletin*, 1989, 68, 1002.
- [41] HAMMOUCHE A., SIELBERT E., HAMMOU A., *Mat. Res. Bull.*, 1989, 24, 367.
- [42] KERTESZ M., RIESS I., TANNHAUSER D.S., LANGPAGE R., ROHR F.J., *J. Solid State Chemistry*, 1982, 42, 125.
- [43] KUO J.H., ANDERSON H.U., SPARLIN D.M., *J. Solid State Chemistry*, 1990, 87, 55.
- [44] BRUGNONI C., DUCATI U., SCAGLIOTTI M., *Solid State Ionics*, 1995, 76, 177.

Photochromic hybrid sol–gel coatings: preparation, properties, and applications*

A. KLUKOWSKA¹, U. POSSET^{1**}, G. SCHOTTNER¹, M. L. WIS²,
C. SALEMI-DELVAUX^{2***}, V. MALATESTA²

¹Fraunhofer-Institut Silicatforschung (ISC), Neunerplatz 2, D-97082 Würzburg, Germany

²Great Lakes Chemical Corporation, Via Maritano 26, I-20097 San Donato Milanese, Italy

Inorganic-organic hybrid polymer (ORMOCER[®]) coatings with a fast photochromic response and high photochromic activity were prepared by incorporation of the photochromophore Variacrol[®] Blue D into hydroly-sates of organofunctional alkoxy-silanes, with subsequent thermal curing. Besides the traditional way of doping the sol–gel materials by physically dissolving the dye, a graftable derivative was prepared and covalently attached to two matrices of different rigidity. The resulting thin films showed good photochromic activity, no blooming, mechanical properties at least comparable to the pure host material, and can be applied to different glass and plastic substrates. Photochemical degradation was studied by means of artificial weathering and factors influencing the fatigue behaviour of the coatings assessed. The graftable dye showed improved photochemical fatigue resistance. The more rigid matrix was preferable, too, in terms of photodegradation.

Key words: photochromic dyes, covalent dye attachment, hybrid sol–gel materials

1. Introduction

Materials prepared via the sol–gel process [1] enable the development of abrasion-resistant, durable and optically clear coatings, that can act as hosts for organic species such as dyes [2, 3]. Inorganic-organic hybrid polymers derived from organofunctional alkoxy-silanes (ORMOCER[®]****) are especially suitable for this application [4]. Besides their alkoxy groups, that can be hydrolysed and polycondensed to form silica-like inorganic domains, these compounds provide reactive organic moieties, that

*The paper presented at the International Conference on Sol-Gel Materials, SGM 2001, Rokosowo, Poland.

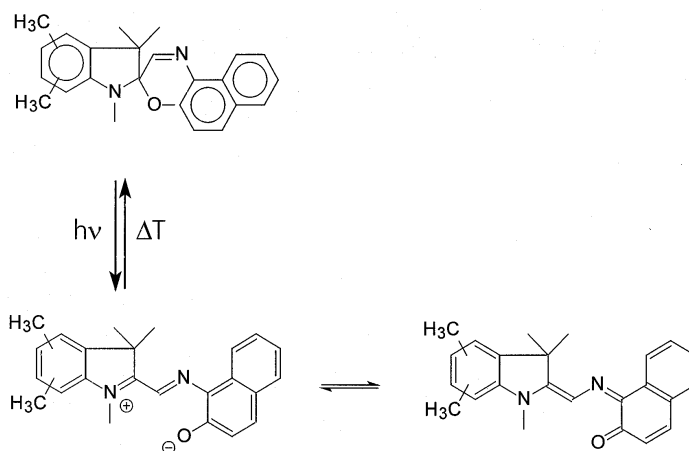
**Correspondence author, e-mail: posset@isc.fhg.de.

***EC Marie Curie Fellow, 1997–1998.

****Trademark of Fraunhofer-Gesellschaft zur Förderung der angewandten Forschung e.V., Munich, Germany.

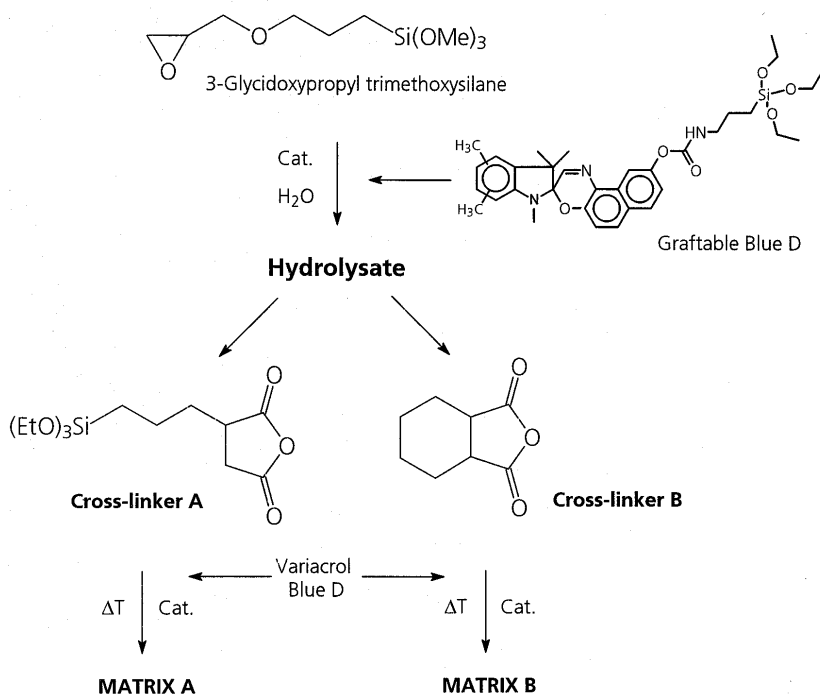
can be cross-linked to form an organic network at elevated temperatures or upon UV irradiation. By appropriate choice of network formers and modifiers the materials properties can be controlled and tailored within a certain range. Dye-doped hybrid polymers, in recent years, have been utilised to design and produce materials with new, unique properties, e. g., materials for optical storage [5] or coatings for decorative use [6].

Photochromism is defined as the reversible change between two chemical species characterized by different absorption spectra. Light of wavelength I_1 is absorbed by the usually uncoloured compound A, which gives after isomeration coloured form B, absorbing at λ_2 . B reverts back to A thermally or photochemically [7]. The most interesting group of photochromic dyes are spirooxazines, being characterized by a relatively weak $C_{\text{spiro}}-O$ bond that, upon an UV light irradiation, undergoes a heterolytic cleavage to form a planar, merocyanine-type structure (Scheme 1). The first electronic transition of such photomerocyanine usually occurs in the visible spectral region [8].



Scheme 1. Photochromic reaction of Variacrol[®] Blue D. Above: bleached spirooxazine state (colourless); below: activated, mesomeric merocyanine states (blue)

According to Crano et al. [9] an optical lens equipped with a physically dye-doped photochromic coating would be inherently limited with respect to its photochromic performance. In order to produce a coated lens with a performance acceptable to the market, the concentration of photochromic dye needs to be at least 25 wt. % of the film composition, which is impractically high. As a result, the physical and mechanical properties of the film would be significantly altered and the matrix integrity might not be maintained. Graftable dyes, with the chromophore linked to a hydrolytically unstable trialkoxysilyl group, are able to covalently attach onto the sol-gel matrix, thus present a possibility to circumvent this problem and realize higher chromophore concentrations without affecting the mechanical integrity of the coating.



Scheme 2. Coating preparation and composition

The objective of this work was to develop photochromic coatings for application on plastic substrates such as polycarbonate sunglass lenses. This should be achieved by incorporation of organic photochromophores into hydrolysates of organofunctional alkoxy silane compositions based on 3-glycidoxypropyl trimethoxysilane. Besides the traditional way of physically dissolving the dye, a graftable derivative was synthesized and subjected to the sol-gel process with the matrix material (Scheme 2). The photochromic behaviour of both dyes was investigated in two coatings of different cross-linking degree. The influence of grafting on the photophysical behaviour and fatigue resistance will be discussed.

2. Experimental section

2.1. Educts

3-Glycidoxypropyl trimethoxysilane (GLYMO), 3-triethoxysilylpropyl succinic anhydride (TESSA, cross-linker A), cis-hexahydrophthalic anhydride (HEPA, cross-linker B), and phenyl trimethoxysilane (PhTMO) were purchased from ABCR,

Wacker Chemie, Fluka, and Aldrich, respectively, and used without further purification. THF and *n*-propanol were purchased from Promochem and used as received.

The photochromic dyes Variacrol[®] Blue D and a silylated derivative thereof (hereinafter called graftable Blue D) were made available by Great Lakes Chemical Corporation. Molecular structures are given in Schemes 1 and 2.

2.2. Procedures and coating materials

Preparation of matrix A: To GLYMO placed in a round bottom flask H₂O and an amine catalyst were added in molar ratio GLYMO : H₂O : cat. = 1 : 1.5 : 0.05, and the mixture stirred. After completion of the hydrolysis as determined by Raman spectroscopy [10], *n*-PrOH (100 g per mole of GLYMO) and TESSA in molar ratio GLYMO : TESSA = 1 : 0.5 was added. After stirring for 1 h the mixture was in a ready-to-apply condition.

Preparation of matrix B: GLYMO and PhTMO in molar ratios GLYMO : PhTMO = 0.75 : 0.25 were placed in a round bottom flask and stirred. Subsequently, H₂O and an amine catalyst in molar ratio GLYMO : H₂O : cat. = 0.75 : 1.5 : 0.0375 were added and the mixture stirred until the hydrolysis was complete. Finally, *n*-PrOH (100 g per mole of GLYMO) and HEPA in molar ratio GLYMO : HEPA = 0,75 : 0,375 were added. After stirring for 1 h the sol was in a ready-to-apply condition.

The dyes were dissolved in 2:1 mixtures of THF and *n*-PrOH, in amounts corresponding to a chromophore concentration of 3 wt. % with respect to the solids content of the resulting sol. For calculation the additional mass of the silylated side chain of graftable Blue D was taken into account in order to make sure that materials with identical chromophore concentrations were investigated. Variacrol[®] Blue D was added to the final sols (as an “additive”). Graftable Blue D was added at an earlier stage in order to allow co-condensation (as shown in the Scheme 2). For the hydrolysis of the dye additional water was added in molar ratio graftable Blue D : H₂O = 1 : 1.5.

The freshly prepared systems were spin coated on different substrates such as glass slides, PC lenses or CR 39[®] sheets, and cured thermally at 130 °C for 20 min.

2.3. Test devices and measurements

Hydrolysis reactions of alkoxy silanes were followed by means of a FT-Raman spectrometer (Bruker, *model RFS 100*). Spin coating was performed by means of a KSM Karl Süss spin coater, *model RC8*. Thermal curing was done by means of Heraeus drying ovens. For activation a commercially available face tanner (Philips, *model HB170*) with Philips CLEO 15 W UV-A bulbs was used. Integrated power density was 44 W·cm⁻²·min⁻¹ between 250 and 410 nm. Bulb-sample distance was 12 cm. Transmittance spectra were measured and Δ*Y* values calculated by means of a colorimeter BYK-Gardner, model the Color Sphere. Prior to each measurement, the samples were activated, manually transferred into the measurement chamber of the

spectrometer and the spectra measured with a 2 seconds delay. An average of 10 individual measurements per sample was taken in each case.

Microhardness was determined by means of a Berkovich indenter (Fischerscope H 100). Coating thickness was measured by means of a Laser Profilometer UBM, equipped with a microfocus device. For assessment of adhesion properties, a cross hatch test according to ASTM D 3359 was performed.

Photochemical degradation was studied by means of an air cooled Suntest chamber (ATLAS Material Testing Technology BV, model Suntest CPS+) with a 1100 W Xenon lamp as a light source (according to DIN ISI 9000ff specification). The average irradiance was $750 \text{ W}\cdot\text{m}^{-2}$. After each irradiation interval all samples were subjected to a bleach-back procedure comprising heat treatment at $75 \text{ }^\circ\text{C}$ for 20 minutes, irradiation with visible light (standard fluorescence bulbs) for 1 h, followed by storage in the dark for at least 2 h.

3. Results and discussion

In order to form matrices of different rigidity, two different anhydride cross-linkers were used, i.e., the bifunctional silylated cross-linker A (to form matrix A with additional inorganic cross-linking, Scheme 2) and organic cross-linker B (to form matrix B, Scheme 2). Variacrol[®] Blue D and its graftable derivative were incorporated into both matrices with amounts corresponding to a chromophore concentration of 3 wt. %. Table 1 compiles some physical and mechanical properties of the four resulting coatings (samples 1–4), compared to the pure host materials (first two lines). The data were obtained from coatings on glass slides. The microhardness of matrix A comprising the silylated anhydride cross-linker A (81 MPa) was about twice the hardness of matrix B (39 MPa). The microhardness was taken as a measure of rigidity and residual free volume in the coating materials.

Table 1. Physical properties of coatings

Sample No.	Matrix type	Dye	Thickness/ μm	Microhardness/MPa	Photochromic activity/%
			(standard deviation in parantheses)		
	B			39.27 (0.98)	
	A			80.84 (13.18)	
1	B	3 wt. % Blue D	4.29 (0.26)	40.80 (6.26)	20
2	A		4.95 (0.25)	98.34 (5.80)	24
3	B	3 wt. % gr. Blue D	6.98 (0.38)	48.38 (5.37)	39
4	A		12.35 (0.27)	114.1 (8.01)	35

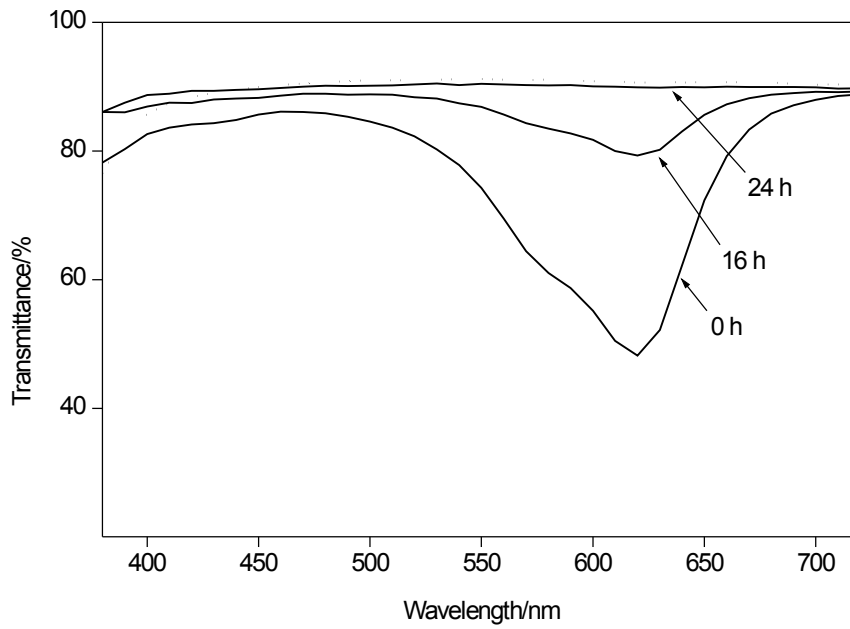


Fig. 1. Variacrol® Blue D incorporated physically into matrix B (sample 1)

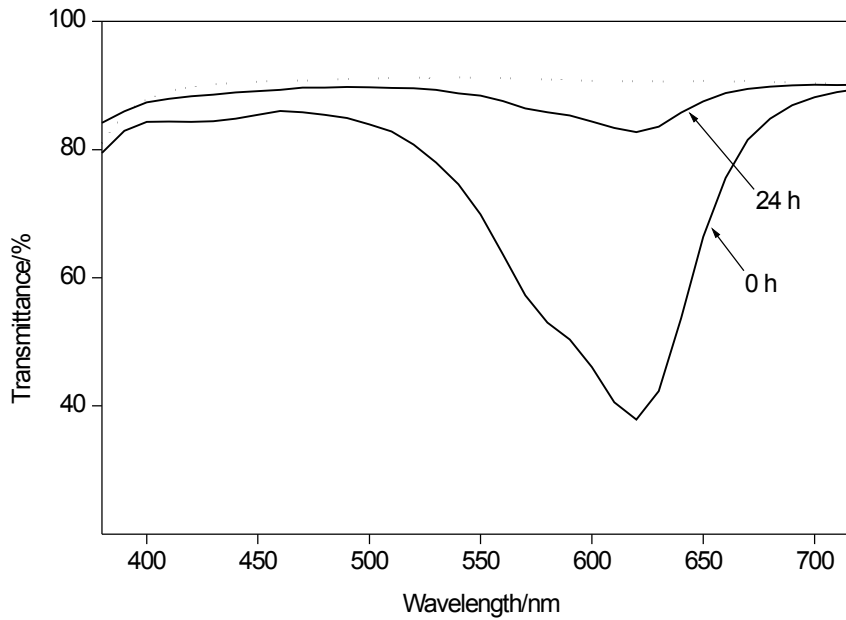


Fig. 2. Variacrol® Blue D incorporated physically into matrix A (sample 2)

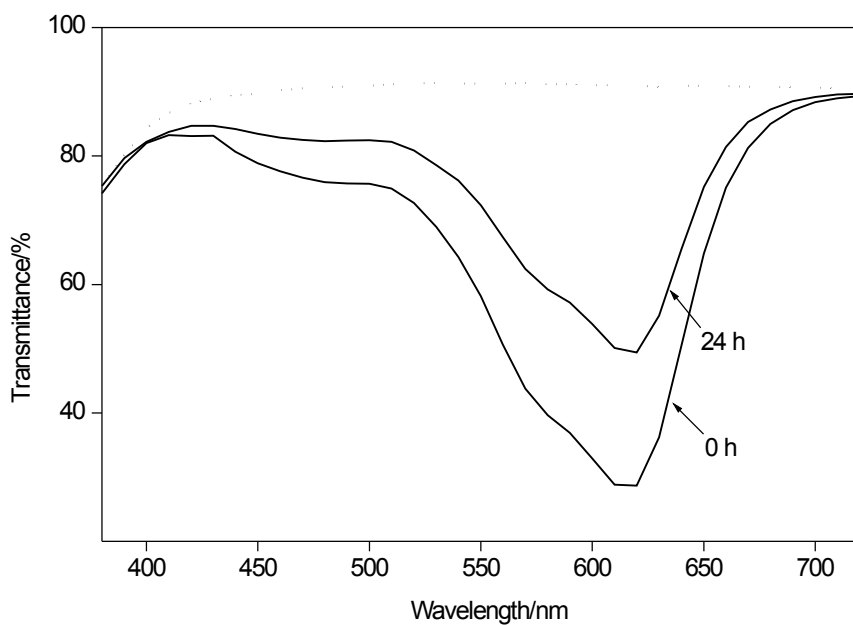


Fig. 3. Graftable Blue D covalently attached to matrix B (sample 3)

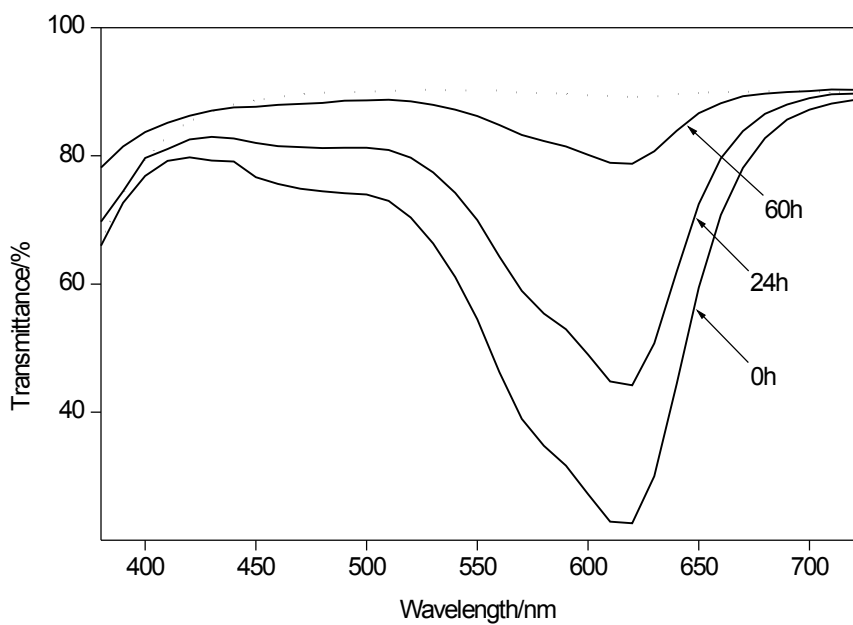


Fig. 4. Graftable Blue D covalently attached to matrix A (sample 4)

After physical incorporation of Blue D the microhardness remained essentially unchanged for sample 1, however, was slightly increased in sample 2. For the dye-grafted samples 3 and 4 the hardness rose to 48 MPa and 114 MPa, respectively. This apparent strengthening effect was attributed to the additional contribution to the matrix connectivity resulting from covalent attachment of the chromophore.

The transmittance spectra of samples 1–4 are shown in Figs. 1–4, respectively. The corresponding photochromic activities ΔY are given in Table 1. Variacrol[®] Blue D shows an absorption maximum at 620 nm in the activated state. This is in close agreement with the corresponding value obtained from alcoholic solutions [11]. The absorption of the graftable derivative was found to arise at approximately the same wavelength. Additionally, a further weak absorption was observed with a maximum at 460 nm, giving the activated form of the graftable dye a slight green hue compared to the colour of the parent dye.

Samples 3 and 4 showed higher activities compared to samples 1 and 2. However, this could not be attributed to a higher photochromic response of the grafted dye, because of the different layer thickness achieved with these samples. According to the law of Lambert–Beer, the absorbance is a function of the path length of light traversed through the sample. Normalization of ΔY to a layer thickness of 1 μm shows that all four samples had comparable activity.

The photochemical degradation (fatigue) behaviour of the coatings (on glass slides) was studied by means of artificial weathering in a Suntest device. The samples were continuously irradiated with simulated sunlight and their residual activity determined after intervals of 4 h. After each irradiation interval all samples were subjected to a bleach-back procedure in order to make sure that all photochromic species are in the bleached state prior to the transmittance measurement. Figures 1, 2 show the spectra of the physically doped samples obtained after the selected intervals. Whereas sample 1 was totally degraded after 24 h (Fig. 1) sample 2 had some residual activity after that time (Fig. 2). As both samples contained the same chromophore in identical concentrations, it can be concluded that – compared to matrix B – matrix A had a stabilizing effect on the fatigue of Blue D.

Figures 3, 4 show the spectra of the dye-grafted samples. It is apparent that the grafted dye had a strongly improved photostability. In matrix B after 24 h of irradiation still 51% of the initial activity was maintained (Fig. 3). An even better stability was observed for sample 4 where 74% and 17% of the initial activity was left after 24 and 60 h of irradiation, respectively (Fig. 4). From these data it is evident that grafting the photochromophore to a rigid, highly cross-linked host material leads to a significant photochemical stabilization, a phenomenon the occurrence of which was expected also from energy dissipation and oxygen diffusion considerations [8]. The influence of the layer thickness, which might also be significant, however, was not investigated.

The developed coatings were applied to a variety of different substrates relevant for sunglass applications, such as bis-phenol A polycarbonate, a material that has

been widely accepted to be utilized for safety-type lenses but cannot be tinted by state-of-the-art solvent dyeing techniques [9]. Bis-phenol-A polycarbonate lenses have been spin-coated with the matrix A system. In Fig. 5 are displayed photographs of the resulting photochromic samples. On the left hand side is shown the colouration of the samples immediately after switching off the UV source. The photographs on the right hand side demonstrate the status after 3 minutes of bleaching at room temperature. The shaded parts of the lenses shown here in different grey scales had a very pleasant deep blue colour. The bleached halves (covered during irradiation) were essentially colourless.

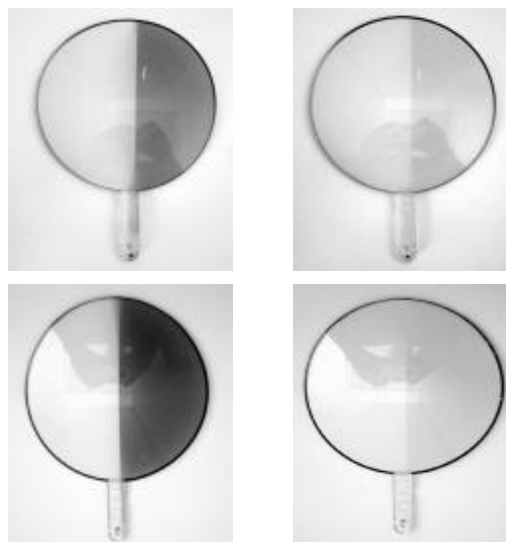


Fig. 5. Bis-phenol-A polycarbonate lenses equipped with photochromic hybrid polymer coatings. Left pictures: colouration immediately after switching off the UV-A irradiation source; right pictures: state after 3 minutes of bleaching under ambient conditions; upper row: 6 wt. % of graftable Blue D in matrix A; bottom row: 4 wt. % of graftable Blue D and 2 wt. % of Variacrol[®] Blue D in matrix A

Two different dye compositions were realized. The coating in the upper row was dyed with 6 wt. % graftable Blue D, whereas that one in the bottom row contained a mixture 2 wt. % Variacrol[®] Blue D and 4 wt. % of its graftable derivative. As the photographs prove, strong colouration depths result from these high concentrations, which, by using physically dissolved dyes only, could not have been achieved. The used grafting technique prevents aggregation, crystallisation or diffusion processes (blooming on the surface) to occur, thus, enabling higher dye concentrations to be incorporated without producing adverse effects. The switching kinetics of both dyes differed, in particular as far as the bleaching reaction is concerned, which proceeds about a factor of 10 slower for the graftable dye [12]. As can be understood from the illustration, the mixed composition (bottom row) consequently showed less residual colouration after 3 min of bleaching, although having a higher initial colouration depth. Hence, in principle, switching kinetics may be tuned in a limited range by means of mixtures of physically dissolved and grafted dyes.

4. Conclusion

Photochromic coatings with favourable mechanical and photochemical properties could be prepared from hybrid polymers and silylated graftable photochromophores. The resulting thin films exhibited a number of favourable features such as high colouration depths, absence of blooming and plasticizer effects, and improved photochemical fatigue resistance. The developed technology provides as a further benefit a more general applicability that should allow for the preparation of high-performance coatings to be used virtually independently of the substrate. The coatings may be preferably employed in the preparation of optical ophthalmic and non-ophthalmic articles such like prescription lenses or sunglasses. Besides, further possible application fields are visors, radiation protection devices, light filters, safeguard systems, sunroofs, shading devices, reversible markings, printing/publishing systems, and textiles. Where appropriate, the coatings may be equipped with abrasion resistant hybrid polymer top coats.

Acknowledgement

A. K. gratefully acknowledges the Bayerische Forschungstiftung for a scholarship. C. S.-D. thanks the European Commission for a fellowship.

References

- [1] BRINKER C.J., SCHERER G.W., *Sol-gel Science*, 1990, New York, Academic Press.
- [2] SANCHEZ C., LEBEAU B., RIBOT F., IN M., *J. Sol-gel Sci. Technol.*, 2000, 19, 31.
- [3] SCHOLZE H., *J. Non-Cryst. Solids*, 1985, 73, 699.
- [4] SANCHEZ C., RIBOT F., LEBEAU B., *J. Mater. Chem.*, 1999, 9, 35.
- [5] LEVY D., AVNIR D., *J. Phys. Chem.*, 1988, 92, 4734.
- [6] SCHOTTNER G., KRON J., DEICHMANN A., *J. Sol-gel Sci. Technol.*, 1998, 13, 183.
- [7] BROWN G.H., *Photochromism*, 1971, Wiley, New York.
- [8] MALATESTA V., *Organic Photochromic and Thermochromic Compounds*, Vol.2, J. C. Crano and R. Guglielmetti (Eds.), 1999, New York, Kluwer.
- [9] CRANO J.C., KWAK W.S., WELCH C.N., *Appl. Photochr. Polym. Syst.*, 1992, 31-79.
- [10] POSSET U., LANKERS M., KIEFER W., STEINS H., SCHOTTNER G., *Appl. Spectrosc.*, 1993, 47, 1600.
- [11] Products Catalogue, Great Lakes Chemical s.r. l., 1994, Italy, Milan.
- [12] POSSET U., SCHOTTNER G., MALATESTA V., unpublished results.

Study of thermal disordering of the $\text{KSc}(\text{WO}_4)_2$ crystal structure by Raman spectroscopy

M. MAŁCZKA¹, J. HANUZA^{1,2}, N. SIDOROV³, S. KOJIMA⁴

¹Institute of Low Temperature and Structure Research, Polish Academy of Sciences,
P.O.Box 1410, 50-590 Wrocław 2, Poland

²Department of Bioorganic Chemistry, Faculty of Industry and Economics,
Academy of Economics, Wrocław, Poland

³Institute of Chemistry, Kola Science Centre, Russian Academy of Sciences,
Apatyty, Murmansk Region, Russia

⁴Institute of Materials Science, University of Tsukuba, Ibaraki 305-8573, Japan

Raman spectra of $\text{KSc}(\text{WO}_4)_2$, exhibiting three reversible phase transitions from a trigonal phase to monoclinic and triclinic structures, have been studied in the temperature region of 100–294 K. The measurements have revealed the presence of significant broadening of librational and translational modes of the WO_4^{2-} ions with increasing temperature. This broadening was explained as a result of anisotropic activation of the complex ion reorientations.

Key words: thermal disordering, Raman spectroscopy, molecular-ionic crystals, disordered phase

1. Introduction

Crystals of binary molybdates and tungstates of alkali metals with the general formula $\text{M}^{\text{I}}\text{M}^{\text{III}}(\text{M}^{\text{VI}}\text{O}_4)_2$, where M^{I} is Na, K, Rb, Cs; $\text{M}^{\text{III}} = \text{In, Sc, Al}$; $\text{M}^{\text{VI}} = \text{Mo, W}$ belong to the type of molecular-ionic crystals. Their structure incorporates a rigid complex ion $\text{M}^{\text{VI}}\text{O}_4^{2-}$ whose atoms are mutually bonded by a covalent bond. In its turn, the $\text{M}^{\text{VI}}\text{O}_4^{2-}$ complex ion is connected with the rest of the ions of the crystalline lattice by a weaker electrostatic interaction [1]. The crystals undergo a series of the thermal phase transformations [2–11].

Many of the important characteristics of similar crystals may be determined by the state of orientational ordering as well as by translational and rotational mobility of the complex ion. Increasing the translational mobility of the $\text{M}^{\text{VI}}\text{O}_4^{2-}$ ion in the crystal lattice may result in phase transition of the displacive type. The change in orienta-

tional ordering and the rotational mobility of the complex ion is of an activation character (i.e., it requires overcoming of potential barriers) and may be accompanied by phase transitions of the order-disorder type. In this case the “melting” (activation of rotations) of rotational degrees of the complex ion freedom with temperature increase may occur stepwise, through a series of intermediate, partially disordered phases differing by various orientational ordering and the state of dynamic mobility of this ion.

The stepwise “melting” of the rotational degrees of freedom of the complex ion can be detected by the temperature dependence of Raman spectra in the low frequency region, where the librational vibrations of $M^{VI}O_4^{2-}$ are located. Disruption of the correlated vibrational movement of $M^{VI}O_4^{2-}$ ions in the crystal caused by individual, incorrectly oriented $M^{VI}O_4^{2-}$ ions or their individual reorientations of a certain type should lead to broadening, relative decrease of intensities, whereas in the limit when correlation is completely disrupted, to blurring out to the unstructured wing of the Rayleigh line of the respective lines of librational vibrations of the complex ion. The lines in the Raman spectrum pertaining to librational vibrations of the complex $M^{VI}O_4^{2-}$ ion around different axes of inertia, due to the difference in the values and temperature behaviour of orientation barriers in respect to different axes of inertia, may broaden differently and be blurred to the wing of Rayleigh line as the temperature increases [12].

The orientational disordering of the complex ion WO_4^{2-} was studied by the Raman spectra in the structure of $KSc(WO_4)_2$ crystal in the temperature interval of 100–294 K. $KSc(WO_4)_2$ is a convenient object for studying the rotational motion and orientational ordering of the complex WO_4^{2-} ion by the Raman spectra, since in the spectra of trigonal phase only internal and external vibrations of WO_4^{2-} reveal themselves. The vibrations of the K^+ and Sc^{3+} ions should not make themselves evident in the Raman spectrum since these ions occupy in the structure the positions at the centre of inversion [11, 13] and for these vibrations no change in the polarizability of the crystal unit cell occurs. In a ferroelastic phase, the situation is a little bit more complicated since the K^+ ions are no longer located at the centre of inversion and the respective vibrations become Raman-active. However, these vibrations are very weak [11].

2. Experimental

Single crystals of $KSc(WO_4)_2$ were grown by cooling of the molten mixture containing $KSc(WO_4)_2$ and solvent ($K_2W_2O_7$) in a ratio 1:1. The cooling rate was 2 K per hour. Back-scattering Raman spectra were obtained with a triple-grating spectrometer of additive dispersion (Jobin Yvon, T6400) and with a spectral resolution of 2 cm^{-1} (more experimental details can be found in our previous paper [11]).

3. Discussion

As the temperature increases, the $\text{KSc}(\text{WO}_4)_2$ crystal undergoes three reversible phase transitions $\text{P1} \leftarrow (T = 124 \text{ K}) \rightarrow \text{C2/m or C2/c} \leftarrow (T = 288 \text{ K}) \rightarrow \text{monoclinic, incommensurate} \leftarrow (T = 307 \text{ K}) \rightarrow \text{P3m1}$ [2–11], the mechanism of which remains unclear. There are grounds to believe that the phase transitions are primarily due to changes in the translational and activation rotational mobility of the WO_4^{2-} ion in relation to its axes of inertia with increasing temperature.

Raman spectra of $\text{KSc}(\text{WO}_4)_2$ have been studied in [3–5, 11]. The spectra obtained by us are shown in Figs. 1 and 2. The vibrational spectrum of this crystal can be split into two groups of lines corresponding to internal and external vibrations of the crystal lattice. Internal vibrations (valent and deformational vibrations of the complex WO_4^{2-} ion) are visible in the regions 800–1100 and 300–400 cm^{-1} , respectively. In the low-frequency region (0–60 and 60–200 cm^{-1}) the external vibrations, i.e. librational and translational vibrations of the complex ion as a whole and translational modes of K^+ ions are located. The assignment of vibrations into the discussed groups is fairly justified since the respective lines in the spectrum are separated from one another by a sufficiently large energy gap ($\sim 150 \text{ cm}^{-1}$), which points to a weak interaction of one group of vibrations with those of the other group.

It is evident from Fig. 2b that in the temperature range studied no distortion of valent bonds in the complex ion occurs, since the frequency of valent semi-symmetrical vibrations ($\nu_{\text{wo}} \sim 1010 \text{ cm}^{-1}$), characterizing the rigidity of the chemical bond W–O, does not change with temperature. In the region of deformational vibrations of the complex ion at the temperature above 250 K, more significant changes are observed: all the lines in the spectrum are noticeably widened and, moreover, the lines of frequencies ~ 350 and 370 cm^{-1} diminish in intensity (see Fig. 2a). However, only small changes in vibrational frequencies were observed herewith. Such behaviour of line parameters of valent and deformational vibrations of the complex ion may be above all caused by the activation mechanism – anisotropic reorientations of the WO_4^{2-} ion around the respective axis of inertia. Therefore, the most broadened should be the lines corresponding to the vibrations occurring perpendicular to the axes of respective reorientations. On this basis it may be assumed that reorientations of the complex ion in the crystal structure occur predominantly around the W–O axis.

The change in the reorientational motion of the WO_4^{2-} complex ion is observed clearly with the increase of temperature in the region of librational vibrations located in the low-frequency part of the spectrum. It is evident from Fig. 1 that with the increase of temperature, the librational line in the Raman spectrum broadens gradually. Such a behaviour of the line is the evidence of anisotropic activation of the complex ion reorientations in the structure of $\text{KSc}(\text{WO}_4)_2$ crystal at the 124 K temperature phase transition.

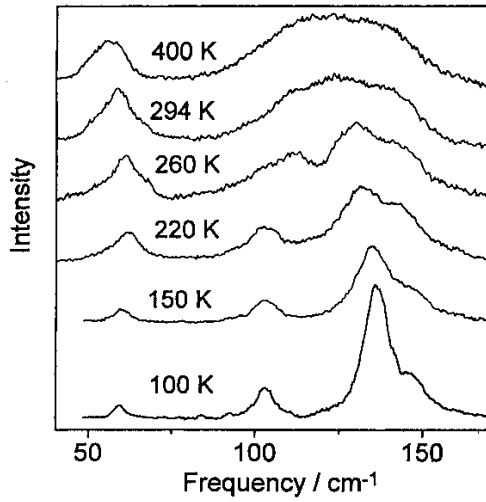


Fig. 1. Temperature-induced changes in the Raman spectrum of $\text{KSc}(\text{WO}_4)_2$ crystal in the frequency range of librational and translational vibrations of the WO_4^{2-} complex ion

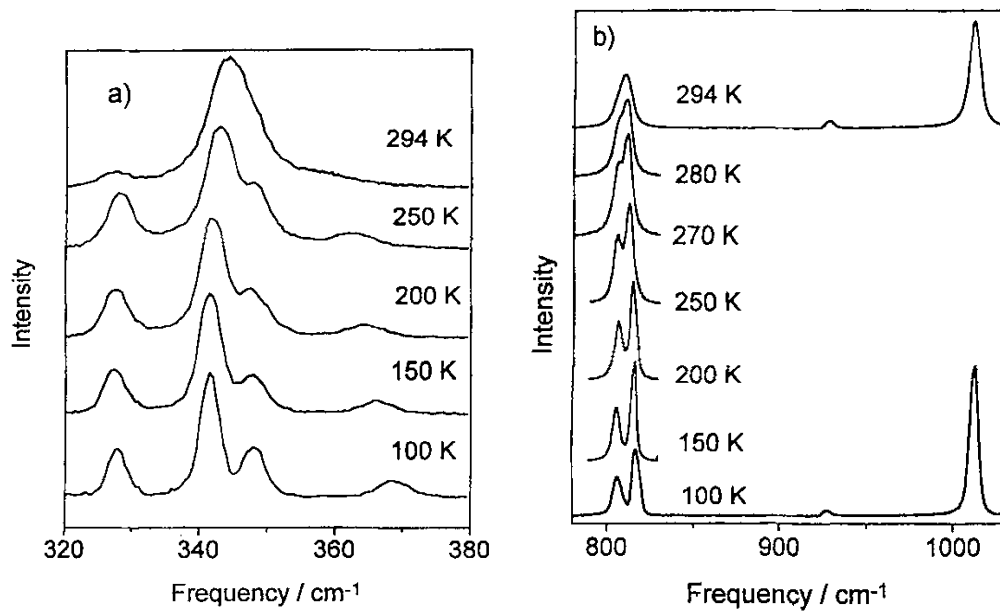


Fig. 2. Temperature-induced changes in the Raman spectrum of $\text{KSc}(\text{WO}_4)_2$ crystal in the frequency range of internal vibrations: a) the region of deformational vibrations of the complex ion, b) the region of valent vibrations of the complex ion

Reorientations of the complex ion in a phase characterized by a space group $C2/m$ ($C2/c$) are activated most likely only in respect to one of the axes of inertia whereas

for the two other axes a sufficiently ordered librational motion is observed. As the crystal temperature approaches the point of phase transition to the trigonal modification, the dynamic mobility of the complex ion is observed to grow further. Such effects of activation of structural units (molecules and their fragments) were earlier observed in Raman spectra of molecular crystals [12]. As regards the activation of anisotropic reorientations of complex ions in ionic crystals, similar effects were only observed in NMR spectra [14].

The reorientational movement of structural units in crystals results in loosening of the structure and facilitates the translational disordering of the structure and translational jumps (mobility) of structural units [12, 14]. In the Raman spectra, the effects of translational disordering of structural units are manifested in the region of translational vibrations of structural units. In molecular crystals similar effects of structural disordering are most clearly defined for the crystals formed by disc-shaped and globular molecules [12]. Thus, in the benzene crystal, with the increase of temperature the dynamic mobility of molecules in the benzene ring plane and simultaneously the translational diffusion of molecules in the directions also coinciding with the planes of the benzole rings are observed to increase [15].

It is clearly seen from Fig. 1 that increasing the temperature results in significant broadening of the translational lines of $KSc(WO_4)_2$ as well as a powerful deformation of the spectrum of translational vibrations of the complex ion, which may be a proof of enhanced translational diffusion of the WO_4^{2-} complex ions in the structure. Thus, it can be assumed that the phase transitions in $KSc(WO_4)_2$ crystal occur due to enhanced orientational and translational mobility of the complex ion in the structure with increasing temperature. In this case the activation of reorientations of the complex ion with increasing temperature occurs most likely stepwise and, in the first turn, during the phase transition occurring at 124 K.

Acknowledgements

This work was partially supported by the Foundation for Advancement of International Science. Dr. M. Maćzka acknowledges to Japan Society for the Promotion of Science for the financial support of his stay at the University of Tsukuba.

References

- [1] KLEVTSOV P. V., KLEVTOVA R.F., *Zh. Strukturn. Khim.*, 1977, 18, 419.
- [2] OTKO A.I., PELIH L.N., POVSTYANYI L.V., NESTERENKO N., *Izv. Acad. Nauk SSSR., Ser. Phys.*, 1978, 39, 697.
- [3] OTKO A.I., NESTERENKO N.M., POVSTYANYI L.V., *Phys. Status Solidi*, 1978, A46, 577.
- [4] NESTERENKO N.M., FOMIN V.I., KUTKO V.I., *Fiz. Nizk. Temp.*, 1982, 8, 862.
- [5] NESTERENKO N.M., FOMIN V.I., POPKOV YU.A., KUTKO V.I., *Fiz. Nizk. Temp.*, 1982, 8, 87.
- [6] ZAPART M.B., *Ferroelectrics*, 1992, 137, 191.
- [7] ZAPART M.B., *Ferroelectrics*, 1993, 143, 179.

- [8] ZAPART M.B., ZAPART W., *Phase Trans.*, 1993, 43, 173.
- [9] ZAPART M.B., ZAPART W., *Molecular Physics Reports*, 1994, 5, 319.
- [10] MAĆZKA M., KOJIMA S., HANUZA J., *J. Phys. Chem. Solids.*, 1998, 59, 1429.
- [11] MAĆZKA M., KOJIMA S., HANUZA J., *J. Phys. Soc. Jap.*, 1998, 68, 1948.
- [12] ZHIZHIN G.N., KRASJUKOV YU.N., MUKHTAROV E.I., ROGOVOI V.N., SIDOROV N.V., *Croatica Chemica Acta*, 1988, 61, 685; *J. Mol. Struct.*, 1990, 216, 91.
- [13] *International Tables for X-ray Crystallography*, F.M. Henry and K. Longsdale (Eds.), Birmingham, Rynoch Press, 1952, p. 564.
- [14] GABUDA S.P., PLETNEV R.N., *Primenenie NMR v Khimii Tverdogo Tela*, Ekaterinburg (Russia), 19, p. 470.
- [15] SIDOROV N. V., KRASJUKOV YU.N., MUKHTAROV E.I., *Zhur. Priklad. Spectr.*, 1999, 66, 383.

Lu₂O₃:Eu, a new X-ray phosphor

E. ZYCH¹, D. HRENIAK², W. STREK²

¹Faculty of Chemistry, University of Wrocław, 14 F. Joliot-Curie Street, 50-383 Wrocław, Poland

²Institute for Low Temperature and Structure Research, Polish Academy of Sciences, Wrocław, Poland

Five specimens of Lu₂O₃:5%Eu were prepared using various synthesis techniques. One of the samples was in the form of a plate, air-sintered at 1775 °C. Radio- and photoluminescence spectra were recorded showing emission exclusively from the ⁵D₀ level of Eu³⁺. The most intense radioluminescence, about 30% of that from standard CsI:Tl, was seen from the sintered ceramic sample. Excitation spectra suggest that some aggregation of Eu³⁺ ions take place in four of the five specimens. Some contamination of the four powdered samples with OH groups was found. Only the sintered material showing the most powerful emission was free of this problem.

Key words: X-ray phosphor, Eu-emission, ceramics

1. Introduction

When in 1895 Roentgen discovered X-ray radiation, he quickly recognized that it could serve to monitor the condition of our bones. Roentgen also quickly realized that such a use of the radiation would require using intensifying screens since the high-energy radiation is very inefficiently absorbed by photographic films. The search for materials, which could serve as converters of the X-ray radiation into visible light, much better absorbed by films, quickly resulted in finding CaWO₄ by Pupin [1]. This material is probably the best-known X-ray phosphor ever discovered. It served as a commercial phosphor for about 75 years and is still used as a very good benchmark for any new X-ray phosphor materials [2] supposing to enter the market.

We are not always aware that the technique of taking images almost did not change till now from the time when Roentgen presented an image of his wife hand bones [3]. Obviously, from that time the materials were improved and important modifications in making phosphor-film cassettes resulted in better quality images and significant radiation dosage reduction. However, last two decades showed that making a real progress and improvement in the relatively simple medical diagnostic technique would require to change the analog image recording into a digital one [4–6]. The first approach was based on utilization of storage phosphor materials. These have an abil-

ity to “remember” the radiation dosage. This information can be recovered by stimulation of the irradiated material with a red laser light [7]. The resulting emission intensity from concrete part of the phosphor gives directly information on the dosage of X-rays. Finally, a full image can be reconstructed and stored in an electronic form.

This idea was successfully realized [5] and appropriate equipment is actually commercially offered. However, this technique suffers from rather low spatial resolution of the images (lower than for the film technique) and does not seem to offer a possibility for much improvement in future.

Another idea for recording images in a digital form is in principle rather similar to the old analog procedure. The idea is to replace the film used today with a CCD camera and to substitute the phosphor layer with a new X-ray phosphor, which should be more efficient both in emission intensity and X-ray radiation absorption. In an ideal case this phosphor would be a transparent plate pixelized for better resolution of the images. Since the area covered by a CCD unit is now still not very big, such a system is first considered for dental radiography. Nevertheless, the fast progress in making bigger and of higher resolution CCD cameras convinces us that in relatively near future much larger areas could be scanned with similar systems.

The problem is that in such a system we could not use the phosphor optimized for the film technology since its emission falls in the region (blue/UV) where CCD has a relatively low sensitivity. For CCD camera the emission should appear in red or near infrared region of the spectrum. A highly desirable property of the future phosphor, for reasons mentioned above, would be the potential to fabricate it in a transparent form, as a single crystal or transparent ceramic [8–10], which are created through a proper densification of a powder.

Taking all these requirements into account we turned our attention into Lu_2O_3 . This is a very dense ($\sim 9.5 \text{ g/cm}^3$) material, which ensures a high stopping power for X-ray radiation. This, in turn, translates into the possibility of using relatively thin layers of the phosphor, which results in improvement of images quality. Furthermore, a structural and electronic analogue of lutetium oxide, Y_2O_3 , when doped with Eu or Tb is a very efficient commercially utilized phosphor. In Fig. 1 we can see how the absorption efficiency of X-ray radiation changes with its energy. In this figure we can also note that in the energy region of typical medical X-rays (20–60 keV) Lu_2O_3 does not have absorption edges. This is a very important property since it translates directly into higher-quality images. This occurs since X-ray photons of energy slightly exceeding the energy of absorption edge are often absorbed only partially in the materials and the remaining energy escapes the phosphor layer. It is a very undesirable situation causing a noticeable image degradation. Unfortunately, this problem is often totally overlooked, when the material requirements are considered. Summarizing, we can state that Lu_2O_3 possesses a set of properties, which make it potentially very attractive as a new X-ray phosphor material. In this report we will present the results of our preliminary study of this material potentials for detection of X-rays. As an activator we chose Eu^{3+} , whose emission falls within the region of high detection efficiency of CCD cameras.

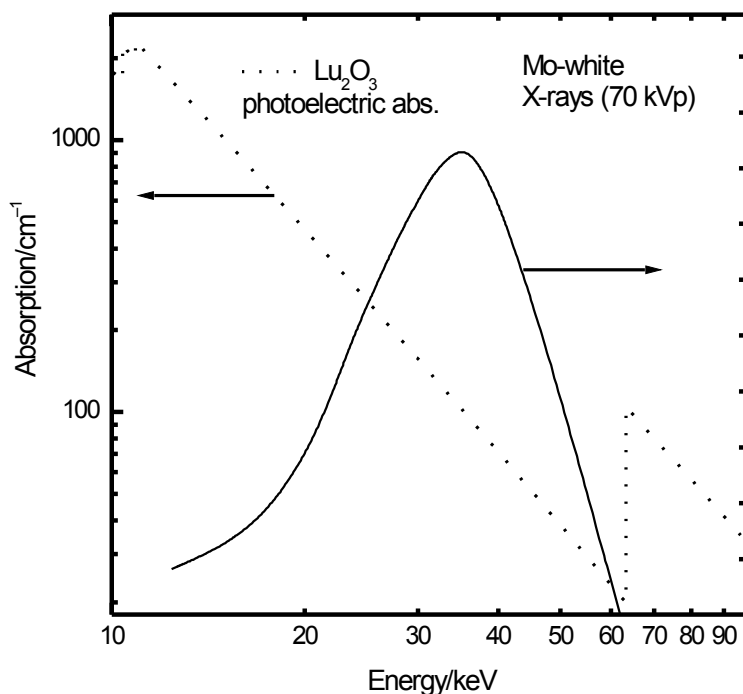
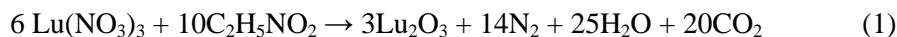


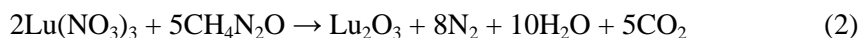
Fig. 1. Lu₂O₃ absorption coefficient for X-ray radiation in the 10–100 keV range of energy and the white X-ray radiation distribution under 70 kVp accelerating voltage

2. Materials and experiments

For our initial study we prepared five samples of Lu₂O₃:Eu containing 5% of the activator. Each of the samples was fabricated with a different synthesis technique. Sample A of the Eu-doped lutetia was formed through a thermal decomposition of (Lu_{0.95}Eu_{0.05})₂(C₂O₄)₃·nH₂O at 800 °C for 1.5 hours. The oxalate was precipitated from a water solution of Lu(NO₃)₃ and Eu(NO₃)₃ by admixing a solution of oxalate acid. Similarly, specimen B was obtained decomposing thermally NH₄Lu(C₂O₄)₂·nH₂O at 800 °C for 1.5 hours. NH₄Lu(C₂O₄)₂·nH₂O was precipitated from a solution of Lu(NO₃)₃ and Eu(NO₃)₃ by adding first NH₄OH and than H₂C₂O₄. The procedure details are given in [11, 12].

Next two samples were made using combustion synthesis. Sample C was prepared reacting Lu(NO₃)₃ mixed with appropriate amount of Eu(NO₃)₃ with glycine, NH₂CH₂COOH, in a furnace preheated up to 650 °C. In a similar manner a sample D was prepared, with the difference that now the glycine was replaced with urea, (NH₂)₂CO. These last two reactions stoichiometry may be given as follows:





In reality, unfortunately, traces of nitrogen oxides are also liberated.

Finally, sample E was made through a thermal sintering in air at 1775 °C for 10 h of the powder D, which prior to the sintering was pressed under 5 tones of load. The formed tablet was of 10 mm in diameter.

Radioluminescence spectra were recorded using white X-rays from a molybdenum X-ray tube. The X-ray maximum efficiency was about 43 keV. The emission was recorded in reflection geometry with a CCD detector coupled to a monochromator. Photoluminescence and excitation spectra were recorded using a SPF 500 Spectrofluorimeter equipped with a 300 W Xe-lamp with a sapphire window and an Al-coated parabolic reflector. Both excitation and emission monochromators were of 0.25 m focal length and $f/4$ aperture. The emission monochromator was equipped with a 1200 line/mm ruled grating blazed at 500 nm. The excitation monochromator used a 1200 line/mm holographic grating optimized for 250–300 nm. Excitation spectra were taken with a 0.3 nm resolution, and emission spectra with 0.2 nm resolution and the former were corrected for the excitation light intensity. Emission spectra were not corrected for the setup characteristic, and the sensitivity of the detection system (PMT-grating) was highest in the range of 400–750 nm. IR transmission spectra were taken with a Brüker FT IR IFS 113V Spectrometer using Merck's poly(chlorotrifluoroethylene) oil for 1400–4000 cm^{-1} energy region and mineral oil (nujol) for measurements down to 400 cm^{-1} .

3. Results

All the investigated samples were white. The samples A-D were rather loose powders, although in the case of specimen D (urea-made) a significant agglomeration was observed. From X-ray diffraction patterns of powders we could deduce that all of them were fully crystalline with varying average sizes of the crystallites as listed in Table 1. The cited sizes, confirmed also with high resolution transmission electron microscopy, were found from broadening of diffraction lines of X-ray patterns according to Scherrer's formula [13]:

$$D = \frac{\lambda}{\cos \theta \sqrt{\beta^2 - \beta_0^2}} \quad (3)$$

where D is an average crystallite size, λ denotes the X-ray radiation wavelength, β is a half-width of a diffraction line at θ and β_0 represents a scan aperture of the diffractometer. We should note that the results for samples D and E indicate that the sintering procedure stimulated significant changes in the material microstructure. Detailed analysis how the sintering parameters influence the process will be published elsewhere.

Table 1. Average sizes of the powder sample crystallites as derived from broadening of diffraction lines and relative radioluminescence intensity

Sample	A	B	C	D	E
<i>D</i> /nm	12	17	17	30	100
Relative radioluminescence intensity	~6I	~6I	~15I	I	~25I

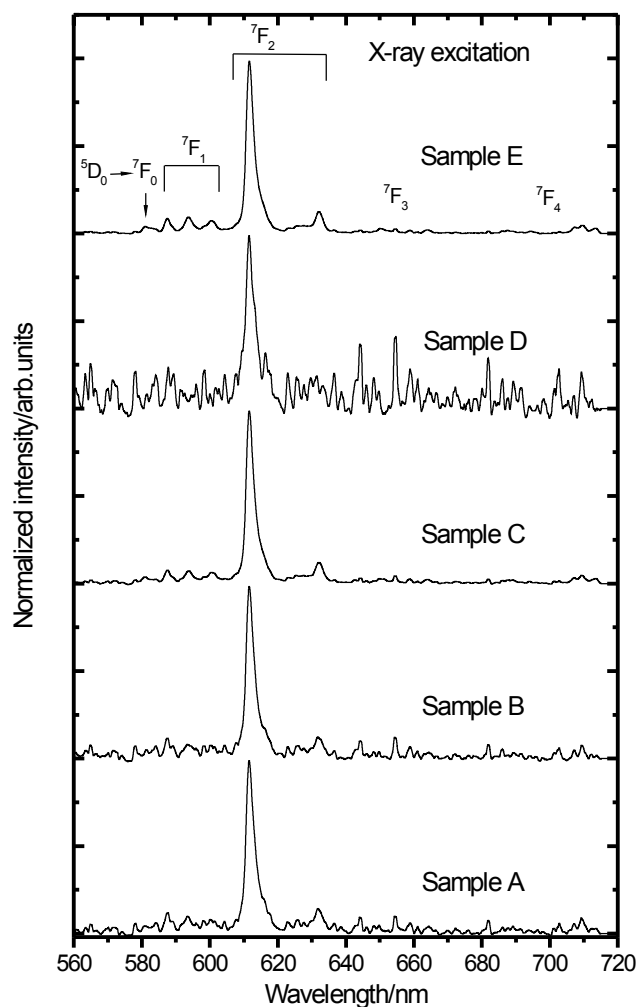


Fig. 2. Radioluminescence spectra of Lu₂O₃:5% Eu specimens prepared with various techniques

In Figure 2 we show emission spectra of all investigated specimens under excitation with X-rays. We wish to note that the radioluminescence could be seen by eye for

each of the samples, although profound variations of the intensity between specimens could be easily noted. The spectra demonstrate extensive similarities. The emissions consist of characteristic lines located within 580–720 nm, whose assignment is given in Fig. 2. The main feature appears around 611.5 nm and is related to the ${}^5D_0 \rightarrow {}^7F_2$ hypersensitive transition. This component comprises about 90% of the total emission intensity. We do not observe any significant variations in the ratios of luminescence lines intensities in different samples. What differs the spectra is mainly the observed overall emission intensity, as can be deduced even from the signal/noise ratio. The weakest luminescence is observed for the urea-made sample D. Much more efficient emissions, roughly by factor of 5–7, were observed for samples A and B. Radioluminescence from the specimen C (glycine-made) beat that from sample D (urea-made) about 12–15 times. The variations of the total emission intensity from sample to sample indicates that the light output rises with increasing crystallites size, which in turn points to the role of surface states in radioluminescence quenching. The highest efficiency we got from the sintered sample E, whose emission almost doubled that from the glycine-made powder. We compared the total emission from the best sample to that from CsI:Tl, the most efficient scintillator ever found [14, 15]. While our experimental set-up does not allow for very precise measurements of such a type, a rough comparison can be done. The estimation indicates that radioluminescence from our sintered ceramic sample E amounts about 30% of that from CsI:Tl standard. We will not overstate saying that it is more we could expect from the very first samples prepared for such experiments. This result confirms that Eu-doped Lu_2O_3 has high potentials as X-ray phosphor. Obviously, it remains to be seen to what extent this material can be optimised. Nevertheless, this results justify its further investigation.

To better understand the observed profound differences in radioluminescence intensities between the samples we performed some optical spectroscopy experiments. In Figure 3 we show emissions excited with 250 nm light from a xenon lamp. While the spectra again differ significantly in their overall intensities (by factor of about 50) they remain very similar. Positions of lines and their intensities ratios are in general the same. In fact, since the material microstructures differ substantially, we expected some changes in the appropriate line width. The smaller the crystallites, the more profound influence could be expected from the so-called surface effects. In small crystallites the near-edge-area makes-up a significant part of the grains. In this fraction of the crystallites the structure can be significantly distorted, and the defects variety and population typically increases [16, 17]. While shortly we will see some variations in spectroscopy of the materials we have to state that they do not manifest much when the 4f levels of Eu^{3+} are considered.

Neither in spectra of radioluminescence nor in optically excited emissions we can observe any traces of luminescence from the higher 5D_1 excited level. The same effect is visible for much more diluted samples [18]. This may indicate that this level falls within the conduction band of the matrix. Such submergence preserves the possibility for an emission appearance. Photoconductivity experiments would be able to explain if this speculation is true. Unfortunately, we lack an appropriate experimental set-up.

Another possible reason of such behaviour, maybe even more probable, is a fast and efficient cross-relaxation between pairs of Eu³⁺ ions. Rather high concentration of the dopant in our specimens fully justify such a supposition.

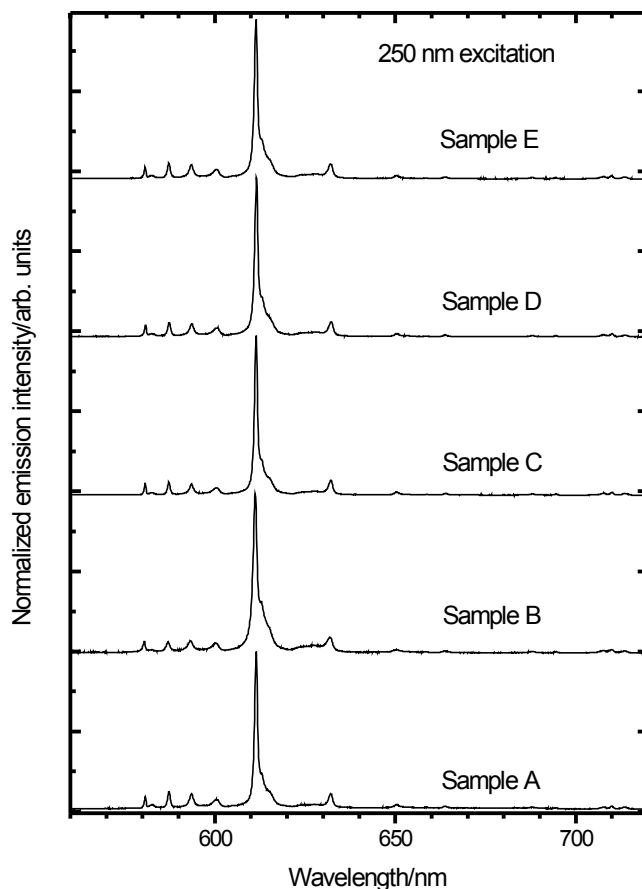


Fig. 3. 250 nm excited emission spectra of Lu₂O₃:5% Eu specimens prepared with various techniques

The X-ray and photo-excited luminescence measurements showed that the materials' emission intensities vary significantly. Partially such behaviour seems to result from the varying surface to volume ratio between samples. Indeed, we have to admit that the intensity rises regularly with increasing crystallites, as shown in Table 1. Seeking a way to better understand such behaviour, we recorded excitation spectra of the 611 nm luminescence for all specimens. They are presented in Fig. 4. While they are all similar, we can easily note considerable differences between them. The most profound disparities are related to the shape of the 250 nm band and its height related to the weaker line-type transitions seen below some 280 nm. The broad and intense

band around 250 nm is known to result from the charge-transfer transitions between O^{2-} and Eu^{3+} ions [19, 20]. The narrow lines in visible and near UV part of the spectrum reflect the intraconfigurational partially forbidden $4f \rightarrow 4f$ transitions within the Eu^{3+} ion.

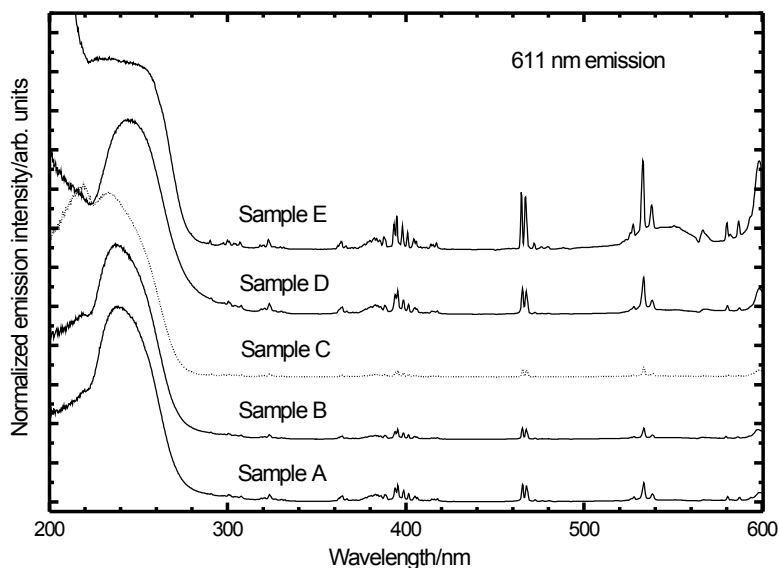


Fig. 4. Excitation spectra of the 611 nm emission of $Lu_2O_3:5\% Eu$ specimens prepared with various techniques

Only in the case of sample D the CT band is symmetric with the peak at 250 nm. In all other instances it shows a profound distortion suggesting a superposition of two bands strongly overlapping each other, thus only slightly different in energy. The shape of this band is very similar for the samples A, B, C. For all of them the band peaks at 240 nm and there is a clearly distinguishable bump around 250 nm. In the case of the specimen E this bump becomes so intense that it forms a plateau at around 230–255 nm together with the 240 nm component. This distortion may result from some aggregation of the Eu^{3+} ions. On the other hand, we could expect that such aggregation would result in a similar broadening of the $f-f$ lines, which should be the most profound for samples E. However, at room temperature such an effect is not seen and for all samples the lines width and peak positions are practically the same. When it comes to sample D, that made-up of the smallest crystallites, the CT transition forms as a very regular band, which clearly distinguishes this material from all others. This may imply that in such small particles the aggregation of Eu-ions is negligible.

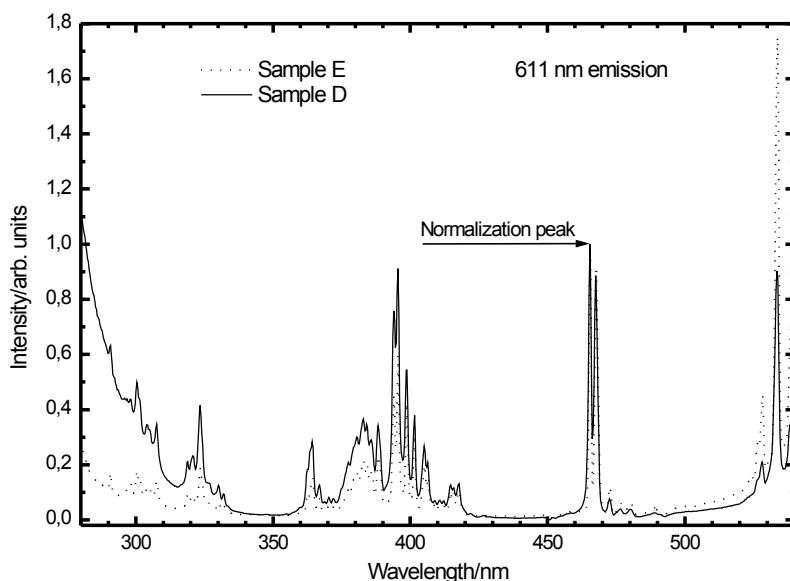


Fig. 5. Intraconfigurational transitions part of excitation spectra of the 611 nm emission of Lu₂O₃:5% Eu of the urea-made powder D and its sintered form E

Figure 5 brings into view, however, another alteration between these spectra. Namely, we clearly see that for the sintered sample E the lines situated in high-energy region are of significantly lower intensity than those in visible part when compared to the excitation spectrum of the powder D, which was a precursor for the sintered ceramic E. Clearly, this is the heating procedure, which caused this effect. Finally, in Fig. 5 we see how deeply towards longer wavelengths the tails of the CT-band extends in the case of the urea-made sample D, despite its main part, as we already stated, is clearly narrower than in sample E. Furthermore, all other powdered samples, A, B and C, behave in a way analogous to sample D. Thus we can treat this property as connected with the microstructure of the materials. The tail of the CT band extending down to about 340 nm for powders, against 280 nm for the sintered sample E, may indicate the possibility of an admixture of the CT state to the higher-lying levels of the Eu³⁺ 4f configuration additionally relaxing the selection rules. This effect seems also to say that in all powders there is some structure distortion of the materials. This should not surprise since all of the powders are created during very fast processes.

Presenting the results of radio- and photoluminescence measurements we stressed the variations in the efficiency of the resultant emissions efficiencies. We noted that the most intense luminescence was observed from specimen E, the sintered plate made of the urea-made powder D, for which on the other hand the emission was the weakest. We already noted that at least to some extent this effect mirrors the variations in surface/volume ratio. However, IR spectra presented in Fig. 6 unveil that there is another factor playing a role here. In Fig. 6 we present only the 1400–4000 cm⁻¹ part of the IR

spectra. Measurements extended down to 400 cm^{-1} indicated that the cut-off vibrations of the host material appear at 580 cm^{-1} . We used its intensity to normalize the spectra in the region above 1400 cm^{-1} . Such a low value of the cut-off vibrations makes the possibility of luminescence quenching through a phonon-assisted non-radiative relaxation of rather a little probability. Thus also from this point of view the Lu_2O_3 host appears to be a valuable luminophore lattice.

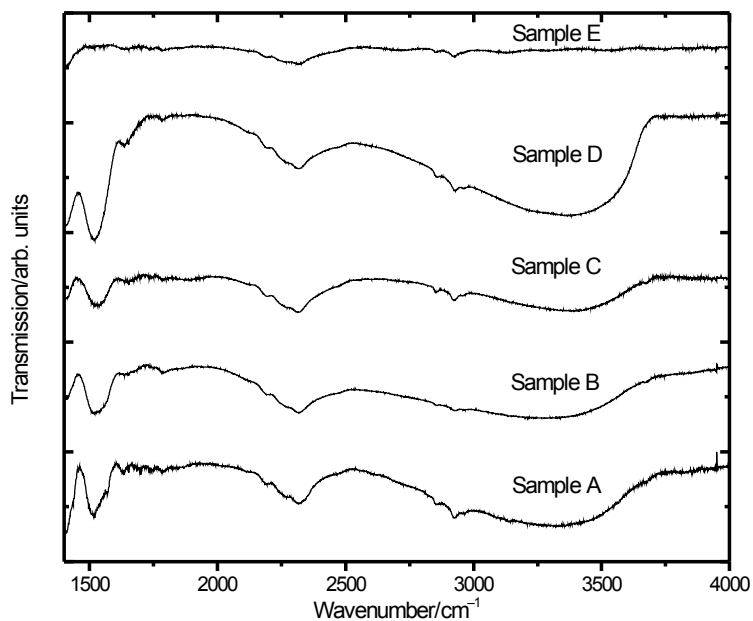


Fig. 6. Infrared spectra of the $\text{Lu}_2\text{O}_3:5\% \text{ Eu}$ specimens prepared with various techniques

The IR spectra presented in Fig. 6 indicate that in most of the investigated samples some contamination with OH groups is present. This we must conclude from the presence of the characteristic broad band located at around $3000\text{--}3500\text{ cm}^{-1}$ and a narrower one at $1500\text{--}1600\text{ cm}^{-1}$. These vibrations are observed for all of the powders A, B, C and D. Only the sintered specimen E do not show any traces of such features, which cannot surprise since the material was made at $1775\text{ }^\circ\text{C}$. Analysing the IR spectra, we can note that the contamination of powders vary from sample to sample, being highest for the urea-made specimen D. Samples A, B and C seem to be contaminated at a roughly similar level.

Obviously, the presence of such high-frequency vibrations in the materials as introduced by the OH groups is very undesirable since they may easily diminish the luminescence efficiency making non-radiative relaxation much more probable. As is well known, vibrations of 3500 cm^{-1} frequency are able to quench luminescence if the gap between levels does not exceed at least 4–5 times this value. In Eu^{3+} the gaps

under considerations are significantly smaller [19, 20]. This is not to say that especially under X-ray excitation we do not have additional problems diminishing the overall radioluminescence efficiency. The influence of the increasing surface/volume ratio we already stated. Nevertheless, the OH groups have to be removed from the samples to reduce the possibility of quenching the luminescence of the excited Eu³⁺ ions. The results indicate that independently of the synthesis technique all the materials will require to be heat-treated at relatively high temperatures to get rid of the OH groups.

4. Conclusions

In this report we showed that Eu-doped Lu₂O₃ appears to be a very interesting material for X-ray radiation detection. The lutetia host is characterized by a very efficient absorption of the medical X-rays, which is very important requirement in many applications. Since lutetia unit cell is cubic, it may be converted into transparent ceramic plates through application of a proper densification technique. This is important possibility for some medical diagnosis techniques. We found that doping the material with Eu³⁺ allows for making a pretty efficient X-ray phosphor. All our powders suffered from some contamination with OH groups. Only an air-sintered specimen was free from such a problem and this specimen exhibited the highest emission both under UV light excitation and X-ray stimulation. The estimated emission efficiency of this material was about 30% of the standard CsI:Tl. Such a result from a material, which was in neither way optimized as an X-ray phosphor, has to be treated as very encouraging. It certainly justifies broader and more thorough research on this material. Optimization of a material performance may be an indeed time-consuming process. We are convinced, however, that the results presented in this report fully justify undertaking of such a work.

Acknowledgements

The authors thank Dr. C. Brecher and A. Lempicki (RMD Inc. Watertown, and Alem Associates, Boston, MA) for helpful discussions. Support from Polish Committee for Scientific Research, KBN, under Grant No. 3 T09B 031 16, and from NATO under Grant No. PST.CLG.976212 is gratefully acknowledged.

References

- [1] BUSHONG S.C., *Radiologic Science for Technologists*, C. V. Mosby (Ed.), USA, St. Louis MO, 1975.
- [2] BRIXNER L. H., *Mater. Chem. Phys.*, 1987, 16, 253.
- [3] ROENTGEN W.C., *Ann. Phys. Chem.*, 1898, 64, 1.
- [4] BRAEGGER U. et al., *Computer Assisted Densitometric Image Analysis (CADIA) for the Assessment of Alveolar Bone Density Changes in Furcations*, *J. Clin. Periodontol.*, 1989, 16.

- [5] MIYAHARA J., *Chem.Today*, 1989, 223, 29.
- [6] ACKERMAN J.B. et al., *Digital, Diagnostic, and Treatment Probe*, New York, J. Dent., 1986, 56.
- [7] TAKAHASHI K., KOHDA K., MIYAHARA J., KANEMITSU Y., AMITANI K., SHIONOYA S., *J. Lumin.*, 1984, 31&32, 266–268.
- [8] RHODES W.H., *J. Am. Ceram. Soc.*, 1981, 64, 13.
- [9] WEI G.C., PASCUCCI M.R., TRICKETT E.A., BRECHER C.W., RHODES H., *SPIE Proc.*, 1988, 968, 5.
- [10] IKESUE A., KINOSHITA T., *J. Am. Ceram. Soc.*, 1995, 78, 1033.
- [11] MINAGAWA Y., YAJIMA F., *Bull. Chem. Soc. Jpn.*, 1990, 63 (2), 378–382.
- [12] MINAGAWA Y., YAJIMA F., *Bull. Chem. Soc. Jpn.*, 1990, 63 (7), 2115–2117.
- [13] KLUG P., ALEXANDER L. E., *X-ray Diffraction Procedure*, 1954, New York, Wiley, Chap. 9.
- [14] HAHN B., *Phys. Rev.*, 1953, 91, 772–773.
- [15] SAKAI E., *IEEE Trans. Nucl. Sci.*, 1987, 34, 418–422.
- [16] KINGERY W.D., *J. Amer. Ceram. Soc.*, 1974, 57, 1.
- [17] see, e. g., KINGERY W.D., BOWEN H.K., UHLMANN D.R., *Introduction to Ceramics*, 2nd Ed., 1976, New York, Wiley.
- [18] ZYCH E., HRENIAK D., STREK W., to be published.
- [19] BLASSE G., *Prog. Solid St. Chem.*, 1988, 18, 79–171.
- [20] BLASSE G., GRABMEIER B.C., *Luminescent Materials*, 1994, Springer-Verlag, Berlin.

Review of luminescence and magnetic properties of antiferromagnetic KMnCl_3 , RbMnCl_3 , TlMnCl_3 and $(\text{C}_n\text{H}_{2n+1}\text{NH}_3)_2\text{MnCl}_4$ ($n = 1, 2$)

MAŁGORZATA PAWŁOWSKA, WALTER WOJCIECHOWSKI

Institute of Inorganic Chemistry and Metallurgy of Rare Elements,
Wrocław University of Technology, Wrocław, Poland

Phenomena connected with the energy transfer in perovskite-type antiferromagnetic materials KMnCl_3 , RbMnCl_3 , TlMnCl_3 and $(\text{C}_n\text{H}_{2n+1}\text{NH}_3)_2\text{MnCl}_4$ ($n = 1, 2$) doped with Sm^{3+} and Eu^{3+} ions, are considered and discussed in this paper. The energy transfer in the compounds studied is proved to depend upon the magnetic interactions in them.

1. Introduction

The title compounds belong to a group of magnetically ordered insulating materials. A consequence of their condensed nature is the possibility of excitation energy transfer. This effect dominates the luminescence and absorption behaviour of magnetically coupled manganese salts. In this paper, we present a review of luminescence and magnetic studies of chloromanganates of different crystal structures and magnetic properties of different dimensionalities. All investigated compounds have the perovskite structure which can be simply described as two- or three-dimensional array of $[\text{MnCl}_6]$ octahedra.

KMnCl_3 has the structure distorted from the ideal cubic perovskite (orthorhombic structure), space group P_{nma} , unit cell parameters: $a = 7.08$, $b = 9.97$, $c = 6.98$ Å, $Z = 4$ (α -phase). This compound manifests an interesting feature of crystallographic polytypism at room temperature, namely, it can simultaneously exist in another orthorhombic crystallographic phase isostructural with KCdCl_3 , space group P_{nma} , unit cell parameters: $a = 8.79$, $b = 3.883$, $c = 14.42$ Å, $Z = 4$ (β -phase). Mn^{2+} is located in the centre of Cl^- octahedra slightly distorted in case of α -phase and heavily in case of β -phase. Both phases are paramagnetic at room temperature and undergo a transition to a magnetically ordered state: α -phase at about 100 K and β -phase at about 2.1 K.

TiMnCl₃ has cubic perovskite structure at 293 K, space group P_{n3m} (α -phase) lattice constant 5.025 Å, which can transfer into another nonperovskite KCdCl₃ structure with space group P_{n3m} and cell parameters: $a = 8.93$, $b = 3.84$, $c = 14.77$ Å. The ideal perovskite structure shows structural phase transition caused by tetragonal and rhombic distortion at 296, 276 and 235 K. Below the last low-temperature transition down to the temperature of liquid nitrogen, the crystal has a monoclinic unit cell. Neel temperature for TiMnCl₃ is about 113 K.

RbMnCl₃ crystallises in a hexagonal space group $P_{6/mmc}$. Neel temperature is 96 K. No structural transition has been found for this compound.

KMnCl₃, TiMnCl₃ and RbMnCl₃ are 3D Heisenberg antiferromagnets.

$(C_nH_{2n+1}NH_3)MnCl_4$ are perovskite layer compounds and possess two-dimensional magnetic properties. This two-dimensional character is further enhanced in the case of antiferromagnetic alignment of spins within a Mn²⁺ plane. T_N for both compounds investigated are about 43 K. Magnetic properties were reported in details in our previous paper [1].

We investigated pure crystals and crystals doped with Eu³⁺ and Sm³⁺ ions, concentration of lanthanide ions was of the order of 1 wt.%. Figure 1 represents the relevant energy levels of Mn²⁺, Eu³⁺ and Sm³⁺ and reveals the possibility of resonance of manganese emission levels and the lanthanide ions absorption levels. We could monitor intrinsic manganese, host and trap emission. Energy transfer process could occur between these spectroscopic centres.

The crystal preparation, details about experimental conditions and results were reported in our previous papers [1–8]. In this report, structures, magnetic and spectroscopic properties of the title compounds are summarised and correlated.

2. Manganese(II) luminescence and absorption

Manganese(II) compounds have particularly attracted the interest of spectroscopists. Mn²⁺ ions excited by the absorption of light into higher excited states, rapidly relax to the lowest ⁴T_{lg} excited state. This is a metastable level, its lifetime is about 30 msec. All d-d transitions are spin- and parity-forbidden but due to the first prohibition they are susceptible to exchange effects. Because of strong Mn–Mn exchange coupling a particular ion do not remain excited, but the excitation energy migrates through the crystal. Excitation transfer, luminescence and absorption are experimentally accessible and can be correctly described by exciton model.

Figure 2 shows a representative absorption spectrum of the compounds investigated. The number and position of the bands are characteristic of octahedry coordinated divalent manganese ions. All those compounds exhibit broad-band luminescence between 14000 cm⁻¹ and 19000 cm⁻¹, which strongly depends on temperature, kind of univalent cation and lattice crystal structure. Temperature dependence is mainly associated with additional energy levels induced by lattice defects and impurities, acting as traps for excitation energy. These traps can be divalent transition-metal

ions with low-energy electronic states, such as Fe^{2+} , Co^{2+} , Ni^{2+} , Ca^{2+} , which are unintentionally but inevitably present in trace amounts even in a nominally pure crystal. Consequently, intrinsic emission of regular manganese ion as well as host and trap emission of slightly perturbed manganese sites are observed.

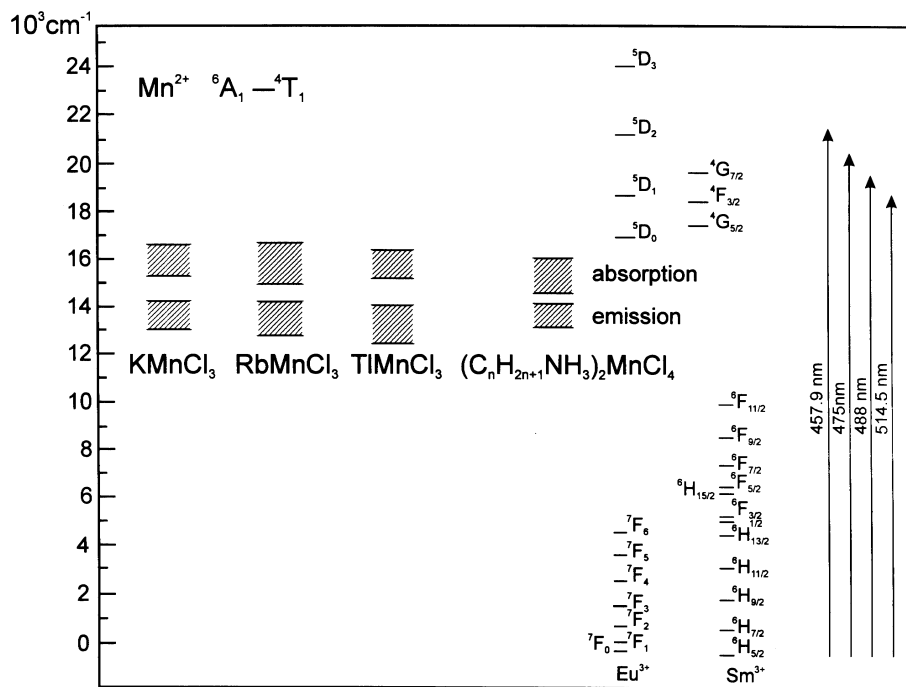


Fig. 1. Relevant energy levels of Mn^{2+} , Eu^{3+} and Sm^{3+}

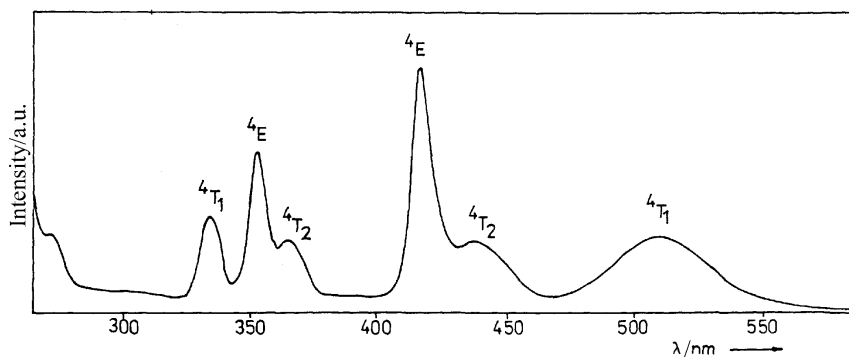


Fig. 2. Absorption spectrum of KMnCl_3 at RT

In fluoromanganates energy transfer process occurs at low temperature, so hardly any intrinsic luminescence is observed. This process becomes more efficient when

temperature increases and simultaneously deeper traps are fed. This is the reason for red shift of luminescence spectrum at higher temperature. Some of the traps decay radiatively (host or lanthanide acceptor traps), some are quenching traps. Presence of quenching traps is likely to be responsible for decreasing of the Mn^{2+} donors luminescence intensity at high temperatures. On the subject of energy transfer in fluoromanganates there exist a large body of literature, but there are only few concerning chloromanganates.

Kambli and Güdel [9] investigated antiferromagnets: RbMnCl_3 , CsMnCl_3 , CsMnBr_3 and Rb_2MnCl_4 doped with Er^{3+} and Nd^{3+} . Emission intensity and time-resolved spectra were measured at different temperatures. The conclusion was that the absence of energy transfer at low temperature is observed for alkalichloromanganates in general. They claim that energy transfer becomes efficient above 50 K.

Our results of Eu^{3+} and Sm^{3+} -doped KMnCl_3 , RbMnCl_3 , TlMnCl_3 luminescence confirm the above feature of chloromanganates, however weak lanthanide fluorescence was also observed at low temperature (see Fig. 3), hence energy transfer cannot be excluded in low-temperature range.

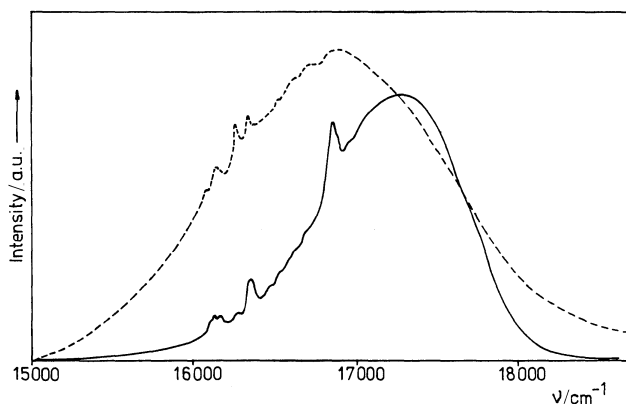


Fig. 3. Luminescence spectrum of Eu^{3+} doped β -phase KMnCl_3 at 4.2 K. Dotted line – continuous flow cryostat, full line – stationary cryostat

There is one more effect that could not be explained if we assumed the temperature 50 K to be a critical one for energy transfer process. This is an effect of blue shift of the Mn^{2+} luminescence maximum in chloro-compounds with increasing temperature. It was observed to be of the order of $500\text{--}700\text{ cm}^{-1}$ for KMnCl_3 , RbMnCl_3 , TlMnCl_3 (see Figs. 4, 5) by us and Kambli and Güdel [10] for RbMnCl_3 . The most probable reason for this shift can be thermal back transfer at high temperature. If it is the case we cannot say that energy transfer is negligible at low temperature.

The luminescence spectra of $(\text{CH}_3\text{NH}_3)_2\text{MnCl}_4$ and $(\text{C}_2\text{H}_5\text{NH}_3)_2\text{MnCl}_4$ doped with Nd^{3+} and Eu^{3+} ions were also investigated. A broad-band Mn^{2+} luminescence maximum at $\sim 16500\text{ cm}^{-1}$ at 77 K and at 17100 cm^{-1} at room temperature was observed. Lanthanide ions fluorescence was not detected.

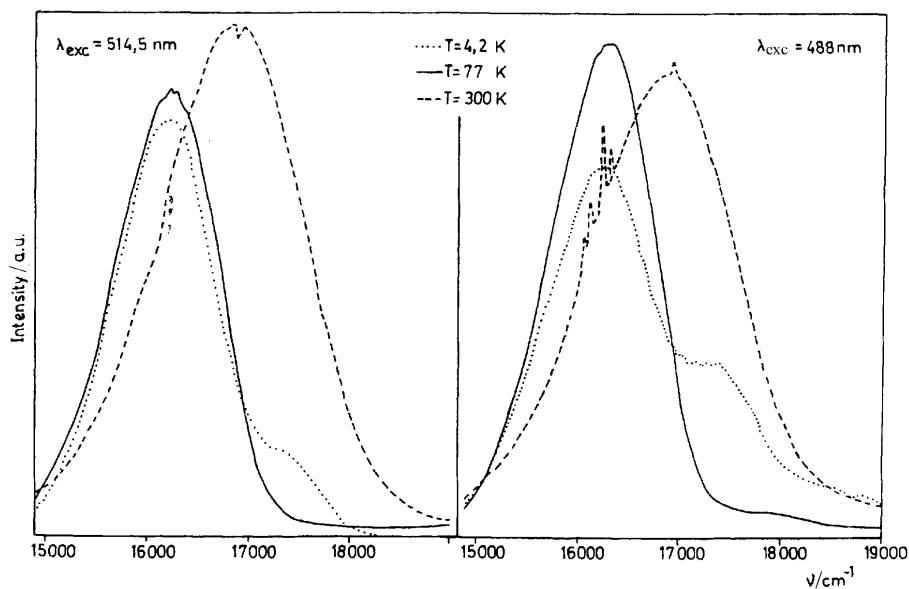


Fig. 4. Luminescence spectra of Eu^{3+} doped $\alpha + \beta$ -phase KMnCl_3 at selected temperatures

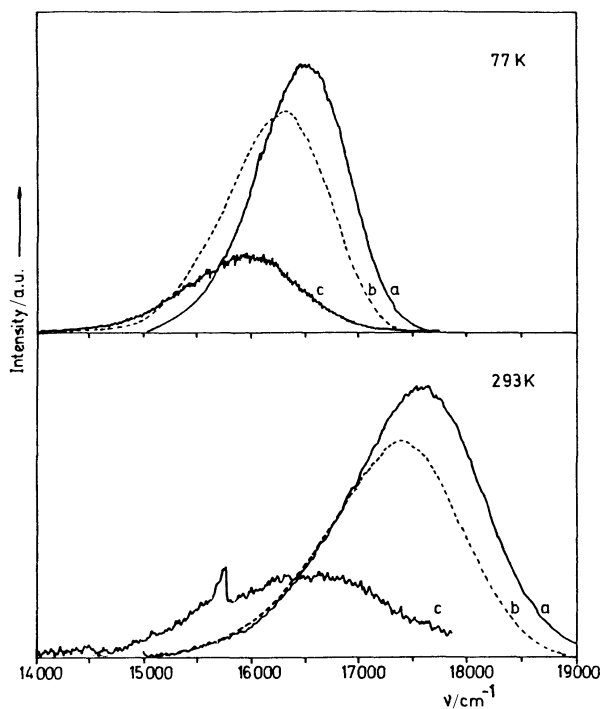


Fig. 5. Luminescence spectra of Eu^{3+} doped TiMnCl_3 :
a) α -phase, b) $\alpha + \beta$ -phase, c) β -phase

3. Crystal structure and luminescence characteristic

The KMnCl_3 crystal occurs in two crystallographic phases [11]: the orthorhombic perovskite structure – α -phase, and the non-perovskite orthorhombic structure – β -phase. The α -phase is not stable and transforms slowly into β -phase, so in practice two different phases may exist in the KMnCl_3 crystal. In Fig. 6 the difference between luminescence spectra of α -phase and β -phase is visible. α -phase emission is observed at 15700 cm^{-1} (635 nm) while this for $\text{Mn}^{2+} \ ^4\text{T}_1 \rightarrow \ ^6\text{A}_1$ transition in β -phase lies in the region of significantly higher energy – 17540 cm^{-1} (570 nm). α -phase emission is strong at 77 K while the emission corresponding to β -phase is rapidly quenched when temperature increases to 77 K (Fig. 4).

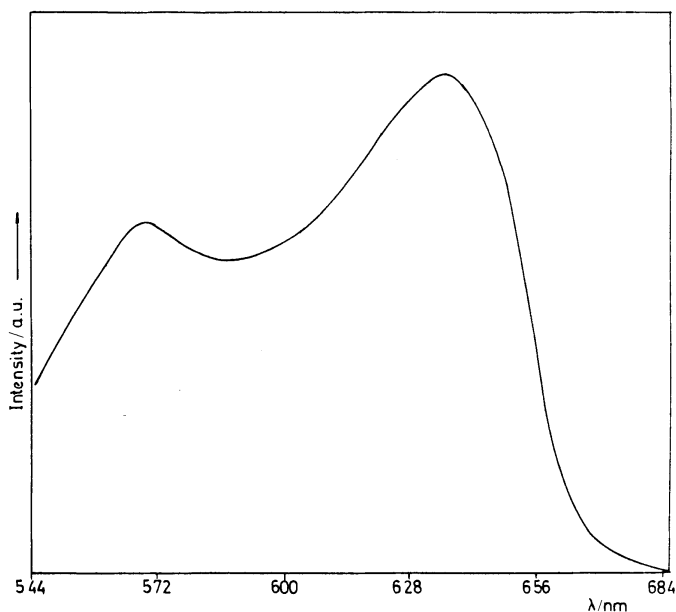


Fig. 6. Luminescence spectrum of KMnCl_3 containing α and β crystal phases at 13 K

In TiMnCl_3 the dependence of Mn^{2+} luminescence on crystal structure was also observed. We investigated the cubic crystal (α -phase) and orthorhombic (β -phase). The emission maximum in luminescence spectra shifts to the red when the symmetry of the crystal lowers (Fig. 5).

In crystals in which a phase transition occurs, an anomalous luminescence can be observed [7, 11]. Figure 7 presents an evident thermal hysteresis loop of the luminescence lifetime measured at luminescence maximum corresponding to α -phase of KMnCl_3 crystal. This effect was not observed for β -phase emission.

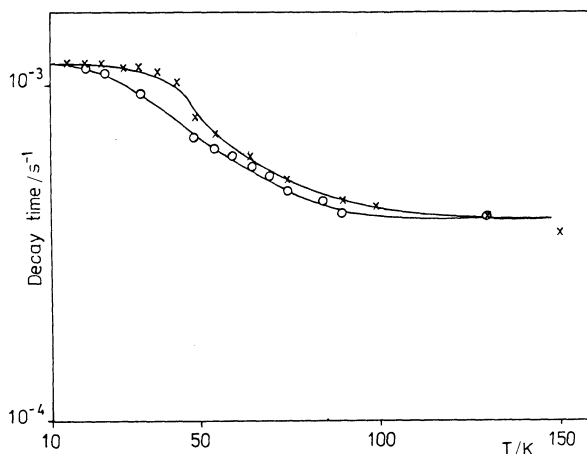


Fig. 7. Temperature dependence of the luminescence lifetimes corresponding to β -phase luminescence of α - + β - KMnCl_3 (635 nm). The points marked by \times and \circ were measured for increasing and decreasing temperature, respectively

Another consequence of the structural transitions in this crystal is an interesting dependence of luminescence spectra on the cooling rate of the crystal (Fig. 3). The luminescence spectra of Eu^{3+} doped KMnCl_3 crystal for some not closer defined reason depended on cooling rate at 4.2 and 77 K, namely, the spectrum of Mn^{2+} salt placed in a stationary cryostat (rapid cooling) is shifted to the blue by about 400 cm^{-1} in comparison to the spectrum measured in a continuous-flow cryostat (slow cooling); this phenomenon was reversible at LN temperature.

Among the three investigated 3D crystals, KMnCl_3 and TlMnCl_3 are susceptible to structure transitions. The polytypism and temperature phase transitions significantly influence the luminescence spectra. So the crystal structure should be confirmed for each particular luminescence spectrum. According to our knowledge, no structural changes have been observed for RbMnCl_3 , so spectroscopy results are synonymous.

4. Trivalent lanthanide ions emission and energy transfer

The investigations of lanthanide ions' luminescence were carried out in such a way that the excitation was only due to energy transfer. The spectra were excited with the argon laser lines: 457.9 nm, 475.5 nm, 488 nm, 514.5 nm. The energy corresponding to these wavelength does not fit the absorption levels of europium and samarium ions (Fig. 1) so direct excitation was negligible. Furthermore, the intensity of lanthanide ions luminescence was of orders of magnitude too high for direct excitation of ions characterized by very small absorption coefficient in low concentrations. Energy transfer could be responsible for excitation of fluorescence of Sm^{3+} and Eu^{3+} ions incorporated into chloromanganates(II) matrices. Figure 8 is a nice illustration of

the feeding mechanism of Sm^{3+} emission by long-range and short-range energy transfer from the Mn^{2+} system. Our spectral data [3, 5, 6] and those of other authors [9, 12] give evidence for thermal activation of this process. Efficiency of energy transfer process to lanthanide ions does not only depend on temperature but also on crystal structure and experimental conditions.

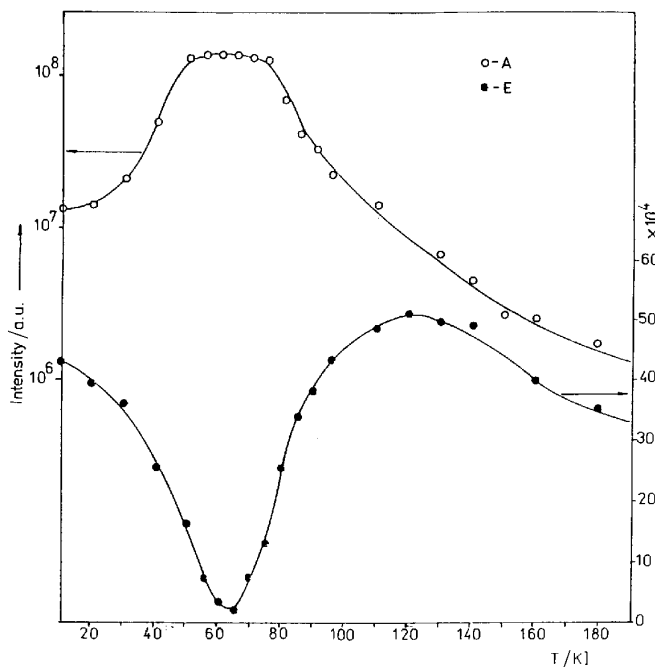


Fig. 8. Temperature dependence of the integrated intensities of ${}^4T_1 \text{Mn}^{2+}$ emission (curve A) and of ${}^4G \text{Sm}^{3+}$ (curve E) for Sm^{3+} -doped RbMnCl_3

Among the investigated salts we have not detected any rare earth emission in case of $(\text{C}_n\text{H}_{2n+1}\text{NH}_3)_2\text{MnCl}_4$ and hardly any in case of TlMnCl_3 . The most effective luminescence centre were created in rubidium and potassium chloromanganates II.

In Figure 4, the luminescence spectra of Eu^{3+} doped KMnCl_3 at the temperature of 4.2, 77 and 293 K are presented. The europium luminescence was observed only at room temperature. It consists of single sharp lines at $\sim 16900 \text{ cm}^{-1}$ assigned to ${}^5D_0 \rightarrow {}^7F_1$ transition, and of the group of lines of lower energy than that assigned to ${}^5D_0 \rightarrow {}^7F_2$ transition. Note that when 514.5 nm line was used as an excitation source, no Eu^{3+} fluorescence was observed but instead of it the characteristic reabsorption of the ${}^7F_1 \rightarrow {}^5D_0$ transition resulting from Mn-Eu interaction appeared at the top of Mn^{2+} luminescence broad band. For β -phase KMnCl_3 europium luminescence was observed at 4.2 K and 77 K (Fig. 9) Eu^{3+} exhibited several intense sharp multiples. The transitions from the 5D_0 to the 7F_2 , 7F_1 , 7F_0 states were observed around 17300, 16900 and

16200 cm^{-1} , respectively. This fine structure in the europium emission spectrum is the result of both electronic and vibronic effects.

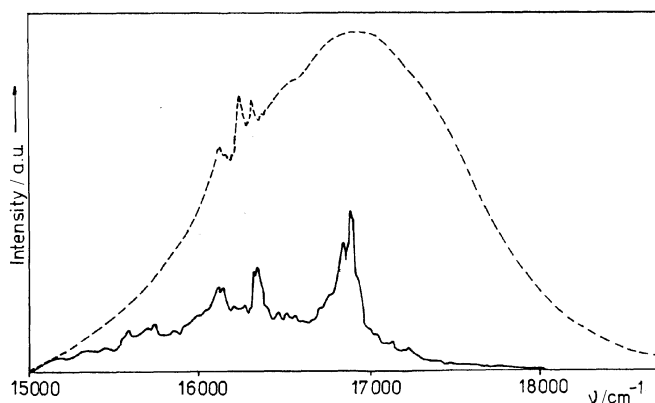


Fig. 9. Luminescence spectrum of Eu^{3+} -doped β -phase KMnCl_3 at 77 K. Dotted line – continuous flow cryostat, full line – stationary cryostat

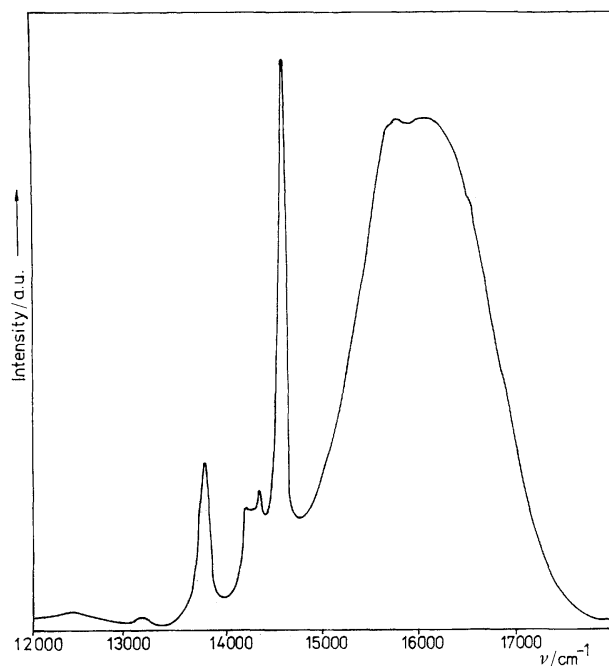


Fig. 10. Luminescence spectrum of Sm^{3+} -doped RbMnCl_3 at 130 K

Sm^{3+} fluorescence in Sm^{3+} -doped RbMnCl_3 was experimentally accessible at the whole temperature range of 10–180 K. The representative spectrum is presented in

Fig. 10. The Sm^{3+} emission originating from the metastable state ${}^4\text{G}_{5/2}$ was observed. In the measured range of $12000\text{--}19000\text{ cm}^{-1}$ at least five bands ${}^4\text{G}_{5/2} \rightarrow {}^6\text{H}_{5/2 \text{ to } 13/2}$ should be observed. In practice, only two bands ${}^4\text{G}_{5/2} \rightarrow {}^6\text{H}_{13/2}$ and ${}^4\text{G}_{5/2} \rightarrow {}^6\text{H}_{11/2}$ located in the range of $12400\text{--}13000\text{ cm}^{-1}$ and $14200\text{--}14600\text{ cm}^{-1}$, respectively, were observed. According to the Judd–Ofelt theory [13, 14], ${}^4\text{G}_{5/2} \rightarrow {}^6\text{H}_{11/2}$ transition should be more intensive than ${}^4\text{G}_{5/2} \rightarrow {}^6\text{H}_{13/2}$ transition as shown in the table for the $\langle U(\lambda) \rangle$ coefficients [15]. Lack of transitions ${}^4\text{G}_{5/2} \rightarrow {}^6\text{H}_{5/2,7/2,9/2}$ located in the range from 15800 to 18000 cm^{-1} of the spectrum may be elucidated by the strong non-radiative energy transfer $\text{Sm}^{3+} \rightarrow \text{Mn}^{2+}$, since these transitions well match with the absorption band ${}^6\text{A}_1 \rightarrow {}^4\text{T}_1$ (Fig 1).

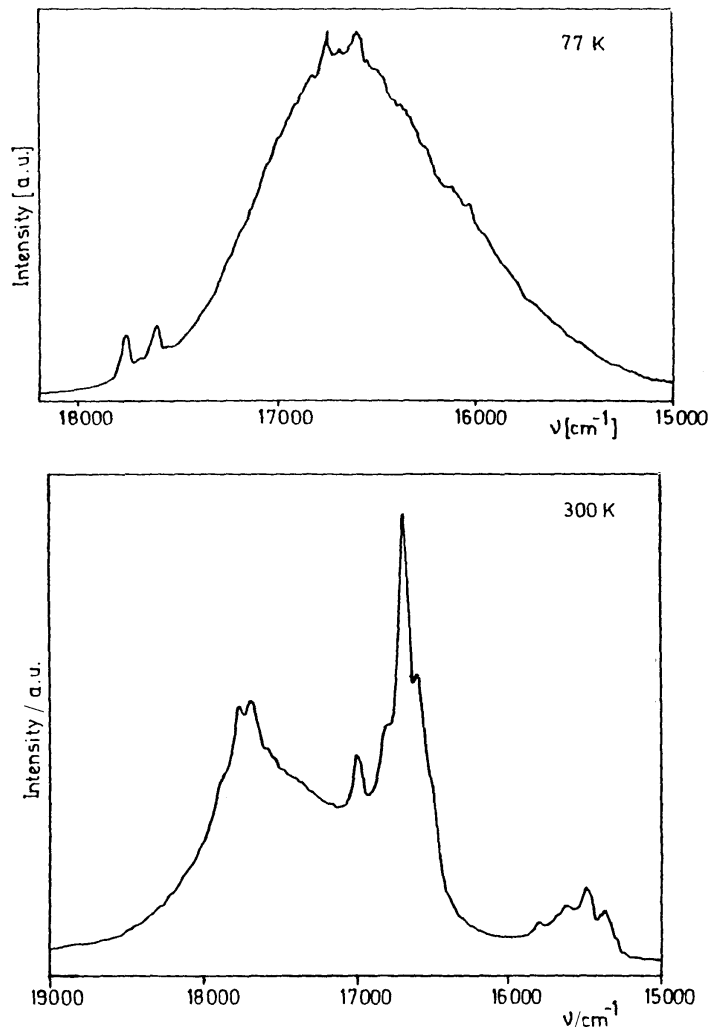


Fig. 11. Luminescence spectra of Sm^{3+} -doped KMnCl_3

Sm³⁺-doped KMnCl₃ emission was observed at 77 K and 300 K in the range of 15360–17880 cm⁻¹ (Fig. 11). It was assigned to ⁴G_{3/2} → ⁶H_{7/2}, ⁶H_{9/2}, ⁶H_{11/2} and ⁴G_{5/2} → ⁶H_{5/2}, ⁶H_{7/2}, ⁶H_{9/2}. The intensity of Sm³⁺ luminescence was stronger at RT than in LN temperature. This can be associated with the blue shift of manganese luminescence maximum from 16700 cm⁻¹ at LN temperature to 17800 cm⁻¹ at RT, and hence better overlapping of Mn²⁺ levels with Sm³⁺ ⁴G levels.

Lanthanide ions in chloromanganate(II) matrices can be excited via long-range or short-range energy transfer. Short-range means direct energy transfer to earth ions traps from neighbouring Mn²⁺ ions. Long-range transfer takes place when excitation migrates through the host lattice. In such a case the transfer rate increases exponentially with increasing temperature; this relationship is described by an empirical activation law:

$$k_{\text{ET}}(T) = (k_{\text{ET}})_{T \rightarrow \infty} e^{-\Delta/kT}$$

where k is the Boltzmann constant, Δ is activation energy for energy transfer. The activation energy calculated from experimental data such as intensity and decay time was of the order of several hundreds cm⁻¹, and related temperature at which energy transfer becomes the most efficient process was about 50 K. This common characteristics of all chloromanganates system was confirmed by us and other authors. If the lanthanide ions luminescence is observed below 50 K it may be due to short-range energy transfer from Mn²⁺ to Eu³⁺ or Sm³⁺. This effect seems to be characteristic of particular crystals and it depends on the structure, monovalent cations and on experimental conditions.

Next to structure and temperature also experimental conditions were found to influence lanthanide ions fluorescence. In Figs. 3 and 9 there are presented the spectra of Eu³⁺-doped β-KMnCl₃ crystal placed in a continuous flow cryostat as well as in a stationary cryostat. The difference between these two experiments consisted in the cooling rate of samples; slow in continuous flow cryostat and rapid in a stationary one. Eu³⁺ fluorescence was much more intensive when the crystal reached quickly the temperature of 77 K.

5. Magnetic properties and luminescence of Mn(II)

The most likely mechanism for excitation transfer in Mn²⁺ compounds with forbidden d-d transitions, is an exchange mechanism. On the other hand, exchange interaction in the ground state generate antiferromagnetic order. Consequently, some relationship between magnetic properties and energy transfer characteristic could be expected.

In the very first investigations [16, 17] these materials distinguished themselves by extensive changes in the fluorescence characteristics below the magnetic ordering temperature. It was suggested that magnetic ordering provides a source of local lattice

distortion around the excited ion which, in turn, gives rise to changes in the fluorescence characteristics; intensity and fluorescence maxima below ordering temperature.

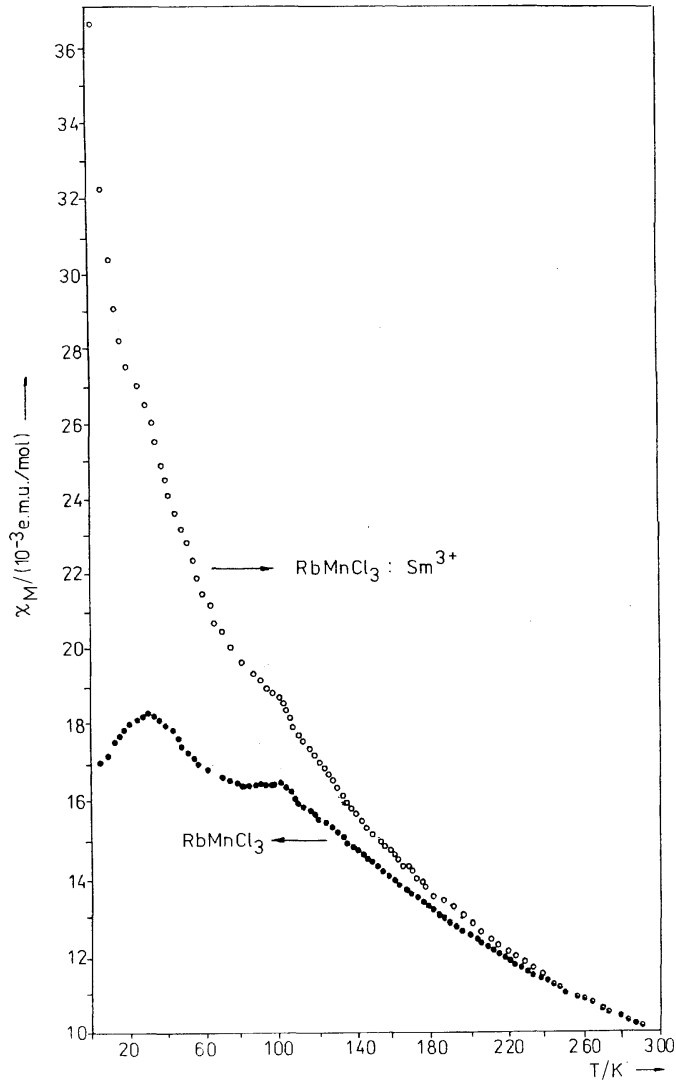


Fig. 12. Magnetic susceptibility χ_M temperature for RbMnCl_3 and Sm^{3+} -doped RbMnCl_3

Specific energy transfer characteristics were observed for low- and high-dimensional antiferromagnets. In high dimensional MnF_3 , and alkali metal fluoromanganates(II) KMnF_3 [18], RbMnF_3 [19] and CsMnF_3 [20] energy transfer is very efficient down to 4.2 K. As a consequence the intrinsic emission is almost not observed. In linear chain compounds (1D): TMMC [21], CsMnBr_3 [22], $\text{CsMnCl}_3 \cdot 2\text{H}_2\text{O}$ [23] energy migrates along the chain and the process – indeed one-dimensional – be-

comes efficient at the temperature above 50 K, so the emission from regular manganese(II) centres dominates the luminescence spectra at low temperature. The layer-structured NaMnCl_3 [24] and Rb_2MnCl_4 [25] behave as quasi 2D antiferromagnets and represent an intermediate case.

We investigated magnetic properties of RbMnCl_3 [2]. The temperature dependence of the magnetic susceptibility for this crystal and the crystal doped with Sm^{3+} is presented in Fig. 12. The maximum at about 100 K represents transition to long-range antiferromagnetic order in RbMnCl_3 . The anomaly at approximately 30 K may be connected with another phase transition or only be a mark of the onset of short-range ordering. Magnetic properties of the rubidium chloromanganate crystal doped with Sm^{3+} ion are different, however, this difference does not manifest itself in structural properties. X-ray data [2] shows that both crystals crystallise in a hexagonal system.

Spectroscopic properties of RbMnCl_3 have been systematically studied by Kambli and Güdel [10] and two characteristic temperatures for luminescence decay time: ~ 30 K and ~ 100 K were distinguished, which match well with two characteristic temperatures 30 and 96 K of magnetic transitions shown in Fig. 12.

In the undoped and weakly doped samples of RbMnCl_3 the decay curves of the Mn^{2+} emission are exponential within experimental error [9]. This is not the case of crystal with lanthanide ions' concentration higher than 1%. Traces of samarium ions cause changes in luminescence characteristic, e.g. the temperatures 30 and 96 K are not characteristic of the temperature dependence of Mn^{2+} luminescence intensity. They also influence the magnetic properties of the crystal.

The dimensionality of the crystal lattice seems to be of minor importance in the luminescence mechanism. We tried to monitor the trap emission in two-dimensional layer compounds $(\text{C}_n\text{H}_{2n+1}\text{NH}_3)_2\text{MnCl}_4$ ($n = 1, 2$) doped with Nd, Eu and Sm ions and no lanthanide ions emission was observed. Other low-dimensional manganese compounds such as Rb_2MnCl_4 , CsMnBr_3 were reported to be an efficient matrix for incorporation luminescence centre of lanthanide ions [9]. Among 3D Heisenberg antiferromagnets in RE doped TlMnCl_3 hardly any lanthanide ions luminescence was observed [8] in opposite to RE doped KMnCl_3 and RbMnCl_3 [3, 4] which produce intense rare earth emission indicating an excitation via effective energy transfer.

References

- [1] PAWŁOWSKA M., WOJCIECHOWSKI W., Phys. Stat. Sol.(a), 1991, 127, K125.
- [2] PAWŁOWSKA M., WOJCIECHOWSKI W., Bull. Acad. Pol. Sci., 1982, 30, 1–12, 63.
- [3] PAWŁOWSKA M., STRĘK W., JEŻOWSKA-TRZEBIATOWSKA B., WOJCIECHOWSKI W., Proc. Inter. Symp. on Rare Earth Spec., 454, Published World Sci., Singapore, 1984.
- [4] PAWŁOWSKA M., BRONOWSKA W., WOJCIECHOWSKI W., Phys. Stat. Sol. (b), 1988, 146, K51.
- [5] PAWŁOWSKA M., STRĘK W., TRABJERG I., Phys. Stat. Sol. (b), 1989, 154, K89.
- [6] PAWŁOWSKA M., STRĘK W., DEREŃ P., J. Sol. State Chem., 1989, 79, 282.
- [7] PAWŁOWSKA M., STRĘK W., TRABJERG I., Phys. Stat. Sol. (a), 1991, 124, K63.
- [8] PAWŁOWSKA M., ŁUKOWIAK E., STRĘK W., TRABJERG I., Phys. Stat.Sol.(a), 1993, 137, K53.
- [9] KAMBLI U., GUDEL H.U., Inorg.Chem., 1984, 23, 3479.

- [10] KAMBLI U., GUDEL H.U., J. Phys., C: Sol. State. Phys., 1984, 17, 4041.
- [11] HOROWITZ M., MAKOWSKY J., BEN DOR L., KALMAN Z.H., J. Sol. State Chem., 1982, 43, 107.
- [12] MORITA M., SEI T., AKASAKA R., MACHII H., SHIBA A., SHOKI T., NARUTOMI S. TSUMBOMARA T., J. Lumin., 1990, 45, 156.
- [13] MCPHERSON G.L., TALLITO K., AUERBACH R.A., Sol. State. Com., 1982, 43, 817.
- [14] JUDD B.R., Phys. Rev., 1962, 127, 750.
- [15] OFELT G.S., J. Chem. Phys., 1962, 37, 511.
- [16] LARNALL W.T., CROSSWHITE H., CROSSWHITE H.M., *Energy Level Structures and Transitions Probabilities of the Trivalent Lanthanide in LaF₃*, Argonne National Laboratory, undated.
- [17] HOLLOWAY W.W., Jr., KESTIGIAN M., NEWMAN R., PROHOFSKY E.U.I., Phys. Rev. Lett., 1963, 11, 82.
- [18] HOLLOWAY W.W., Jr., KESTIGIAN M., Phys. Lett., 1969, 29A, 709.
- [19] WILSON B.A., YEN W.M., HEGARTY J., IMBUSCH G.F., Phys. Rev. B, Condens. Matter., 1979, 19, 4238.
- [20] IVERSON M.V., SIBLEY W.A., Phys. Rev. B, Condens Matter, 1980, 21, 2522.
- [21] MANCORGE R., JACQUIER B., MADEJ C., BLANCHARD M., BRUNEL I.C., J. Phys.(Orsay, Fr.), 1982, 43, 1267.
- [22] YAMAMOTO H., MCCLURE D.S., MARZZACCO C., WALDMAN M., Chem. Phys., 1977, 22, 79.
- [23] MCPHERSON G.L., FRANCIS A.H., Phys. Rev. Lett., 1981, 41, 1681.
- [24] MCPHERSON G.L., WILLARD S.C., Chem. Phys. Lett., 1981, 78, 135.
- [25] KAMBLI U., GUDEL H.U., BRIAT B., J. Phys. C: Sol. State Phys., 1984, 17, 3113.

Effects of polarization of radiofrequency radiation in polycrystalline ESR

V.E. FAINZILBERG

Department of Chemistry, Long Island University, USA

ESR spectrum of polycrystalline samples exposed to radiofrequency radiation of circular polarization is calculated and examined. The spectrum is compared with ESR spectrum generated by commonly used oscillating magnetic field of linear polarization. Differences of contours at linear and circular polarizations provide additional opportunity for correlation of theory and experiment, and determination of ESR parameters.

Key words: ESR spectrum, polycrystalline samples, circular polarization

1. Introduction

Radiofrequency radiation, commonly used in ESR experiments, is linearly polarized. Utilization of a circular-polarized radiofrequency radiation is essential in some cases, when the sign of gyromagnetic ratio may reveal the nature of the ground state. It permits also to determine the signs of g -tensor components in the systems with ground state described as an effective spin level [1–3]. Multiple experiments and calculations of line shapes of mono- and polycrystalline ESR spectra have exclusively been carried out with linear-polarized radiation (see, e.g., [4–8]). Indeed, any linear-polarized radiation is a superposition of two circular components that revolve in opposite directions, and hence, while one of them may be silent, the other one is absorbed. We aim to show that polycrystalline spectrum in linear-polarized radiation has different line shape than that obtained in a circular polarization. The latter provides additional data to compare and validate theoretical models. In this paper, the theory of polycrystalline ESR spectra that are generated by a resonance absorption of a circularly polarized radiofrequency radiation are examined.

2. Transition operator of a circularly polarized radiation

Operator of Zeeman interaction of a paramagnetic center (effective spin, s) with an oscillating magnetic field \mathbf{B} is written as [1–5]:

$$\mathbf{V} = -b\hat{s}g\mathbf{B}$$

where b and g are Bohr's magneton and g -tensor, respectively (here and further a circumflex above letter indicates the operator and/or tensor). Omitting constant multiplier $b\mathbf{B}$ we obtain the transition operator in the form of:

$$\hat{V} = \hat{s}^\dagger \hat{g} \mathbf{e} \quad (1)$$

where polarization vector $\mathbf{e} = \tilde{\mathbf{B}}/\tilde{B}$ defines the orientation of an oscillating magnetic field.

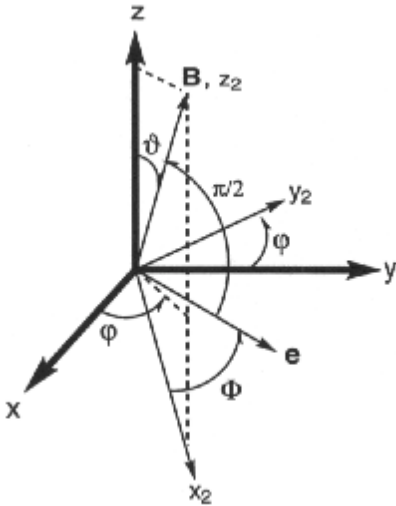


Fig. 1. Orientation of external constant magnetic field \mathbf{B} and polarization vector \mathbf{e} of oscillating magnetic field in the co-ordinate system, x, y, z of an individual paramagnetic center

Usually, in ESR spectrometers, the oscillating magnetic field (either linear-, or circular-polarized) is localized in the plane perpendicular to the external constant magnetic field \mathbf{B} .

Consider system x, y, z of an individual paramagnetic center (Fig. 1). The orientation of the external field \mathbf{B} is chosen along z_2 -axis, while x_2y_2 -plane accommodates the polarization vector \mathbf{e} of the oscillating radiation. Co-ordinate system $x_2y_2z_2$ can be obtained from the system of an individual center xyz by two successive rotations, namely: (1) right-handed rotation around z -axis by an angle j to obtain intermediate system, $x_1y_1(z_1 \equiv z)$:

$$\begin{pmatrix} x_1 \\ y_1 \\ z_1 \end{pmatrix} = \hat{u} \cdot \begin{pmatrix} x \\ y \\ z \end{pmatrix} \equiv \begin{pmatrix} \cos j & \sin j & 0 \\ \sin j & \cos j & 0 \\ 0 & 0 & 1 \end{pmatrix} \cdot \begin{pmatrix} x \\ y \\ z \end{pmatrix}$$

followed by (2) right-handed rotation around newly formed y_1 -axis by an angle J :

$$\begin{pmatrix} x_2 \\ y_2 \\ z_2 \end{pmatrix} = \hat{u}_J \cdot \begin{pmatrix} x_1 \\ y_1 \\ z_1 \end{pmatrix} \equiv \begin{pmatrix} \cos J & 0 & -\sin J \\ 0 & 1 & 0 \\ \sin J & 0 & \cos J \end{pmatrix} \cdot \begin{pmatrix} x_1 \\ y_1 \\ z_1 \end{pmatrix}$$

where x_j , y_j , and z_j assume components of an arbitrary vector written in each of coordinate systems. The relationship between components of the vector in two coordinate systems is given by [9, 10]:

$$\begin{pmatrix} x_2 \\ y_2 \\ z_2 \end{pmatrix} = \hat{u} \cdot \begin{pmatrix} x \\ y \\ z \end{pmatrix}$$

where

$$\hat{u} = \hat{u}_J \cdot \hat{u}_j \equiv \begin{pmatrix} \cos J \cos j & \cos J \sin j & \sin J \\ -\sin j & \cos j & 0 \\ \sin J \cos j & \sin J \sin j & \cos J \end{pmatrix} \quad (2)$$

The immediate orientation of polarization vector \mathbf{e} in the system, x_2, y_2, z_2 is defined as (see Fig. 1):

$$e_{x_2} = \frac{\tilde{B}_{x_2}}{\tilde{B}} \equiv \cos \Phi, \quad e_{y_2} = \frac{\tilde{B}_{y_2}}{\tilde{B}} \equiv \sin \Phi, \quad \text{and} \quad e_{z_2} = \frac{\tilde{B}_{z_2}}{\tilde{B}} \equiv 0$$

Thus, the polarization vector in the x, y, z -system is obtained as

$$(0 \leq J \leq \pi, \quad 0 \leq j \leq 2\pi, \quad 0 \leq \Phi \leq 2\pi):$$

$$\begin{pmatrix} e_x \\ e_y \\ e_z \end{pmatrix} = \hat{u}^{-1} \cdot \begin{pmatrix} \cos \Phi \\ \sin \Phi \\ 0 \end{pmatrix}, \quad \Leftrightarrow \quad \begin{cases} e_x = \cos J \cos j \cos \Phi - \sin j \sin \Phi \\ e_y = \cos J \sin j \cos \Phi - \cos j \sin \Phi \\ e_z = -\sin J \cos \Phi \end{cases} \quad (3)$$

In the case of axial anisotropy the \mathbf{g} -tensor is diagonal with: $g_{xx} = g_{yy} \equiv g_{\perp}$ and $g_{zz} \equiv g_{\parallel}$. In the cyclic basis [11, 12], $x_0 = z$, $x_{\pm} = \mathbf{m}^{1/\sqrt{2}}(x \pm iy)$, the transition operator has a simple form, and in the case of a linear polarization we obtain the a well-known expression [13]:

$$\begin{aligned}
\hat{V}_{\text{lin}} &= -g_{\parallel} e_0 \hat{s}_0 + g_{\perp} (e_+ \hat{s}_- + e_- \hat{s}_+) \\
&\equiv g_{\parallel} \sin J \cos \Phi \hat{s}_0 + \frac{1}{\sqrt{2}} g_{\perp} \left[(\cos J \cos \Phi - i \sin \Phi) e^{-ij} \hat{s}_+ \right. \\
&\quad \left. - (\cos J \cos \Phi + i \sin \Phi) e^{ij} \hat{s}_- \right]
\end{aligned} \tag{4}$$

where \hat{s}_+ and \hat{s}_- are commonly known raising and lowering spin operators, respectively.

General case of an elliptically-polarized radiation [15, 16] is given by a complex polarization vector: $\mathbf{e} = \mathbf{e}_1 \pm i\mathbf{e}_2$. In a particular case of $1/2\mathbf{e}_1/2 = 1/2\mathbf{e}_2/2$, and $\mathbf{e}_1 \perp \mathbf{e}_2$, elliptically-polarized radiation is reduced to a right-handed: $\mathbf{e}_+ = \mathbf{e}_x + i\mathbf{e}_y$, and left-handed: $\mathbf{e}_- = \mathbf{e}_x - i\mathbf{e}_y$, circular-polarized radiations. Hence, the transition operator of interaction with a circular-polarized oscillating field related to x_2, y_2, z_2 -system is given by:

$$\hat{V}_{\text{cir}}^{\pm} = \hat{\mathbf{m}}_{\mathbf{m}} e_{\pm} \equiv -\mathbf{m}_{\mathbf{m}} e^{\pm i\Phi} \equiv -\frac{1}{\sqrt{2}} (\hat{\mathbf{m}}_{x_2} \pm i\hat{\mathbf{m}}_{y_2}) e^{\pm i\Phi}, \tag{5a}$$

where upper + and lower - superscripts (subscripts) correspond to the right-handed, and left-handed circular-polarized radiofrequency radiations, respectively. Applying unitary transformation (3) to (5a) we can rewrite the right-handed circular-polarized transition operator in the system, x, y, z , of individual center in the form of:

$$V_{\text{cir}} = \left\{ \frac{1}{\sqrt{2}} g_{\parallel} \sin J \hat{s}_0 + \frac{1}{2} g_{\perp} \left[(\cos J - 1) e^{-ij} \hat{s}_+ + (\cos J + 1) e^{ij} \hat{s}_- \right] \right\} e^{i\Phi} \tag{5b}$$

Transition operator (4) for a linear polarization can be also expressed as a superposition of clockwise- and counterclockwise circular polarizations:

$$\hat{V}_{\text{lin}} = \frac{1}{\sqrt{2}} (\hat{V}_{\text{cir}}^+ + \hat{V}_{\text{cir}}^-)$$

3. Calculation of line shapes of polycrystalline samples

We consider first the polarization effects in ESR of an isolated Kramers doublet with an axial anisotropy of g -factors. Zeeman interaction is described by a standard spin Hamiltonian:

$$\hat{H}_Z = -\hat{\mu}B \equiv - \left[g_{\parallel} \cos J \hat{s}_0 + \frac{1}{\sqrt{2}} g_{\perp} \sin J (e^{ij} \hat{s}_- - e^{-ij} \hat{s}_+) \right] \beta B \tag{6}$$

with the energies ($s = 1/2$): $E_{\pm} = \pm \frac{1}{2} g(\mathbf{J}) bB$, where

$$g(\mathbf{J}) = \sqrt{g_{\parallel}^2 \cos^2 J + g_{\perp}^2 \sin^2 J}$$

Integral ESR contours of powder spectrum are generated by:

$$J_k(B) = \frac{1}{8\pi^2} \int_0^{\pi} \sin J dJ \int_0^{2\pi} dj \int_0^{2\pi} W_k(J, \Phi) r(J, B, \mathbf{e}) dF \quad (7)$$

where $\varepsilon = h\nu$ is radiofrequency quantum; $W_k(J, F)$ is the probability of a transition at a given polarization κ (either linear, or circular), and $r(J, B, \mathbf{e})$ is the form-function of absorption of an individual paramagnetic center. In the case of Kramers doublets the spectrum is generated by the only transition: $W_k(J, F) = \left| \langle E_+ | \hat{V}_k | E_- \rangle \right|$, and in linear polarized radiation the latter takes the form [1–3]:

$$W_{\text{lin}} = \frac{1}{4} g_{\perp}^2 b^2 \left[\frac{g_{\parallel}^2}{g^2(\mathbf{J})} \cos^2 F + \sin^2 F \right] \quad (8)$$

Using the operator (5b) we obtain the transition probability in the case of a circular-polarized radiation as:

$$W_{\text{cir}}^{\pm} = \frac{1}{8} g_{\perp}^2 b^2 \left[\frac{g_{\parallel}}{g(\mathbf{J})} \pm 1 \right]^2 \quad (9)$$

Both probabilities depend on the angles h and M , which define the orientation of polarization vector \mathbf{e} in the plane perpendicular to the external field \mathbf{B} . This dependence vanishes only in a canonical orientation of the external magnetic field, $h = 0$. In this particular case the standard relation $W_{\text{cir}}^{\pm}/W_{\text{lin}} = 2$, applies that is peculiar for relation, 'in the axial symmetry. We would like to stress that this result is not related to a relative amplification of a spectrometer, and is obtained under the assumption of the same amplitude of radiofrequency radiation and, hence, of the same rates of radiofrequency energy that enters the absorption center in both circular and linear polarizations. In arbitrary ($h \neq 0$) field, the ratio, $W_{\text{cir}}^{\pm}/W_{\text{lin}}$ is no longer equal to 2 and is substituted by a more complicated expression that follows from formulas (8) and (9). In addition, more complicated systems (that involve spin-orbital contributions to effective spin levels [13]) bring also the field dependence into expressions of probabilities and their ratios.

We consider next the simplest theoretical model without broadening of individual absorption with form-function, $r(J, B, e) = d[g(J) bB - e]$. Using Eqs. (7) and (9), we arrive at the following contours of ESR lines of polycrystals in the case of circular-polarized radiation (Fig. 2, $g_{\parallel} > g_{\perp}$ is assumed here):

$$J_{\text{cir}}^{\pm}(B) = \frac{g_{\perp}^2 b (e \pm g_{\parallel} bB)^2}{8eB (g_{\parallel}^2 - g_{\perp}^2) (e^2 - g_{\perp}^2 b^2 B^2)} \quad (10)$$

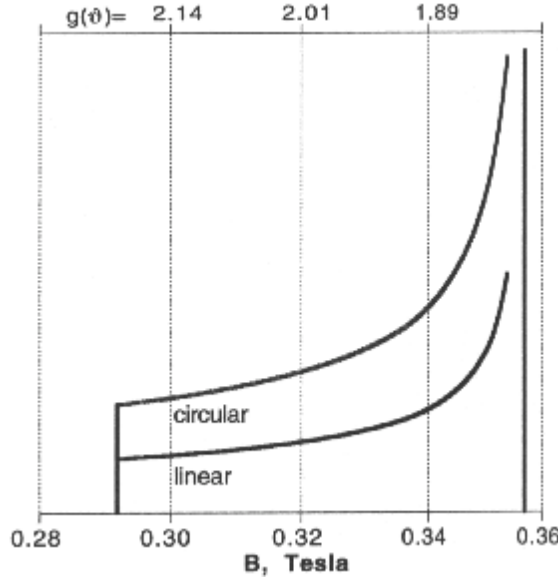


Fig. 2. Line shapes of polycrystalline ESR in the right-handed circular and linear polarizations of quantum, $\varepsilon = 9 \text{ GHz} \cong 0.3 \text{ cm}^{-1}$, for $g_{\parallel} = 2.2$, $g_{\perp} = 1.8$

Same calculations carried out using Eqs. (7) and (8) yield well-known expression for the contours [1–3] referred to absorption of a linear-polarized radiation (Fig.2):

$$J_{\text{lin}}(B) = \frac{g_{\perp}^2 b (e^2 \pm g_{\parallel}^2 b^2 B^2)}{8eB (g_{\parallel}^2 - g_{\perp}^2) (e^2 - g_{\perp}^2 b^2 B^2)} \quad (11)$$

Comparison of these results exhibits a simple ratio of intensities corresponding to the circular and linear polarizations:

$$J_{\text{cir}}^{\pm}(B) = \frac{(e \pm g_{\parallel} bB)^2}{e^2 + (g_{\parallel} bB)^2} \quad (12)$$

Thus, the line shape in a circular polarization is characterized by a similar square root divergence as in the case of a linear-polarized absorption in the field perpendicular to the axial axis. In the field parallel to the axial z -axis, the intensity of the right-handed circular-polarized absorption is twice of that at a linear-polarized radiation in agreement with the above consideration. The ratio of intensities slowly decreases with the increasing field while moving towards the right-hand side of the contour (Fig. 2).

Equation (12) allows one to determine the value of the parallel g -factor, g_{\parallel} . With proper fitting of theoretical and experimentally observed contours in the two polarizations, followed by comparison of one, or several points of the line contours, Eq. (12) provides additional possibility and greater accuracy of parameter's evaluation. Similar approach can be applied to differential contours, as well. The ratio of differential intensities in different polarizations is obtained as:

$$\frac{d(J_{\text{cir}}^{\pm}(B))}{d(J_{\text{lin}}(B))} = \frac{2(g_{\perp}bB)^2(e \pm g_{\parallel}bB) - e[e^2 - (g_{\parallel}bB)^2]}{2(g_{\perp}bB)^2e - e[e^2 - (g_{\parallel}bB)^2]} \quad (13)$$

Let us emphasize that the ratio of intensities of differential contours, $d[J_{\text{cir}}^+(e/g_{\parallel}b)]/d[J_{\text{lin}}(e/g_{\parallel}b)] = 2$, in the field parallel to the z -axis at right-handed circular and linear polarizations remains the same as that for the integral contours.

Formulas (12) and (13) reveal an essential practical advantage of ESR experiments using powder samples subjected to radiation in the two polarizations. Relatively simple expression (13) offers the possibility of experimental determination of both (parallel and perpendicular) g -factors based on the comparison of differential contours obtained in the linear and right-handed circular polarizations of radiofrequency field.

Of course, there are relaxation and other processes which cause the line broadening in real systems. Accounting for broadening of individual absorption γ brings some erosion of the edges of powder ESR line contours and makes it difficult to determine accurately the g -factors on the borders of the spectrum. Nevertheless, at relatively small γ (compared to orientation broadening of the spectrum), the line contours undergo only small changes in the region distant from the borders.

Consequently, Eqs. (12) and (13) represent an appropriate approximation for the central parts of real spectra.

Consider more realistic model that phenomenologically accounts for the line broadening of individual centers. We assume here the Lorentz form-function [1, 3] (with the broadening parameter γ):

$$r(J, B, e) = \frac{1}{\pi} \cdot \frac{g}{g^2 + [g(J)bB - e]^2} \quad (14)$$

Applying again Eqs. (7)–(9) we obtain the following expressions for the line contours in circular and linear polarizations (assuming $g_{\parallel} > g_{\perp}$):

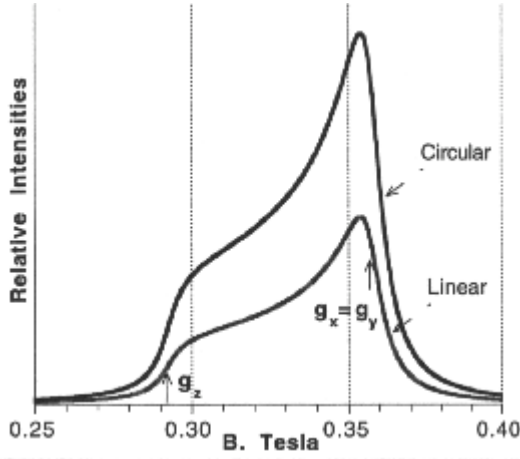


Fig. 3. Integral contours of ESR spectrum generated using Eq.(15) at $g = 50 \text{ Gs} \equiv 0.05 \text{ T}$ in right-handed circular and linear polarizations of radiofrequency quantum, $e = 9 \text{ GHz} \equiv 0.3 \text{ cm}^{-1}$, at $g_{\parallel} = 2.2$, $g_{\perp} = 1.8$

$$\begin{aligned}
 J_{\text{cir}(\text{lin})}(B) &= \frac{g(g_{\perp} b)^2 q(g_{\parallel} - g_{\perp})}{4pH_{\perp}(a_{+} + a_{-})(e^2 + g^2)\sqrt{h^2 - 1}} \\
 &\times \left\{ \frac{(e^2 + g^2 - H_{\parallel}^2) \cdot a_{-} + (e^2 + g^2)^2 - f_{\text{cir}(\text{lin})}(B)}{\sqrt{2a_{-} + 4e^2}} \right. \\
 &\times \ln \frac{\sqrt{(a_{-} + 2eH_{\parallel}) - H_{\perp}} \sqrt{(2a_{-} + 4e^2)(h^2 - 1)}}{\sqrt{(a_{-} + 2eH_{\parallel}) + H_{\perp}} \sqrt{(2a_{-} + 4e^2)(h^2 - 1)}} \\
 &+ \frac{(e^2 + g^2 - H_{\parallel}^2) \cdot a_{+} - (e^2 + g^2)^2 + f_{\text{cir}(\text{lin})}(B)}{\sqrt{2a_{+} + 4e^2}} \\
 &\left. \times \left[\frac{p}{2} - \arctan \left(\frac{a_{+} - 2eH_{\parallel}}{H_{\perp} \sqrt{(2a_{+} - 4e^2)(h^2 - 1)}} \right) \right] \right\} \quad (15)
 \end{aligned}$$

where

$$h \equiv \frac{g_{\parallel}}{g_{\perp}} > 1, \quad H_{\parallel} \equiv g_{\parallel} bB, \quad H_{\perp} = g_{\perp} bB$$

and

$$\left\{ \begin{array}{l} a_{\pm} = \sqrt{(e^2 + g^2 + H_{\perp}^2)^2 - (2eH_{\perp})^2} \pm (e^2 + g^2 + H_{\perp}^2) \\ f_{\text{cir}}^{\pm}(B) = (e^2 + g^2 \pm 2eH_{\parallel})^2 \\ f_{\text{lin}}(B) = (e^2 + g^2)^2 + (2eH_{\parallel})^2 \end{array} \right. \quad (16)$$

ESR line contours in the two polarizations calculated using Eq. (15) are shown in Fig. 3. Analytical formulas (15) and (16) can be employed to determine the g -factor values and Lorentz broadening parameter y , based on the comparison of the line contours obtained in different polarizations. Differences of contours in linear and circular polarizations provide the additional possibility for correlation of theory and experiment.

Acknowledgment

Author appreciates the discussion of the subject with Yu. Rosenfeld and is extremely grateful to B.S. Tsukerblat for the review and valuable comments.

References

- [1] ABRAGAM A., BLEANEY B., *Electron Paramagnetic Resonance of Transition Ions*, Vol. 1, 1970, Oxford, Clarendon Press.
- [2] PAKE G.E., *Paramagnetic Resonance*, 1962, W.A. Benjamin Inc., New York.
- [3] SLICHTER C.P., *Principles of Magnetic Resonance*, 2nd Ed., 1980, Springer-Verlag.
- [4] TAYLOR P.C., BAUGHER J.F., KRIZ H.M., *Chem. Rev.*, 1975, 75 (2), 203–240.
- [5] JIDOMIROV L.M., LEBEDEV Ya.C., DOBRYAKOV S.N., STEINSHNEIDER N.Ya., CHIRKOV A.K., GUBANOV V.A., *Interpretation of Complex EPR Spectra* (in Russian), 1975, Moscow, Nauka.
- [6] TSUKERBLAT B.S., BELINSKII M.I., FAINZILBERG V.E., *Sov. Sci. Rev.*, 1990, 9, 339.
- [7] TSUKERBLAT B.S., BELINSKII M.I., *Magnetochemistry and Radiospectroscopy of Exchange Clusters* (in Russian), 1983, Kishinev, Shtiintza, p. 300.
- [8] TSUKERBLAT B.S., *Group Theory in Chemistry and Spectroscopy*. 1994, Academic Press, p. 430.
- [9] MCCLUNG R.E.D., *Canadian J. Phys.*, 1968, 46, 2271.
- [10] RUDONICZ C., *J. Mag. Res.*, 1985, 63, 95.
- [11] VARSHALOVICH D.A., MOSKALEV A.N., HERSONSKII V.K., *Quantum Theory of Angular Momentum* (in Russian), 1975, Nauka, p. 433.
- [12] BIEDENHARN L.C., LOUCK J.D., *Angular Momentum in Quantum Physics*, Vol. 1, 1981, Addison-Wesley.
- [13] GATTESCHI D., TSUKERBLAT B.S., FAINZILBERG V.E., *Appl. Magn. Res.*, 1996, 10, 217–249.
- [14] FAINZILBERG V.E., BELINSKII M.I., TSUKERBLAT B.S., *Mol. Phys.*, 1981, 44, 1195–1213.
- [15] LANDAU L.D., LIFSHITZ E.M., *Field Theory* (in Russian), 1973, Mir, p. 502.
- [16] LOUDON R., *The Quantum Theory of Light*, 1973, Oxford, Clarendon Press.